Computer-aided-diagnosis of liver fibrosis using non-linear optics microscopy

Xu, Shuoyu

2014

Xu, S. (2014). Computer-aided-diagnosis of liver fibrosis using non-linear optics microscopy. Doctoral thesis, Nanyang Technological University, Singapore.

https://hdl.handle.net/10356/62531

https://doi.org/10.32657/10356/62531

COMPUTER-AIDED-DIAGNOSIS OF LIVER FIBROSIS USING NON-LINEAR OPTICS MICROSCOPY

XU SHUOYU

(B.Sc., PEKING UNIVERSITY)

A THESIS SUBMITTED

FOR THE DEGREE OF DOCTOR OF PHILOSOPY

IN COMPUTATION AND SYSTEMS BIOLOGY (CSB)

SINGAPORE-MIT ALLIANCE

NANYANG TECHNOLOGICAL UNIVERSITY

2014

Acknowledgements

List of Publications

Xu, S., Wang, Y., Tai. D.C.S., Wang, S., Cheng, C.L., Peng, Q., Yan, J., Chen, Y., Sun, J., Liang, X., Zhu, Y., Rajapakse, J.C., Welsch, R., So, P.T.C., Wee, A., Hou, J., and Yu, H. *qFibrosis: A fully-quantitative innovative method incorporating histological features to facilitate accurate fibrosis scoring in animal model and chronic hepatitis B patients*, Journal of Hepatology 2014 Aug; 61(2):260-9.

Xu, S., Kang, C., Gou, X., Peng, Q., Yan, J., Kang, Y., Cheng, C., Xia, W., He, Y., Welsch, R., So, P.T.C., Rajapakse, J.C., Yu, H. *Quantification of liver fibrosis via surface imaging of the Glisson's capsule*, Scientific Reports, submitted.

Stanciu, S.G., **Xu, S.**, Peng, Q., Yan, J., Stanciu, G.A., Welsch, R.E., So, P.T.C., Yu, H. *Experimenting Liver Fibrosis Diagnostic from Liver Surface by Two Photon Excitation Microscopy and Bag-of-Features Image Classification*, Scientific Reports 2014 Apr 10;4:4636.

Venkatesh, S.K., **Xu, S.**, Tai, D., Yu, H., and Wee, A. (07/2013) *Correlation of Magnetic Resonance Elastogrpahy with Morphometric Evaluation of Hepatic Fibrosis and Histologic Staging in Chronic Hepatitis B*, Magnetic Resonance in Medicine 2014 Oct 72(4):1123-1129.

Raja, A.M., **Xu, S.**, Tai, D.C.S., Sun, W., So, P.T.C., Welsch, R.E., Chen, C.-S., Yu, H., *Differential Remodeling of Extra-Cellular Matrices by Breast Cancer Initiating Cells*, Journal of Biophotonics, *in press*.

Yan, J., Kang, Y., **Xu, S.**, Ong, S.L.L., Zhuo, S., Bunte, R.M., Chen, N., Asada, H.H., So, P., Wanless, I.R., and Yu, H., In vivo label-free quantification of liver microcirculation using dual modality microscopy, Journal of Biomedical Optics, 11 November 2014; 19(11): 116006.

Zhuo, S., Yan, J., Kang, Y., **Xu, S.**, Peng, Q., So, P.T.C., and Yu, H., In vivo, label-free, three-dimensional quantitative imaging of liver surface using multi-photon microscopy, Applied Physics Letters, 16 July 2014; 105(2): 023701.

Yin, L., Zheng, D., Limmon, G.V., Leung, N.H.N., **Xu, S.**, Rajapakse, J.C., Yu, H., Chow V.T.K., and Chen, J., Aging Exacerbates Damage and Delays Repair of Alveolar Epithelia following Influenza Viral Pneumonia, Respiratory Research, 30 September 2014; 15(1):116.

Yin, L., **Xu, S.**, Cheng, J., Zheng, D., Limmon, G., Leung, N., Rajapakse, J., Chow, V., Chen, J., Yu, H., *Spatiotemporal quantification of cell dynamics in the lung following influenza virus infection*, Journal of Biomedical Optics; 18(4):46001, 04/2013.

Lin, J., Lu, F., Zheng, W., **Xu, S.**, Tai, D., Yu, H., Huang, Z., *Assessment of liver steatosis and fibrosis in rats using integrated coherent anti-Stokes Raman scattering and multiphoton imaging technique*, Journal of Biomedical Optics; 16(11): 116024, 2011.

He, Y., Kang, C., **Xu, S.**, Tuo, X., Trasti, S., Raja, A., Peng, Q., So, P., Rajapakse, J., Welsch, R., Yu, H., *Toward surface quantification of liver fibrosis progression*, Journal of Biomedical Optics; 15(5):056007, 2010.

Raja, A., **Xu, S.**, Sun, W., Zhou, J., Tai, D., Chen, C., Rajapakse, J., So, P., Yu, H., *Pulse-modulated second harmonic imaging microscope quantitatively demonstrates marked*

increase of collagen in tumor after chemotherapy, Journal of Biomedical Optics; 15(5): 056016, 2010.

Tai, D., Tan, N., **Xu, S.**, Kang, C., Chia, S., Cheng, C., Wee, A., Wei, C., Raja, A., Xiao, G., Chang, S., Rajapakse, J., So, P., Tang, H., Chen, C., Yu, H., *Fibro-C-Index: comprehensive, morphology-based quantification of liver fibrosis using second harmonic generation and two-photon microscopy*, Journal of Biomedical Optics, 14(4): 044013, 2009.

Table of Contents

Abstract

Excessive accumulation of extracellular matrix results in fibrosis, which is the hallmark of chronic liver diseases. The role of liver biopsy as the gold standard for liver fibrosis assessment has recently been challenged due to inter- and intra-observer variation and sampling error. We have developed *q*Fibrosis - a fully-automated classification of liver fibrosis through quantitative extraction of pathology-relevant features using non-linear optics microscopy, trained and tested in both animal and human studies. *q*Fibrosis faithfully recapitulates the liver fibrosis staging performed by pathologists, and is robust with reference to sampling size. It can significantly predict staging underestimation in short biopsy cores, thus aiding in the correction of sampling error-mediated intra-observer variation. *q*Fibrosis can predict the staging underestimation of the non-expert pathologist, thus further aiding in the correction of inter-observer variation. *q*Fibrosis can also significantly differentiate intra-stage cirrhosis changes that can be monitored for making informed clinical decisions, and for predicting possible prognostic outcomes. *q*Fibrosis has the potential to expedite the re-establishment of liver biopsy as the gold standard for assessment of fibrosis in chronic liver diseases. Furthermore, we have hypothesized that the less invasive liver surface imaging could serve as a favourable alternative to biopsy. We established a Capsule Index based on significant parameters extracted from the non-linear optics microscopy images of liver capsule from two fibrosis rat models. The Capsule Index is capable of differentiating different fibrosis stages in both animal models, making it possible to quantitatively stage liver fibrosis via liver surface imaging without biopsy.

Summary

Excessive accumulation of extracellular matrix results in fibrosis which is the hallmark of chronic liver disease, such as chronic hepatitis B and C virus infection, alcoholic liver disease, non-alcoholic steatohepatitis and autoimmune liver disease. Liver biopsy has been the gold standard for fibrosis assessment for more than a century, providing information on inflammatory activity and collagen architecture that are not obtainable with non-invasive techniques. The conventional histological staging of liver fibrosis is semi-quantitative, relying on a global assessment of architectural distortion and associated fibrosis, in biopsy samples. It is, however, highly subjective to sampling error and inter-observer variation; both of which have led to the liver biopsy being challenged as the gold standard for fibrosis assessment in recent years.

With the advancement of new imaging modalities and image informatics techniques, the major contribution of this thesis is to introduce the newest development of image analytic tools to characterize liver fibrosis progression quantitatively from liver biopsy samples using non-linear optics microscopy thus to improve the liver diseases diagnosis and re-establish biopsy based assessment as the gold standard. This thesis also presents the first study to quantitatively monitor fibrosis progression from the collagen capsule of liver surface that sheds a light on the potential application of liver surface scanning using an endoscope as a totally new method for liver disease diagnosis that is less invasive than biopsy.

The non-linear optical microscopy especially second harmonic generation microscopy makes it possible to image collagen directly from unstained samples without staining variations. In chapter 2, we investigated the application of second harmonic generation imaging on unstained liver tissue samples for quantitative liver fibrosis assessment. We proposed a quantification system, Fibro-C-Index, by quantifying the collagen amount in the samples. We have validated the system in both animal and human study and compared the index with other non-invasive liver fibrosis measurements.

As it has been shown that the histo-pathological features of collagen architecture and patterns used in semi-quantitative scoring systems by pathologists are more important than collagen amount to assess liver fibrosis, we presented qFibrosis, the improved liver fibrosis quantification system by incorporating histo-pathological features in Chapter 3. qFibrosis was validated in a Thioacetamide-induced rat model and in chronic hepatitis B biopsy samples. The results indicated that qFibrosis can reliably recover liver fibrosis staging, with reduced variability of sampling error and inter-/intraobserver bias. qFibrosis may become a powerful novel tool for precise analysis of fibrosis in basic research; and a surrogate histological marker for evaluating liver fibrosis and for monitoring anti-fibrotic drug efficacies in clinical practice.

On the other hand, the highly invasive nature of liver biopsy for assessing fibrosis led us to hypothesize that the less invasive liver surface imaging could serve as a favourable alternative. In Chapter 4, we investigated whether non-linear optical imaging of the Glisson's capsule at liver surface would yield sufficient information to allow quantitative staging of liver fibrosis. In contrast to conventional tissue sections whereby tissues are cut perpendicular to the liver surface and interior information from the liver biopsy samples were used, we have established a Capsule Index based

on significant parameters extracted from the second harmonic generation microscopy images of capsule collagen from anterior surface of rat livers. The Capsule Index is capable of differentiating different fibrosis stages in two animal models used, making it possible to quantitatively stage liver fibrosis via liver surface imaging without biopsy.

List of Tables

List of Figures

List of Abbreviations

2D	Two-dimensional
3D	Three-dimensional
ANOVA	Analysis of variance
AUC	Area under ROC
BDL	Bile duct ligated
BOF	Bag-of-feature
CARS	Coherent anti-Stokes Raman scattering
CHB	Chronic hepatitis B
CHC	Chronic hepatitis C
CI	Confidence interval
CLD	Chronic liver disease
CPA	Collagen percentage area
CV	Coefficient of variation
ECM	Extracellular matrix
FMM	Fast matching method
GLCM	Gray-level co-occurrence matrix
GLOH	Gradient location and orientation histogram features
H&E	Hematoxylin and eosin
HAI	Histological activity index
HVPG	Hepatic venous pressure gradient
INR	International normalized ratio
MIP	Maximum intensity projection
MNL	Multinomial logistic regression
MRE	Magnetic resonance elastography
MRI	Magnetic resonance imaging

MT	Masson trichrome
NAFLD	Non-alcoholic fatty liver disease
NAS	NAFLD activity score
NASH	Non-alcoholic steatohepatitis
PC	Principal component
PCA	Principal component analysis
ROC	Receiver-operating-characteristics curve
ROI	Region of interest
SD	Standard deviation
SHG	Second harmonic generation
SIFT	Scale-invariant feature transform
SNR	Signal-to-noise ratio
SRS	Stimulated Raman scattering
SURF	Speeded up robust features
SVM-RFE	Support vector machine recursive feature elimination
TACS	Tumor-associated collagen signatures
TE	Transient elastography
THG	Third harmonic generation
TPEF	Two-photon excitation fluorescence

Chapter 1

Introduction

Liver fibrosis is associated with the excessive deposition of extracellular matrix (ECM) proteins, such as collagen, as a recurrent wound healing response to most chronic liver diseases [1]. The injury of the hepatocytes due to viral infection, heavy alcohol consumption, toxins or other factors will activate the immune system and start the repair process. The inflammatory immune cells are stimulated to release cytokines, growth factors and other chemicals which support hepatic stellate cells to activate and produce collagen, fibronectin, and other substances [2]. These substances are deposited in the liver and cause the build-up of ECM. Although the ECM production and degradation are in balance in a healthy liver, the process of degrading collagen is impaired in an injured liver which leads to excessive accumulation of ECM and fibrosis. The accumulation of ECM distorts the hepatic architecture by forming a fibrous scar, and the subsequent development of nodules of regenerating hepatocytes defines cirrhosis, the advanced stage of fibrosis. Cirrhosis produces hepatocellular dysfunction and increased intrahepatic resistance to blood flow, which result in hepatic insufficiency and portal hypertension, respectively [3].

Assessment of liver fibrosis severity is commonly used for staging chronic liver diseases, and for therapeutic efficacy evaluation. Various invasive and non-invasive techniques are used or under study to detect liver fibrosis [4, 5]. The most widely

adopted non-invasive methodologies include serum markers from blood tests and liver stiffness measurement by elastography imaging of the liver [6].

A large number of serum markers have been developed for the assessment of liver fibrosis directly or indirectly. The direct markers directly represent the level of the components of ECM while indirect markers may need to be combined together with direct makers to form certain indices. FibroTest [7], which combines six serum markers (Alpha-2-macroglobulin, Haptoglobin, Apolipoprotein A1, Gamma-glutamyl transpeptidase, Total bilirubin, and Alanine transaminase) together with age and gender of the patients, is the most popular biomarker test in the market and has been tested in clinical trials. The other available indices include PAPAS index [8], FIB-4 [9], APRI [10], and APGA [11] etc, which use different formulas or regression models to combine serum markers. Most of these indices are shown to be useful for detecting advanced fibrosis; however, the sensitivities are rather poor to identify early and mild fibrosis which limits the prospect of such techniques. Moreover, as these biomarkers in the blood could be affected by the fibrogenesis and metabolism changes in other organs, such techniques may only be applied when certain ideal requirements are met [12].

Liver stiffness measurement is becoming an alternative to the serum markers for non-invasive diagnosis of liver diseases. Such techniques include transient elastography (TE) [13] and magnetic resonance elastography (MRE) [14, 15]. The reproducibility of both of the techniques is excellent and recent studies suggest that both of the techniques are good for diagnosis of significant fibrosis with sensitivity and specificity values over 90% [16]. However, the diagnostic performances decrease dramatically for mild fibrosis. Besides, the TE has the limitation that the results will be greatly affected in obese patients as the depth of the signal penetration is limited

[17]. Meanwhile, MRE does not have such limitation for obese patients, but its results are highly dependent on operator expertise [18]. Moreover, since some pathophysiological processes other than fibrosis may also contribute to liver stiffness change, the liver stiffness measurement may not be able to reflect fibrosis progression in particular [14, 19].

In all, most of the currently adopted non-invasive methodologies are effective in qualitatively assessing the presence or absence of the disease, rather than assessing precisely the progression of fibrosis in a step-wise fashion. This limits the clinical usefulness of the tests, as it is important to track the progression of disease to predict the eventual timing of liver function loss and the onset of portal hypertension or other complications which determine proper courses of therapeutic intervention.

Liver biopsy remains the gold standard in tracking fibrosis progression despite the fact that it is an invasive procedure and the risks of sampling error, provided that the specimens are of at least 25 mm in length, including at least 11 portal tracts [20-22]. After biopsy, tissue samples are stained and passed to experienced pathologists to yield either a descriptive or semi-quantitative score. These scoring systems, originally designed for specific liver diseases like hepatitis C, focus on qualitative rather than quantitative properties of fibrosis development, grouping liver fibrosis into categories of severity. The first semi-quantitative scoring system came out in 1980s, which allocated a range of numbers presenting different categories to pathological features on the basis of their severity [23]. Several routinely used scoring systems include Knodell histological activity index (HAI) [24], Scheuer [25], Ishak [26] and Metavir [27] systems. The detailed pathological features of two most widely used staging systems are shown in **Table 1** where numerical numbers are assigned accordingly.

Although liver biopsy still remains the only reliable method for liver fibrosis assessments until now, it has been questioned whether it should remain the golden standard due to several drawbacks. In the following part of this chapter, we first describe the limitations of the current gold standard technique – liver biopsy, which motivated us to conduct this thesis research aiming to overcome these drawbacks to a certain extent with the help of the state-of-art imaging and computation techniques. Our contributions for developing imaging modalities and image analysis techniques are summarized in the second section, followed by the reviews of the previous works that focus on the foundations for this study in the next section. We finally conclude the chapter with the outline of thesis.

Table 1: Histo-pathological features used in different liver fibrosis scoring systems

Stage	Metavir	Ishak
0	No fibrosis	No fibrosis
1	Fibrous portal expansion	Fibrous expansion of some portal areas, with or without short fibrous septa
2	Few bridges or septa	Fibrous expansion of most portal areas, with or without short fibrous septa
3	Numerous bridges or septa	Fibrous expansion of most portal areas with occasional portal to portal bridging
4	Cirrhosis	Fibrous expansion of most portal areas with marked bridging (portal to portal as well as portal to central)
5		Marked bridging (portal-portal and/or portal-central) with occasional nodules (incomplete cirrhosis)
6		Cirrhosis, probable or definite

1.1 Motivation and objectives

Although there have been various approaches for observing and assessing liver fibrosis currently, liver biopsy is the particular one which acquires the diseased tissue specimen and directly observes the histological changes in the tissue, thus remaining the gold standard for providing the pathology progress information that is substantially supportive for important clinical strategy development. However, liver

biopsy currently taken in clinical settings has its own limitations, which compromises to some extent its diagnostic power. These limitations are summarized as follows.

Invasive Procedure

As an invasive procedure, liver biopsy comes with significant pain and major complications occurring in 30% and 0.5% of patients, respectively. 1-2% of the biopsied patients may suffer significant bleeding and 2-3% of the biopsied patients require hospitalization. Fatal complications may occur in up to 0.01-0.3% of biopsied patients [28].

Staining Variations

Special histochemical staining of the biopsy samples is required routinely for the assessment of liver fibrosis. The most common used staining is hemotoxylin and eosin (H&E) stain which colors nuclei of cells blue and other eosinophilic structures in various shades of red, pink and orange. However, when it comes to the specific staining, the panel varies from laboratory to laboratory. For the purpose of liver fibrosis assessment, collagen need to be specifically stained in tissue samples, where several different staining methods are applied such as Masson trichrome (MT) stain, Sirius Red stain, reticulin stain and Van Gieson stain. The colours of the stained samples are different from different stainings which makes it difficult to standardize the samples and follow evaluation procedures between the labs. Moreover, there are colour variations of the staining between different labs or operators even with the same staining protocol (**Figure 1**). Besides, all these stainings are time-consuming procedures which generally require several steps and more than 45 minutes, and will increase the patients' costs additionally.
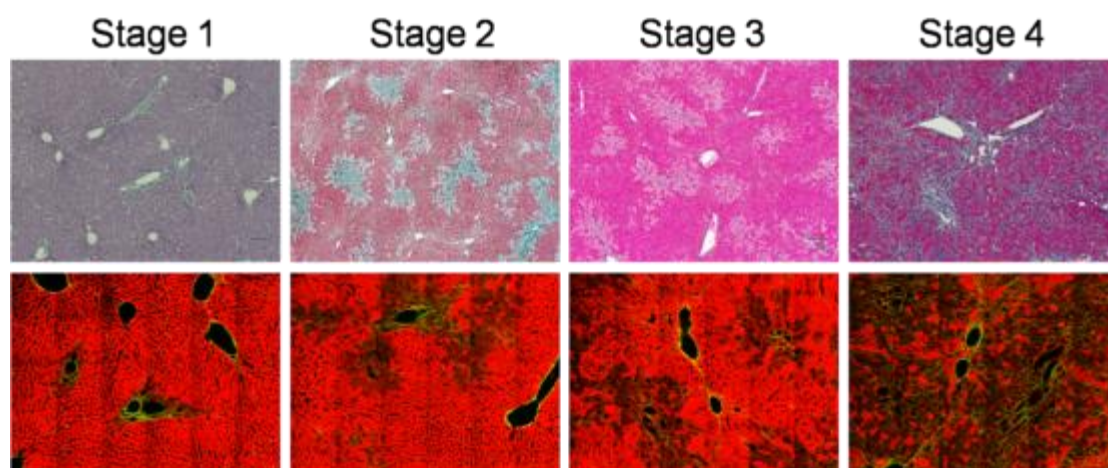
Figure 1: Staining variation of liver tissue samples from different stages using the same Masson Trichrome staining method.

Sampling Error

As needle liver biopsy generally only represents 1/50000 of the total liver organ and fibrosis distributes heterogeneously, sampling error can occur due to its localized sampling site and limited sampling size, which may lead to inaccurate grading and staging of liver fibrosis [29, 30]. Although it is suggested that the sampling variation can be reduced by taking several biopsies from the same patient [21], the approach is not well adopted due to the increased risk of morbidity and mortality after taking more biopsies. Other studies have suggested that an adequate biopsy should be at least 25 mm in length while including at least 11 portal tracts [22]. However, although using adequate biopsies which meet these criteria can help to reduce the sampling error, the sampling variation can still be as high as 40% according to Bedossa *et al* [20].

Evaluation Bias

Liver biopsy is also limited by the evaluation bias origins from assessment-system due to its semi-quantitative property and inter- and intra- observer variability [31]. These semi-quantitative scoring systems aim to group liver fibrosis into categories of severity based on a limited number of well-characterized morphologic patterns, which very much relies on the observers' subjective opinion. Therefore, the inter- and intra-observer variations can be as high as 35% and it is difficult to obtain highly reproducible results from these systems [32-34]. Moreover, severities of the samples which are assigned in the same category cannot be further assessed to reflect fine fibrosis progression or regression, which may be important for drug efficiency evaluation and prediction of disease progression.

It is a big challenge to overcome these limitations of the liver biopsy, and great efforts have been made in the field which motivates us to keep exploring in this direction. The objectives of this thesis research are to develop new computation tools together with new imaging modalities to improve the diagnosis of liver fibrosis which are introduced as follows:

Objective 1: Feasibility study of quantitative liver fibrosis assessment using non-linear optics microscopy.

To overcome the evaluation bias problem of the liver fibrosis assessment, several studies have reported to quantify liver fibrosis through image analysis techniques. These computer-aided systems aim to provide objective quantitative measurements which are able to exclude observer discrepancies. However, all of these systems work for stained biopsy samples, and have the difficulty dealing with staining variations.

Driven by the telecommunication boost in recent years, developments in both mode-locked lasers and highly sensitive optical sensors have made nonlinear optical

microscopy— such as the two-photon excited fluorescence (TPEF) and second harmonic generation (SHG) [35] — an affordable option for tissue imaging. In particular, SHG is capable of imaging collagen from unstained tissue samples since it is a nonlinear optical process requiring no fluorophore presence. Our aim is to develop a quantification method to measure collagen proportionate area (CPA) for TPEF/SHG images on unstained liver tissue samples to demonstrate its capability for quantitative liver fibrosis assessment, which could be a good substitution for stained samples. The imaging can be applied on unstained sample directly with no staining variation problem anymore.

Objective 2: Development of innovative image analytic tool incorporating pathological relevant features for liver fibrosis assessment

Collagen percentage area (CPA) was widely adopted as the measurement to quantitatively grade and stage fibrosis. Although some correlations were found between CPA and results of semi-quantitative scoring, CPA is not specifically addressed in any of the scoring systems. Other pathological features such as fibrosis architecture change play a more important role in grading and staging fibrosis, which leads to the need of computer-aided systems with more measurements than CPA only. Therefore, we aim to propose new image analysis techniques that not only quantify CPA but also characterize morphology and architecture changes of collagen patterns. The new technique should be capable of providing indices which has better correlation with pathology scores than CPA and inheriting its advantages of diminishing evaluation bias.

Objective 3: Feasibility study of liver fibrosis assessment using non-linear endoscopy from liver surface.

The limitations of being invasive and sampling error cannot be avoided if liver biopsy approach is adopted. Current available non-invasive methodologies still are not able to replace liver biopsy because of their own limitations in precisely assessing the progression and regression of fibrosis. Recent studies have reported the feasibility of liver surface scanning based on non-linear SHG fiber-optic endoscope, which can potentially be used clinically to complement or eventually replace the more invasive liver biopsy. In view of translating this imaging technique from bench to bed side, we aim to develop automated image analysis methods to quantify liver fibrosis progression at the liver surface and provide a histological index for further clinical applications. By incorporating our histological index with SHG endoscopes, we see the feasibility of liver fibrosis diagnosis from the liver surface, which would therefore give us the potential to image larger sampling area than from biopsy and extract enough information over a long period of time without the complication brought forth by the invasive biopsy.

1.2 Contributions of this thesis

With the advancement of new imaging modalities and image informatics techniques, it is promising to overcome or at least improve some of the weaknesses of the biopsy based liver fibrosis assessment so as to re-establish it as the gold standard. The non-linear optical microscopy makes it possible to image collagen directly from unstained samples without staining variations. The automated image analysis techniques is capable of reducing inter- and intra- observer discrepancies significantly by evaluating fibrosis in a quantitative manner. It is also feasible to achieve virtual liver biopsy by scanning the liver surface with the non-linear endoscope which does not have the limitations on sample sites and areas and tends to be a less invasive procedure than liver biopsy. In light of the above, this thesis aims to contribute a step

further in these aspects, focusing on the development of new image analytic tools to characterize liver fibrosis both from liver interior and liver surface using non-linear optics microscopy thus to facilitate the improvement of liver diseases diagnosis which could potentially benefit the patients. The research in this thesis has made three main specific contributions:

(1) <u>An improved quantification method to measure collagen proportionate area in TPEF/SHG images for liver fibrosis assessment</u>

Collagen proportionate area is widely accepted as the important quantitative feature to characterize liver fibrosis progression. However, all existing methods are developed for stained images using colour information. We present Fibro-C-Index, a new quantification system to measure collagen proportionate area in TPEF/SHG image using both cellular information from TPEF image and collagen information from SHG image. The method was first validated in the bile duct ligation (BDL) animal model comparing with the conventional histopathology scores, and then tested in a human study for hepatitis B patients comparing with liver stiffness measurement as well as histopathology scores.

(2) <u>First quantitative method incorporating histo-pathological features for liver fibrosis assessment</u>

Collagen proportionate area is sensitive to sampling error and its ability to differentiate between fibrosis stages is limited. The histo-pathological features of collagen architecture and patterns used in semi-quantitative scoring systems by pathologists are more important to assess fibrosis. In order to recognize these patterns by automated image analysis algorithms and include this path-architecture information for quantification, we develop an algorithm to classify collagen into portal collagen, septa collagen and fibrillar collagen according to the pathological

knowledge. Morphological and spatial features are further extracted for each collagen group and a statistical framework is proposed to reduce the dimension of the features into a single index - *q*Fibrosis. The algorithms are developed and validated on a thioacetamide (TAA) inducded animal model which has similar collagen architecture patterns as hepatitis B. We have further tested the proposed index on two independent cohorts of human biopsy samples of hepatitis B which reveal the promising results of characterizing liver fibrosis progression.

(3) <u>First quantitative method for liver fibrosis assessment from liver surface</u>

Liver capsule is not assessed during diagnosis in conventional ways. However, with the development of modern imaging techniques, we are able to image liver capsule which can provide a new way to grade and stage liver fibrosis. An algorithm based on minimum spanning tree was developed which is capable of extracting complete but compact major axis of collagen fibers in the capsule SHG images which has high level of noise. Geometry measurements are quantified after individual collagen fibers are identified. Besides, we also extracted hundreds of texture features from capsule images. We selected the most useful features from all the measurements and combine the selected measurements into one index – Capsule Index. The new index successfully differentiates between non-fibrosis and fibrosis samples, as well as between early fibrosis and late fibrosis samples, which shows the potential of applying surface scanning as a totally new method to monitor liver disease progression.

1.3 Review of previous works

In this section, we will first introduce the application of SHG/TPEF microscopy in disease diagnostics as a new powerful optical imaging modality. Image informatics techniques for characterizing fibrosis and cellular morphologies in SHG/TPEF images

11

will also be discussed. We will next focus on reviewing all the existing image analysis approaches to quantify liver fibrosis progression from histological liver biopsy images in clinical studies. Finally, we will discuss the role of the liver capsule from liver surface for fibrosis diagnosis and review the existing computation techniques to characterize collagen network geometry.

1.3.1 Short overview of SHG/TPEF microscopy

Fluorescence imaging is widely adopted in pathology applications to study the localization and distribution of molecular in cellular and tissue structures. The development of advanced imaging tools as well as new fluorescence proteins and fluorescent dyes enables pathologists a series of more powerful tools to assess cells and tissue that are not visible previously. One major limitation of the conventional widefield one-photon fluorescence is the affected image contrast and resolution due to the blurring caused by the emission light outside of the imaging focal plane. The use of pinhole in confocal laser scanning fluorescence microscopy improves the image contrast by eliminating the out-of-focus light. However, it blocks the laser light emitted at the focal point at the same time which reduces the detection sensitivity and imaging depth.

With the developments in both mode-locked lasers and highly-sensitive optical sensors, non-linear optical microscopy such as multi-photon excited fluorescence and multi-harmonic generation become an affordable option for tissue imaging [35, 36]. When the power of excitation light is low, the macroscopic polarization of the media is proportionate to the electric field strength known as the linear optics affect. In the case of laser excitation when the power is much higher, this response becomes non-linear and the media properties are not only related to the electric field strength but a power series expansion of it. For instance, the second harmonic generation effect

comes from the quadratic terms of the power series expansion and the cubic terms gives rise to the two-photon absorption. In recent studies, two-photon excited fluorescence (TPEF) microscopy has been widely used for imaging structure and dynamic interactions in biological tissues while second harmonic generation (SHG) microscopy has been increasingly used for measuring highly ordered structures without central symmetry in tissue [37-39].

The two photon excitation of molecules is a nonlinear process that involves the absorption of two photons whose combined energy is sufficient to induce a molecular transition to an excited electronic state. Even though this idea dates back to 1931 when the Nobel laureate Maria Goppert Mayer predicted in her doctoral thesis the phenomenon of two photon absorption, it was not until 1990 when Denk et al exploited this phenomenon in regard to fluorescence microscopy. In more detail, two-photon excitation fluorescence microscopy exploits the fact that a fluorophore can be excited by two photons with lower energy than required in one photon excitation. The two photons have smaller frequencies and longer wavelengths than the one photon that would provide the same results. Excited by these two photons, the fluorophore acts in the same way as if it was excited by only one photon, emitting a single photon whose wavelength is only determined by its intrinsic characterstics, such as fluorophore type, chemical structure, etc. As the chance of absorption of two photons at the same time for excitation is proportional to the square of the laser power, thus such chance is extremely low out of the imaging volume and nothing is excited so that the out-of-focus blurring is minimized. Comparing to the confocal one photon fluorescence imaging, since no pinhole is used, all the emitted light at the imaging volume can be detected which improves the detection sensitivity and imaging depth.

SHG imaging shares the same laser source with the TPEF imaging and can be performed together. Other than TPEF imaging which results from the nonlinear excitation of molecules, SHG imaging depends on the material properties such as orientation, polarization and local symmetry property etc. For example, collagen consists of a triple helix structure which is asymmetry and produces SHG signals. In this process, an excitation signal is converted to an emission signal with double the energy while no absorption of the excitation photon happened.

Compared to the conventional technique of imaging collagen by using transmitted light microscopy of histological tissue sections stained with Masson's trichrome or picrosirius red, SHG is more specific for the collagen type I in ECM which is noncentrosymmetry and capable of generating SHG signals, thus does not need the samples to be stained which excludes the variation in staining resulting from different batches of stains, protocols, time dependant fading and photobleaching [40, 41]. The other advantages of using SHG to image collagen include requiring no fluorophore presence in tissue so that signals are unaffected by dye concentration and photobleaching; excitation source can be at infrared range, resulting in less scattering in tissue; deeper tissue penetration for imaging purposes and three-dimensional visualization of the fiber architecture [42]. TPEF can provide complementary structure and cellular information [43], as TPEF has different excitation mechanism than SHG so that TPEF signals can be easily separated from SHG signals using appropriate detectors. Since ECM is highly altered in many diseases such as cancer, connective tissue diseases, cardiovascular diseases and autoimmune disorders, SHG/TPEF has the potential to play an important role in disease diagnostics with its advantages over traditional histology as described.

1.3.2 Application of SHG/TPEF microscopy and image informatics for disease diagnostics

Due to the handy accessibilities and abundant collagen in skin SHG/TPEF microscopy is found useful in applications of dermatology. Yeh *et al* [44] and Tai *et al* [45] first demonstrated the applicability of SHG to provide distribution of collagen fibers in dermis in rodent and human skin samples, respectively, in a qualitative manner. Lin *et al* [46] presented a quantitative MFSI index which calculates the signal ratio between TPEF and SHG images to differentiate cancer cells and adjacent cancer stroma from the normal dermis successfully. Dong's team [47] further used polarization-resolved SHG microscopy to distinguish normal and dermal pathological conditions of keloid, morphea, and dermal elastolysis according to the finding that the peaks of the histogram of the second order susceptibility tensor element ratio is wider in pathological skins, which suggested more heterogeneous structures of pathological dermal collagen fibers. Cicchi *et al* [48] adopted texture analysis by calculating correlation, homogeneity and energy from gray-level co-occurrence matrix together with collagen/elastin content scoring to characterize skin tissue with particular dermal disorder. An automated image-pattern classification algorithm was developed by Medyukhina *et al* [49] to discriminate between keloid and healthy skin. They calculated two waviness parameters of collagen: the corrected average shift of the center of mass and the inter-fiber variability of the Feret's angle and the combination of two were found to separate normal and keloid skin samples with statistical significance. Wu et al [50] reported the quantification of orientation index and collagen bundle packing by fast Fourier transform as good indicators for the statuses of aging skins. Recent work by Puschmann et al [51] also suggested the elastin-to-collagen ratio as a useful parameter to quantify age-associated alterations in the

extracellular matrix. Another study by Chen *et al* [52] showed the collagen content increased in both upper dermis and the deep dermis with the progression of keloid.

The predominant extracellular collagen in corneal membrane layers suggests promising application of SHG/TPEF microscopy in ophthalmology as well. Yeh *et al* [53] were among the first to report the capability of SHG/TPEF microscopy to reveal three-dimensional structure of the corneal stroma, which contains approximately 88% of collageous fibrils, in a rabbit model. Han *et al* [54] further visualized the morphology of collagen fibrils in cornea and sclera with SHG/TPEF microscopy and concluded the differences of collagen fibril morphology account for the transparency of cornea and high stiffness and elasticity of the sclera. Tan *et al* [55] demonstrated the value of MFSI index in infectious keratitis diagnosis. More recently, a quantitative analysis was performed by Matteini *et al* [56] to study photothermally-induced alterations of corneal stroma by SHG imaging. The collagen orientation and arrangement were assessed to provide a good description of collagen morphology changes along with the progressive thermal modifications.

Using SHG/TPEF microscopy as a tool to study cancer microenvironment provided the insights of how tumor formation and progression were affected by extracellular matrix organization. The pioneer works in this area were reported by Keely's group [57-59] in mammary tumor and breast cancer studies. They presented three tumor-associated collagen signatures (TACS) to characterize tumor microenvironments. The first signature characterizes the presence of locally dense collagen within the globally increased collagen concentration surrounding tumors. The second signature was designed for collagen fibers stretched around the tumor. The third signature identified radially aligned collagen fibers that facilitate local invasion by a distribution of collagen fiber angles around 90 degrees relative to the tumor boundary. The

signatures were able to provide indications to assess whether a tumor is invasive or not. Adur *et al* [60] further reported pathological changes associated with ovarian cancer can also be characterized by TACSs, as well as by collagen density and epithelium width. Other studies on ovarian cancer had been done by Kirkpatrick *et al* [61] and Nadiarnykh *et al* [62]. The former quantified SHG-based texture from gray-level co-occurrence matrix, the spatial frequency characteristics of the SHG images by Fourier transform, and cellular redox ratios from TPEF images. The latter adopted an integrated approach combing 3D SHG imaging and optical parameter measurements to calculate the tissue scattering coefficient and scattering anisotropy, as well as the intensity ratio between forward and backward SHG signal and attenuation-rate of intensity decrease along increasing depth into tissue. Besides, Hompland et al [63] observed differences of collagen density, second-order nonlinear optical susceptibility and anisotropy parameter between osteosarcoma, breast carcinoma and melanoma, and Wang *et al* [64] applied their MFSI index in the lung cancer study. Zhang *et al* [65] also reported the visualization of the invasive cancer cell in their native environment in human melanoma skin tissue from TPEF/SHG co-localization images which provide the insights of cell morphology and cell-ECM organization.

Accumulation of ECM proteins such as collagen serves as an important signature of fibrosis. The applicability of SHG/TPEF microscopy to monitor fibrosis progression in liver was first demonstrated by Cox *et al* [42] as SHG images showed the extensive collagen fibers in cirrhotic liver samples. Our group presented a study [41] on quantification of liver fibrosis in a bile duct ligated (BDL) rat model. We quantified collagen percentage area in SHG images by the automated Otsu segmentation method. The segmented collagen were further grouped into aggregated and distributed using

low pass filters and the progression patterns of two groups of collagens suggested the regression of fine distributed collagen and progression of large aggregated collagen along the fibrosis progression. Sun *et al* [66] reported similar findings as our study using a limited number of human liver samples. Guilbert *et al* [67] reported a new scheme for liver fibrosis scoring under different SHG/TPEF imaging settings. A reference sample was required to set the reference gain and signal intensities. Each SHG image would be normalized according to the reference gain and signal intensities and the normalized images would be segmented using a fixed threshold to calculate collagen percentage area as the fibrosis score. Besides, Pena *et al* [68] first reported 3D spatial distribution of lung fibrosis using SHG/TPEF microscopy, and they measured histograms of background noise and applied to the images a threshold corresponding to the maximum background value to quantify collagen percentage in different areas which successfully sorts out control and fibrotic lung samples. Strupler *et al* [40] presented a quantification method for kidney fibrosis in a mouse model. A threshold was applied to SHG images after noise subtraction and correction to identify collagen percentage area, which appears to be appropriate to differentiate control and fibrotic mice. In their further study [69] on renal interstitial fibrosis, the SHG quantification also achieved good agreement with pathology scores. They also characterized arterial remodeling along fibrosis progression by measuring media to lumen ratio, wall to lumen ratio, and adventitial surface to cross sectional area ratio from TPEF images.

Another important application of SHG/TPEF microscopy is to characterize connective tissues in muscle, tendon and cartilage. Theodossiou *et al* [39] first found that both collagen types I and III can be detected by SHG microscopy in rat-tendon cryosections which demonstrate the possibility of using SHG to assess scar tissue

after injury and surgery. The following studies on tendon and ligaments were more focused on the quantitative analysis where Hu *et al* [70] adopted orientation-dependant gray-level co-occurrence matrix based texture analysis with the estimation of dominant orientation of collagen fibers and Frisch *et al* [71] used fast Fourier transformation and fractal dimension analysis according to the box-counting method. These quantitative measurements were shown to successfully characterize tendons during aging and wound healing. Davies's group reported studies [72, 73] on chicken cartilage by quantifying the principal directionality and dispersion of the collagen fibers in the superficial layer based on Fourier analysis and they successfully showed that these parameters can be used in biomechanical constitutive models. Plotnikov *et al* [74] characterized striation patterns of muscle in SHG images by calculating the local striation spacing and angle of orientation using the imageJ plugin. Garbe *et al* [75] demonstrated a quantification algorithm to extract sarcomere lattice disruption patterns by applying the boundary tensor, which was computed from polar, separable filters in Fourier domain, to the image stacks. Signal phase, direction and energy were extracted from the tensor at different scales and the changes of signal directions on smaller scales referred to the locations of local disruptions of the striation pattern. The morphometry of muscle disease was well characterized in both of these two studies using SHG microscopy.

The study by Zoumi *et al* [76] reported the feasibility of using SHG microscopy to visualize coronary artery microstructures such as collagen, elastin fibril and muscle cells. Kwon *et al* [77] in the following study quantified collagen content within atherosclerosis-prone aortic arch branch points and resistant areas in the murine aortic wall and evaluated its role in regional low-density lipoprotein deposition. The first demonstration of quantitative determination of the myosin filament content using

SHG/TPEF microscopy was reported by Wallace *et al* [78]. The cell volume of mononucleated and binucleated cardiomyocyte was determined after segmentation of TPEF images making use of the well-resolved background and signal peaks in the intensity histogram of the image and the myosin filaments were segmented from SHG images with a fixed threshold. The more recent study by Tsai *et al* [79] used Fourier transform analysis to quantify angle entropy which was shown to increase in atrial fibrillation tissues.

The recent reports by Akins *et al* [80] and Yousefi *et al* [81] showed the ability of SHG/TPEF microscopy to stage pregnancy and predict preterm birth. The fiber size, number of pores, mean pore size, mean spacing between pores, and the fractional area in microns squared covered by the pores were characterized by autocorrelation and particle analysis, which revealed the potential of SHG endoscopic devices for clinical assessment. Another quantitative approach to characterize SHG images was established by Reiser *et al* [82] for intervertebral disk injury where angle index and neighbor index were presented to characterize structural disorder. The angle index was defined as the sum of the differences in the orientation of the index pixel and that of each of its neighbors normalized to the number of neighbors, and neighbor index was calculated as the number of nonparallel neighbors. These indices tend to be good measurements to infer structural information from SHG/TPEF microscopic images.

1.3.3 Image analysis for liver biopsies in clinical studies

Image analysis was introduced into liver biopsy studies in the mid 90s where collagen morphometry was quantified. The earliest study was presented by Kage *et al* [83] to infer that collagen percentage area might be a predictive factor for predicting evolution of fibrosis from chronic hepatitis to cirrhosis in hepatitis C patients based on liver biopsies from 25 patients. Pilette *et al* [84] did a more comprehensive study

on 243 chronic hepatitis C (CHC) patients later to support that collagen percentage area, which was quantified by interactive thresholding from images of picrosirius red stained samples, correlated well with Knodell scores and had a better correlation with serum markers.

Since then, collagen percentage area was recognized as a useful fibrosis morphometry measurement and was included in several studies. O'Brien *et al* [85] further examined 230 liver biopsy samples from CHC patients with Mallory trichrome staining and interactive thresholding method and found that the correlation between collagen percentage area and Knodell score only existed among biopsies with high scores. Furthermore, they reported that fibrosis change among serial biopsy was accurately estimated by collagen percentage area in only 30% of the samples. Similar findings were reported by Wright *et al* [86] using 30 liver biopsies of CHC patients with picro-sirius red staining. An image histogram based peak proportion area change method was developed to quantify collagen percentage area and poor reproducibility was found between different sections from the same core. They suggested possible limitations of the image-based quantification comes from variation in staining intensity, variation in section thickness and real variation in the amount of collagenous tissue within the section. Arima *et al* [87] compared change of collagen percentage area in paired liver biopsy with IFN therapy of 25 patients with HCV infection and reported that fibrosis regression after therapy was better characterized by quantitative analysis than by a semi-quantitative scoring system. Lazzarini *et al* [88] obtained collagen percentage area on 164 trichrome-stained biopsies from untreated patients with CHC using color information for segmentation, and suggested that collagen percentage area was highly correlated with Ishak scores and was capable of differentiating all the stages. Friedenberg *et al* [89] also approached color based

segmentation method according to hue, lightness and saturation to quantify collagen percentage area from images of trichrome stained samples and demonstrated a strong relationship between the collagen percentage area and the Ishak score, although considerable overlaps for intermediate stages of fibrosis were observed as well. Goodman *et al* [90] conducted a study in a cohort of 245 CHC patients where 158 patients were treated with interferon gamma-1b for advanced hepatic fibrosis and 87 with placebo. Collagen percentage area was quantified from unfragmented Sirius red stained biopsy samples of adequate sizes. Both a brightfield RGB image and a grayscale image using crossed polarization filters were captured for each sample. Since only collagen stained with Sirius red had bright birefringence that could be seen in the polarized image, the saturation of the red channel of the RGB image was multiplied by the intensity of the corresponding pixel in the polarized image to calculate collagen content at each pixel location. Their results showed that collagen percentage area overlaps between various stages of the scoring system but it appeared to be a more sensitive tool to demonstrate fibrosis progression than a semi-quantitative scoring system between treated and untreated groups. They further suggested that factors other than the collagen percentage area, such as architectural alteration as well as shunting of blood may be of equal or greater importance than the collagen percentage area. They later reported nonlinear changes in collagen percentage area over time in another study [91] of 346 patients enrolled in the hepatitis C antiviral long-term treatment against cirrhosis (HALT-C) trial.

All these methods are based on the colour information in the stained liver images, thus there is a need for a standard quantification method specially designed for the TPEF/SHG images where no such information is available. We reported one of the first CPA quantification systems for SHG images in Chapter 2. More recently,

Gailhouste *et al* [92] also demonstrated the application of SHG microscopy to quantify liver fibrosis using 119 biopsies from patients with chronic liver disease. The collagen percentage area quantified from SHG images were found to correlate well with Metavir scores, which allows discriminating patients with advanced fibrosis and cirrhosis.

Besides all these studies which aim to demonstrate the role of collagen percentage area for fibrosis diagnosis and drug treatment efficiency evaluation, other works were done to compare collagen percentage area with other non-invasive liver fibrosis diagnostic markers. Calvaruso *et al* [93] evaluated 250 liver biopsies from HCV patients who underwent hepatic venous pressure gradient (HVPG) measurement as well. They found that collagen percentage area had better correlation with HVPG than with Ishak scores and greater changes of collagen percentage area were found when HVPG was low. Their later study [94] suggested that collagen percentage area had better prognostic power than Ishak scores or HVPG to predict clinical outcome in hepatitis C virus infected patients after liver transplantation. Studies from Nitta *et al* [95] and Mori *et al* [96] confirmed that liver stiffness measurement from FibroScan correlated well with collagen percentage area in HCV and NAFLD patients, respectively. On the other hand, Patel *et al* [97] demonstrated that serum biomarkers can differentiate mild from moderate-to-severe fibrosis better than morphometry analysis according to the comparison between FIBROSpectII panel and collagen percentage area on CHC patients. We also explored in this direction to study the correlation between CPA and liver stiffness measurement using SHG images as elaborated in Chapter 2.

Although numerous studies using CPA are investigated, till now, CPA is still not adopted in the routine clinical practice. The major problem, as mentioned in most of

these studies, is that the quantification of collagen percentage area in liver fibrosis study has the limitation of ignoring the architecture changes of collagen patterns along the disease progression. To address this problem, Masseroli *et al* [98] first demonstrated an image analysis approach to quantify collagen percentage area in porto-periportal and septal areas along with vessel and biliary duct lumina area. Several portal tracts regions of one biopsy were manually selected to be imaged and quantified. The collagens were segmented using a global thresholding method defined by Kurita from images of Sirius red stained samples while the contours of porto-periportal and septal areas were manually edited. They claimed that the analysis of the total collagen percentage area in the whole liver biopsy was less precise than their approach by calculation of collagen percentage area in prota-periportal area and excluding the vessel and biliary duct lumina. Significant correlations were shown between their quantifications with Knodell and Scheuer scores from 59 CHC patients. Similar results were reported in their later study [99] to demonstrate that their quantifications provide more objective data on the anti-fibrogenic effects of interferon than semi-quantitative scores. Zaitoun *et al* [100] assessed fibrosis and steotosis in liver biopsies from patients with hepatitis C and alcoholic liver disease, by manually identifying fibrosis and steatosis in peri-central and periportal regions. The collagen percentage area and diameter of fat globules in these two areas were quantified and significant differences were found between hepatitis C and alcoholic liver disease groups. Hui *et al* [101] demonstrated the first study on chronic hepatitis B patients. They manually identified portal-periportal, perisinusoidal and pericentral area and adopted the interactive thresholding method to quantify collagen percentage area in these regions. Excellent inter-observer agreement, significant correlation between quantifications and Ishak scores, and good discriminative power between mild and

advance and with and without cirrhosis was found according to their results. They further investigated their quantifications along with liver stiffness measurement in hepatitis B, hepatitis C and non alcoholic fatty liver disease patients [102]. Higher correlation between Fibroscan and pericelluar fibrosis was observed than periportal or perivenular fibrosis. Sethasine *et al* [103] manually measured number of nodules per millimeter of length of liver biopsy, spetal width and nodule size and quantified collagen percentage area from Masson trichrome stained samples to investigate quantitative histological-hemodynmaic correlations in cirrhosis. They found that collagen percentage area and nodule size could be used to predict clinically significant portal hypertension in cirrhosis patients and collagen percentage area correlated best with HVPG. Kim *et al* [104] further adopted manually septal thickness and nodule size measurements to validate a new scoring system, Laennec system, for sub-staging cirrhosis, where significant increment in the septal thickness and decrement in the nodule size were found. All these studies support the assumption that such pathology relevant approach using pathological features in the quantification improves the analysis; however, the methods to identify such pathological features developed in these studies are performed manually which introduces observer variations back to the analysis and limits the analysis throughput.

The other approach is to adopt novel image features to characterize liver fibrosis along with collagen percentage area. Matalka *et al* [105] developed a collagen segmentation method for images from Van Geison stained samples based on a k-means clustering method using local variance and percent of black pixels in a local region. Fifty-four measurements were then generated including size measures, shape measures, invariants and frequency domain measures of segmented collagen fibers. A neural network was trained to automatically assign a score to the image according to

the 54 measurements extracted. Their system was found to be more accurate in fibrosis diagnosis than collagen percentage area. In another image analysis system proposed by Dioguardi *et al* [106], fractal analysis methods were used to generate a series of fractal-corrected size and shape measures, include fractal dimension and Hurst's exponent of whole tissue section, sizes of collagen islet, collagen percentage area corrected by the fractal dimension, and wrinkled nature of the collagen. They suggested that their system provided the quantitative measurements of the geometric properties and architectural changes of the liver tissue and had the potential to outperform collagen percentage area in liver fibrosis characterization. However, such approach does not directly assess the pathological features and cannot reflect the pathologists' know how which makes it difficult to be accepted by the pathologists. Alternatively, we present a new analysis framework by combing both the automated recognition of pathological relevant collagen patterns and advanced machine learning tools for liver fibrosis assessment as illustrated in Chapter 3.

1.3.4 Liver capsule study and techniques for characterizing collagen network geometry

The entire surface of the liver is covered by a thin layer called the Glisson's capsule, which is mostly composed of dense, irregular connective tissue of typical Type-I collagen fibrils. Liver capsule plays an important role to preserve the integrity of liver, but the correlation between the structures of capsule and liver disease progression is not well studied. The early works were done by Ryoo and Buschmann [107, 108] in rat and human samples respectively where they measured the thickness of liver capsules and studied its correlation with liver fibrosis. It was found that the thickness of liver capsule increases along the fibrosis progression and should be an important indicator of fibrosis which was missed in the routine histology examinations.

However, no further study on large group of samples was performed to validate their preliminary findings of the potential role of liver capsule thickness in diagnosis. Therefore, pathological features from liver capsule and sub-capsule areas are excluded in any of the routinely used semi-quantitative scoring systems nowadays. Chapman *et al* [109] carefully examined the liver capsule in rat, monkey and pike's samples under transmission electron microscope and suggested that the capsule thickness varied depending on the area of the capsule studied and on the animal studied. Our previous study [110] demonstrated the correlation of sub-capsular surface features to the bulk of the liver and the correlation of sub-capsular surface features as well as capsule thickness to fibrosis stages in a rat model, which was consistent with Ryoo and Buschmann's earlier findings. It is also reported that liver capsule can be affected by pathologic conditions from the view of computed tomography and magnetic resonance imaging [111], but both of these imaging modalities were not able to capture the capsule structures in high resolution and the study is qualitative rather than quantitative.

The application of reflective SHG microscopy makes it feasible to image the real collagen network geometry of liver capsule instead of a thick band at the tissue boundary in the conventional way. Although no previous study was proposed to characterize the geometry of collagen network in liver capsule, several techniques were reported to extract collagen network geometry in biopolymer network created in collagen gels. The useful measurements include average pore-size and cross-links. Baradet *et al* [112] first proposed interactive image analysis software to identify collagen network architecture which required human operations. The first automated algorithm was presented by Wu *et al* [113] for backscattered-light confocal images of collagen gels. The collagen network image was segmented first and global maximal

points were identified in the calculated Euclidean distance maps. Medial axes of the fibers were recognized by tracing and connecting these maximal points, followed by post-processing procedures to remove short branches and connect similarly-oriented branches. This algorithm was further verified by Sander *et al* [114] on 3D images of fluorescently labeled collagen gels. Both actual collagen network and artificially generated images of known network structure were used to test the algorithm. Fiber length, persistence length and cross-link density were extracted and fitted in a mechanical model to predict the gel shear modulus. The predicted results were compared to experimental measurement and demonstrated the ability of the proposed algorithm to extract collagen network geometry. Nisslert *et al* [115] developed a skeletonization-based algorithm to identify the gel microstructure from transmission electron micrographs. The image was first filtered with Wiener filter, minimum filter and median filter and segmented. The binary image was skeletonized after removal of small spots and those skeletons with branches shorter than 10 pixels were further removed. The authors also quantified several global measurements such as the distribution of branch lengths and the angles between branches at nodes. To predict the elastic moduli of collagen gels from 2D confocal reflectance microscopy and confocal fluorescence microscopy, Yang *et al* [116] developed a fiber finding algorithm performed on thresholded images by tracing out individual fibers at different widths. Starting from one initial segmented collagen pixel, the fiber was extended to another collagen pixel which fell in a searching window with same size as the fiber width from one to eight pixels if there is no big change of the fiber direction. The number of fibers and the mesh size were characterized and fitted to two mechanical models which successfully predicted the storage modulus of collagen gel according to the experimental results. Another skeletonization-based method was

presented by Luck *et al* [117] to quantify architecture of intermediate filament networks using scanning electron microscopy. The binary image after noise reducing and thresholding was skeletonized by the Avizo package, followed by improving the position of all line segments and merging all closely located cross-links. Total network length per base area, cross-link density, mean segment length and network connectivity were calculated to characterize network morphology and investigate the role of network organisation in regulation of cell elasticity. A recent work was done by Smith *et al* [118] to use open active contours to extract cytoskeletal structures from fluorescence microscopy. The contour of each new filament was initialized by the user and then deformed to minimize the sum of an internal bending and stretching energy and external energy representing constraints from the images. The final contour was further edited by the user for analysis. The method was validated using simulated images of semiflexible polymers of known properties and was used to extract tangent correlation function and curvature distribution from in vitro actin filaments and actin cables images. This method needs a certain level of human interaction and is more appropriate for single fiber or filament tracing. In summary, the key step to extract the collagen network geometry is to identify and locate the medial axis of the collagen fibers, which is very challenging in SHG images due to the disconnected fibers after segmentation caused by the low signal to noise level. We demonstrate a gap filling algorithm to resolve this problem as presented in Chapter 4.

1.4 Outline of the thesis

This thesis is organized as follows: In Chapter 2, we describe how to adapt the conventional quantitative assessment method developed for images from stained samples to the images from non-linear optics microscopy. Chapter 3 explains the details of our innovative pathological relevant approach established for patho-

architecture characterization of liver fibrosis and demonstrates its ability to diagnose fibrosis in the TAA rat model and hepatitis B human samples. In chapter 4, we report the surface quantification of liver fibrosis by establishing a histology index from morphology and texture analysis of liver capsule. Finally, in Chapter 5, we summarize the research work done and discuss future directions of this research.

Chapter 2

Fibro-C-Index, quantitative liver fibrosis assessment using non pathological relevant approach

2.1 Introduction

Liver fibrosis is a result of wound healing responses with resultant accumulation of collagen [1]. Assessment of the severity of liver fibrosis is important for scoring chronic liver diseases, as well as for therapeutic efficacy evaluation.

Liver biopsy remains the gold standard despite risks of staining variation, sampling error, and inter- and intra- observer variations, as it can provide information on inflammatory activity and collagen architecture, that are not obtainable with non-invasive techniques. All the currently adopted non-invasive methodologies such as blood tests, magnetic resonance imaging (MRI) and ultrasound are effective in qualitatively assessing the presence or absence of the disease, rather than assessing precisely the progression of fibrosis in a step-wise fashion [12, 16], due to its specificity and imaging resolution. This limits the clinical usefulness of the tests as it is important to track the progression of disease to predict the eventual timing of the liver function loss and the onset of portal hypertension or other complications which determine proper courses of therapeutic intervention. Liver biopsy has been recommended in the clinical guidance of hepatitis B management as the reference method for diagnosis as well as for assessment of treatment eligibility. The prediction of specific end point in the fibrosis progression from the biopsy has huge impact in

respect to clinical planning, as the detection of significant fibrosis is crucial for antiviral therapies and the identification of cirrhosis affects the treatment entirely as it is now associated to a high risk of cancer.

To minimize observer discrepancies, several studies have reported building automated image analyses systems to quantify the amount of fibrosis for assessment [85, 86, 88-90, 98, 105, 119] , where collagen proportionate area (CPA) is the most widely used feature defined by the percentage of the collagen area over the entire tissue area. As CPA is not addressed in any of the scoring system used by pathologists, we refer it as the non pathological relevant approach in this work. CPA tends to be an objective quantitative measurement with minimized observer variations compared to the semi-quantitative scores. The key procedure to quantify CPA is to segment collagen from the tissue image. Dealing with images acquired from light microscope with stained samples, most of these studies applied collagen segmentation methods according to the color information. However, most of these segmentation algorithms are either simple or not automated, thus are not robust to the images from batch to batch due to the fact that staining variation is unavoidable in most situations.

The advanced imaging modalities such as second-harmonic generation (SHG) microscopy could be the solution for staining variation problem, which is a non-linear optical process specific for imaging fibrillar collagens without the need of staining. SHG exhibits intrinsic advantages over conventional fluorescence imaging as it is a non-linear optical process, requiring no fluorophore presence in tissue; thus, signals are unaffected by dye concentration and photobleaching. Excitation source can be at infrared range, resulting in less scattering in tissues than in the visible wavelength range, and deeper tissue penetration for imaging purposes [120-126].

Thus, in this chapter, we investigated the application of SHG imaging modality for liver fibrosis assessment. As the images obtained using SHG are standardized and highly reproducible, we further established a quantification index system based on CPA, Fibro-C-index, for scoring the progression of liver fibrosis from SHG images. Based on morphological characteristics of collagen development observed, we developed an algorithm to improve the sensitivity of CPA quantification. Our results confirm that CPA quantified from SHG images is useful to monitor liver fibrosis progression in a quantitative way which has the potential to reduce inter- and intra-observer discrepancies from both animal samples and human biopsy samples.

Furthermore, we addressed the potential use of Fibro-C-index as an alternative marker of semi-quantitative fibrosis scores to validate other quantitative non-invasive markers for fibrosis assessment. As discussed, the current available non-invasive methods for liver fibrosis assessment are, by far, not as comprehensive as liver biopsy. Hence, it is necessary to use liver biopsy as a reference to validate any non-invasive markers in the development process. As pointed out by Standish et al [23], the semi-quantitative score is a category assignment rather than a measurement, thus any numerical manipulation of scores is statistically invalid and any further statistical analysis should take this into account. In this manner, Fibro-C-index provides additional value as a quantitative surrogate marker of fibrosis scores to serve this purpose. In this chapter, we validate MRE using Fibro-C-index as the standard for the fibrosis scoring in 32 CHB patients. MRE assesses liver stiffness non-invasively which is the most accurate non-invasive test for detection and staging of liver fibrosis [14-16].

We also reported the limitations of CPA based Fibro-C-index quantification for liver fibrosis assessment which leads to the needs for including other histo-pathological

33

features that are more pathologically relevant, which will be covered in the following chapters.

2.2 Materials and Method

2.2.1 Animal tissue preparation

Male Wistar rats, with initial weight of 200g, were used for the experiment. Animals were housed in the Animal Holding Unit (AHU) of the National University of Singapore (NUS) with free access to lab chow and water in a 12:12 – hour light / dark schedule. Experiments were approved by the Institutional Animal Care and Use Committee (IACUC).

Bile duct ligation (BDL) of rats was performed under general anesthesia with ketamine and xylazine. A midline abdominal incision was performed, exposing the liver and intestines. The lower end of the bile duct is identified at its insertion into the small intestines and traced up towards the porta. The bile duct is then doubly ligated at two areas near the porta with silk sutures and then transacted between the two ligation points. Wound is then closed with double layered tissue closure with vicryl sutures. A total of 15 rats were ligated and sacrificed at intervals of 2, 4 and 6 weeks (n = 5 per week). 5 control rats were also sacrificed at week 0.

Cardiac perfusion with 4 % paraformaldehyde was performed to flush out blood cells and fix the liver tissue before harvesting. Liver specimens from the left lateral lobe were preserved in paraffin and sectioned at a thickness of 50 μm for imaging and of 5 μm for staining and scoring.

2.2.2 Human sample preparation

The study was approved by the institutional review board at National University Hospital, Singapore and all patients gave written informed consent for the study.

Patients with CHB and who underwent MRE of liver and a liver biopsy within a 6-month interval were recruited. A total of 36 patients were recruited. Four patients were excluded due to inadequate liver biopsy samples. Finally 32 patients (20 males and 12 females) formed the study group.

Percutaneous liver biopsies were performed by experienced radiologists under local anesthesia using ultrasound for guidance. Biopsies from the right anterior lobe of liver were obtained using an eighteen gauge core biopsy needle with one to three passes. The samples were fixed immediately in formalin and sent to the pathology. The liver biopsy samples were processed using standard techniques.

2.2.3 Histo-pathological scoring

Animal tissue samples were stained with Masson's Trichrome (MT) stain kit (ChromaView advanced testing, #87019, Richard-Allan Scientific) and imaged (IX51, Olympus). Animal tissue scoring was performed using modified Ruwart score according to Boigk et al. as there was extensive bile duct proliferation noted [127, 128], making the modified Ishak score unsuitable.

The human biopsies were stained with hematoxylin and eosin and Masson's trichrome. The histologic staging of fibrosis was performed by an experienced hepatopathologist with more than 20 years' experience in liver pathology using the METAVIR system as follows: F0, no fibrosis; F1, portal fibrosis without septa; F2, portal fibrosis with few septa; F3, numerous septa without cirrhosis; and F4, cirrhosis.

2.2.4 TPEF/SHG microscopy

The TPEF/SHG microscopy was developed based on a confocal imaging system (LSM 510, Carl Zeiss) using an external tunable mode-locked Ti:Sapphire laser (Mai-Tai broadband, Spectra-Physics). System is shown in **Figure 2**, where laser was

passed through a pulse compressor (Femtocontrol, APE GmbH, Berlin, Germany) and an acousto-optic modulator (AOM) for group velocity dispersion compensation and power attenuation respectively. The laser was then routed by a dichroic mirror (DM1, 490 nm), through an objective lens, to the tissue sample. TPEF emission generated in tissue was collected by the same objective lens and recorded by a photo-multiplier tube (PMT), after passing through the dichroic mirror (DM2) and a 700 nm short-pass filter (BP1). SHG signal was collected using a high numerical aperture (NA) condenser and filtered by a 450 ± 10 nm band-pass filter (BP2) before entering PMT (Hamamatsu R6357) for detection. With the intrinsic optical sectioning characteristics for non-linear optical process, the pinhole function of the confocal microscope was not used. A total of 4 SHG images (~ 4.1 x 4.1 mm) were scanned for each animal tissue specimen. Up to 10 SHG images (~ 1.3 x 1.3mm) were scanned for each human biopsy sample to cover all the tissue areas.
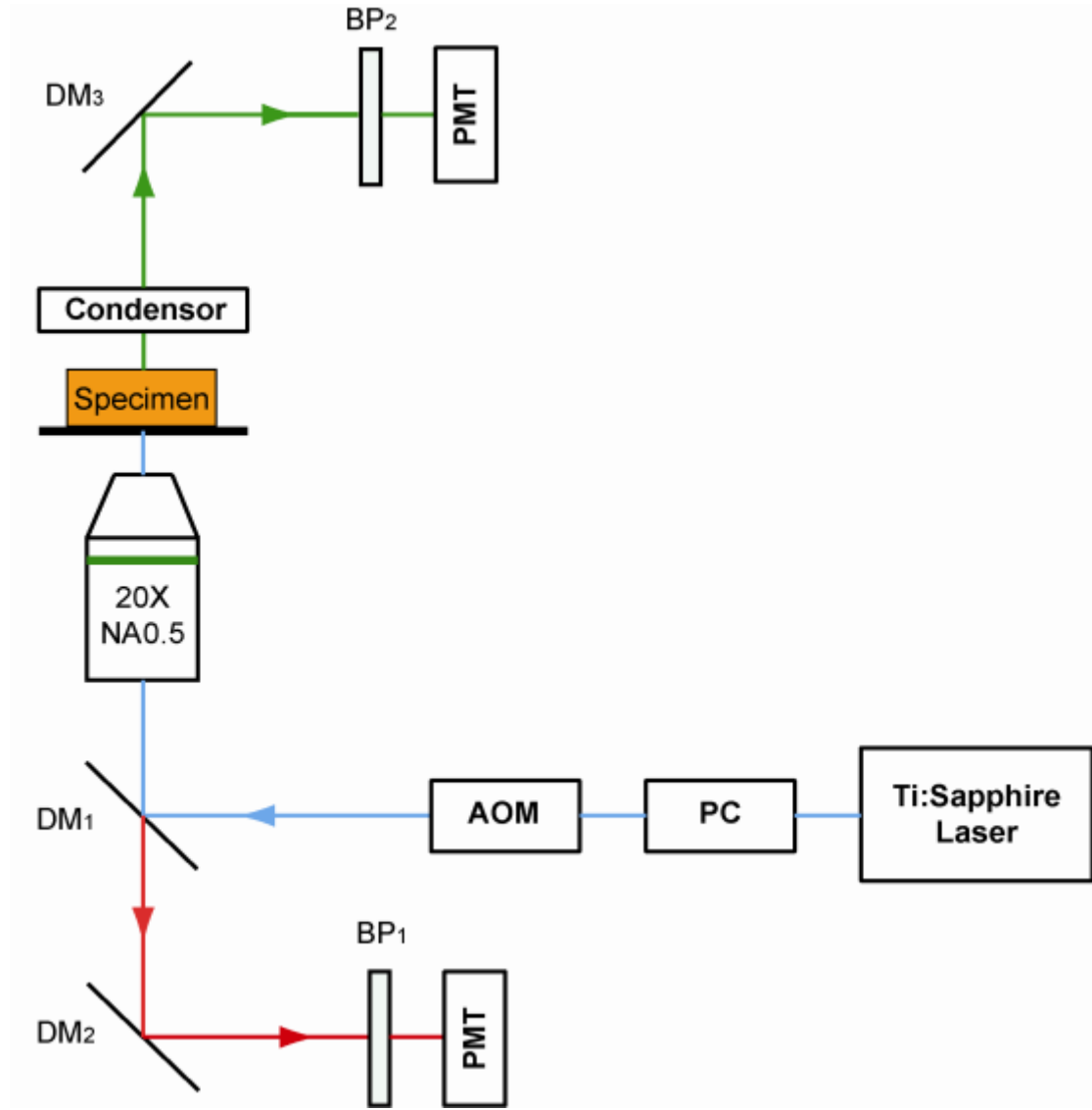
Figure 2: Schematic illustration of the TPEF/SHG microscope system used in the study.

2.2.5 Fibro-C-Index

We proposed a standardized quantification indexing system, Fibro-C-Index, for staging the progression of liver fibrosis, by measuring collagen proportionate area from the SHG microscopy images. A quantification algorithm for collagen segmentation is developed as illustrated in **Figure 3**. The algorithm utilizes images acquired using both TPEF and SHG microscopy. Dark background images pre-acquired before the experiment were subtracted from raw images, for both TPEF and

SHG channels. TPEF image was categorized into 3 different groups depending on pixel intensity: completely dark, dim, and bright which represent areas of vessel or outside-tissue-space, bile duct cannaliculi, and all other cells respectively. Threshold levels used here were found by identifying local minima from the pixel intensity profile of the entire TPEF image, given the significant intensity variation among 3 different groups. Once these areas were identified, a mask was created from segmented TPEF image. Various weights were subsequently assigned to these areas depending on the likelihood of collagen aggregation in these areas. A weight, α, was assigned to areas representing the border of blood vessels as well as inside the bile duct cannaliculi while the rest of the image was assigned with an unity constant, 1, to create a weight map. The value of weight constant, α, was then determined systematically by examining the adaptive quantification results between early and late stages of liver fibrosis such that the quantification result difference is greatest. Once the optimal α was determined, the weight map was multiplied to SHG image, followed by Otsu segmentation [129], erosion, and dilation [130] to create a final mask. By applying a final mask on the raw SHG image, we obtained an image representing the collagen content in the tissue sample where the collagen proportionate area was calculated and was named as Fibro-C-index.
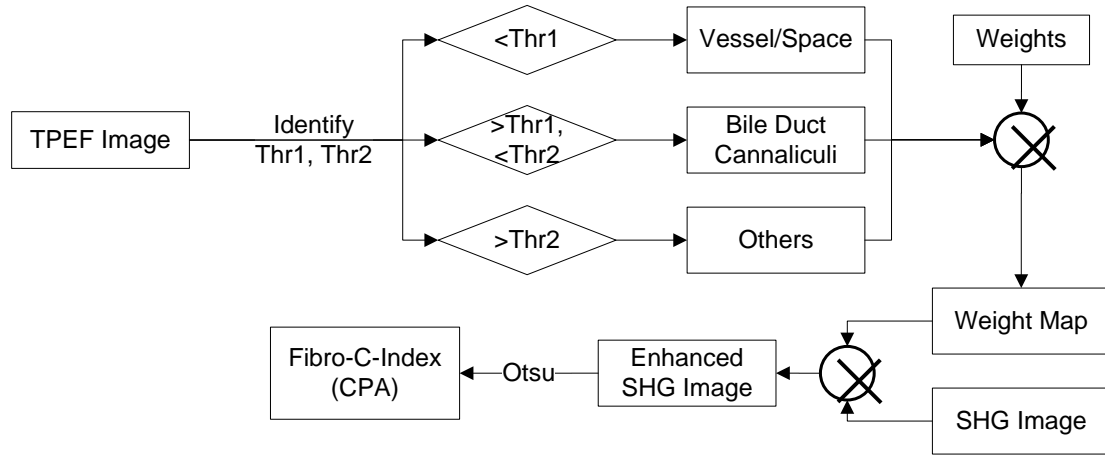
Figure 3: Flow Chart of the adaptive quantification algorithm.

The SHG images were also analyzed using the direct segmentation method for comparison purposes. The direct segmentation algorithm is described as follows: background in the images was removed by subtracting a pre-recorded background image, and then images were segmented using the Otsu method. Residual grainy noise was removed using erosion and dilation functions.

Moreover, to make a standardized comparison across all tissue samples, all images were collected using the same parameters (PMT gain and laser power). Fibro-C-Index was later used to compare the results obtained using conventional histopathological scoring.

For human samples, the normal collagen from liver capsules and around the big portal tracts and central veins which did not contribute to fibrosis was identified by an experienced pathologist and excluded from the Fibro-C-Index. All the parameters were set as same as those used in the animal study.

2.2.6 Magnetic resonance elastography (MRE)

MRE of the liver was performed with a standard MRE technique as described previously [131] on a 1.5 Tesla clinical MR scanner. MRE was performed with

standard liver MRI protocol after 6 hours fasting. MRE was performed in supine position with a 19-cm passive driver placed over right lower chest wall and upper abdomen at the xiphisternum level so as to lie directly above the right lobe. The passive was connected to an active driver placed outside the MRI scanner via a 7.6 m long plastic tube. Shear waves were produced in the upper abdomen and liver by continuous acoustic vibrations at 60Hz generated by the active driver. The MRE sequence was a standard GRE based sequence as described in literature [131]. The liver stiffness values were calculated by placing regions of interest (ROI) on the automatically generated stiffness maps. ROIs were placed on the region of right anterior lobe so as to correlate with biopsy region sampled and a mean liver stiffness value obtained for each patient and expressed in kilopascals (kPa).

2.3 Results and Discussions

2.3.1 Qualitative assessment of liver fibrosis progression in animal samples

SHG and TPEF microscopies were used to detect changes in collagen as well as the hepatocyte and bile duct morphology; and compared with results obtained from modified Ruwart scoring [127, 128]. **Figure 4** shows changes in collagen using Masson's Trichrome staining (A − D) and the combination of SHG and TPEF microscopies (E - H). Readers can refer to the modified Ruwart scoring system for a detailed definition of the scoring system [127, 128]. In normal livers, hepatocytes were healthy and the presence of collagen was minimal. As the animal model progressed, stage 1 fibrosis with an increase in pericellular collagen without the formation of septa was seen (**Figure 4A, E**). At about 3-4 weeks after BDL, proliferation of bile duct appeared as dim regions in the SHG/TPEF images. Stage 2 collagen aggregations formed incomplete septa from portal tract to central vein (**Figure 4B, F**). By week 6, profuse proliferation of bile ducts could be observed all

over the tissue sample (**Figure 4C, G**). Complete but thin collagen septa interconnected with each other to divide the parenchyma into separate fragments in stage 3 fibrosis. Late fibrosis (stage 4) was observed in some animals after 6 weeks, where thick collagen septa were observed, forming complete cirrhotic nodules (**Figure 4D, H**). Unique to the BDL model, was the amount of bile duct proliferation and collagen aggregating around the bile ducts, shown as dim regions.
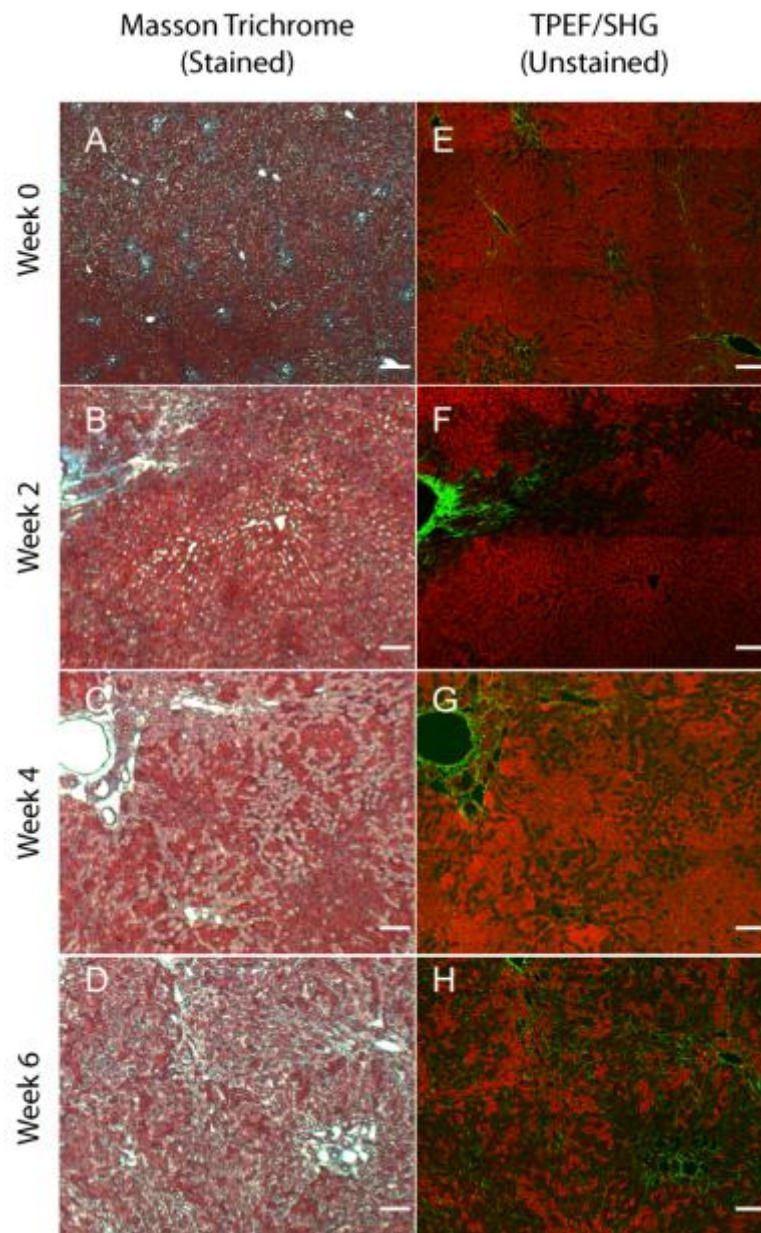
Figure 4: Fibrosis progression at different time points after BDL imaged by conventional MT staining (A-D) and SHG/TPEF microscopy (E-H).

The BDL model used in this experiment successfully induced fibrosis progression in livers over a period of 6 weeks. Pathological development of liver fibrosis, including changes in collagen fibers, bile duct cannaliculi, and hepatocyte morphology, could be clearly recorded by SHG/TPEF imaging without the need for tissue staining.

2.3.2 Fibro-C-index: Quantitative assessment of liver fibrosis progression in animal samples

Our group has previously developed a quantification algorithm using the SHG/TPEF system, in which images and quantification were processed without emphasis on the typical morphological features seen in the images [41]. When the original algorithm was applied to the BDL model, a small amount of the collagen presence was removed after segmentation, as their signal levels are equivalent to the noise levels. To improve the system's sensitivity, we have incorporated morphology information for quantitative fibrosis assessment.

We developed an algorithm specifically for the BDL model using insights gained from collagen progression observed in **Figure 5**. Collagen was noted to aggregate around blood vessels and bile ducts in our BDL model. By enhancing SHG signals in these regions before applying Otsu segmentation, we could retain fine collagens with low intensity level. A comparison between direct segmentation algorithm and proposed quantification algorithm is shown in **Figure 5**. In **Figure 5A**, the raw TPEF/SHG image was shown, and the area pointed by the white arrow appeared to be fairly empty. The binary mask where the low intensity SHG signals were enhanced is shown in **Figure 5B**. The processed images using a direct Otsu segmentation algorithm and the proposed quantification algorithm were shown in **Figure 5C** and **5D** respectively. There was much more collagen in the same area when the proposed quantification algorithm was applied instead (**Figure 5D**). A series of weights ($\alpha = 1$,

50, 70, 100) were applied in the proposed quantification algorithm and the results are summarized in **Figure 5E**. In order to determine the optimal weight, α, a sensitivity analysis was done based on the quantification results between week 2 and week 6. The ratio (quantification results of week 6/week 2) was calculated systematically for α = 1 - 110 (**Figure 5E**). The SHG image was taken as 12 bit with the maximum intensity at 4095. As the SHG signal intensity to be enhanced in the region is around 20-30, it would not be over saturated after being multiplied by α in such range. In this analysis, it was found that when α = 70, the proposed algorithm is most sensitive for differentiating between early and late stages of liver fibrosis. Area of collagen identified is 4 to 6 times higher than that obtained with the direct segmentation algorithm (α = 1, **Figure 5F**). For the subsequent results presented in this study, α was chosen to be 70. The proposed algorithm developed here further enhanced the sensitivity of SHG for detecting collagen contents, specifically for BDL model.
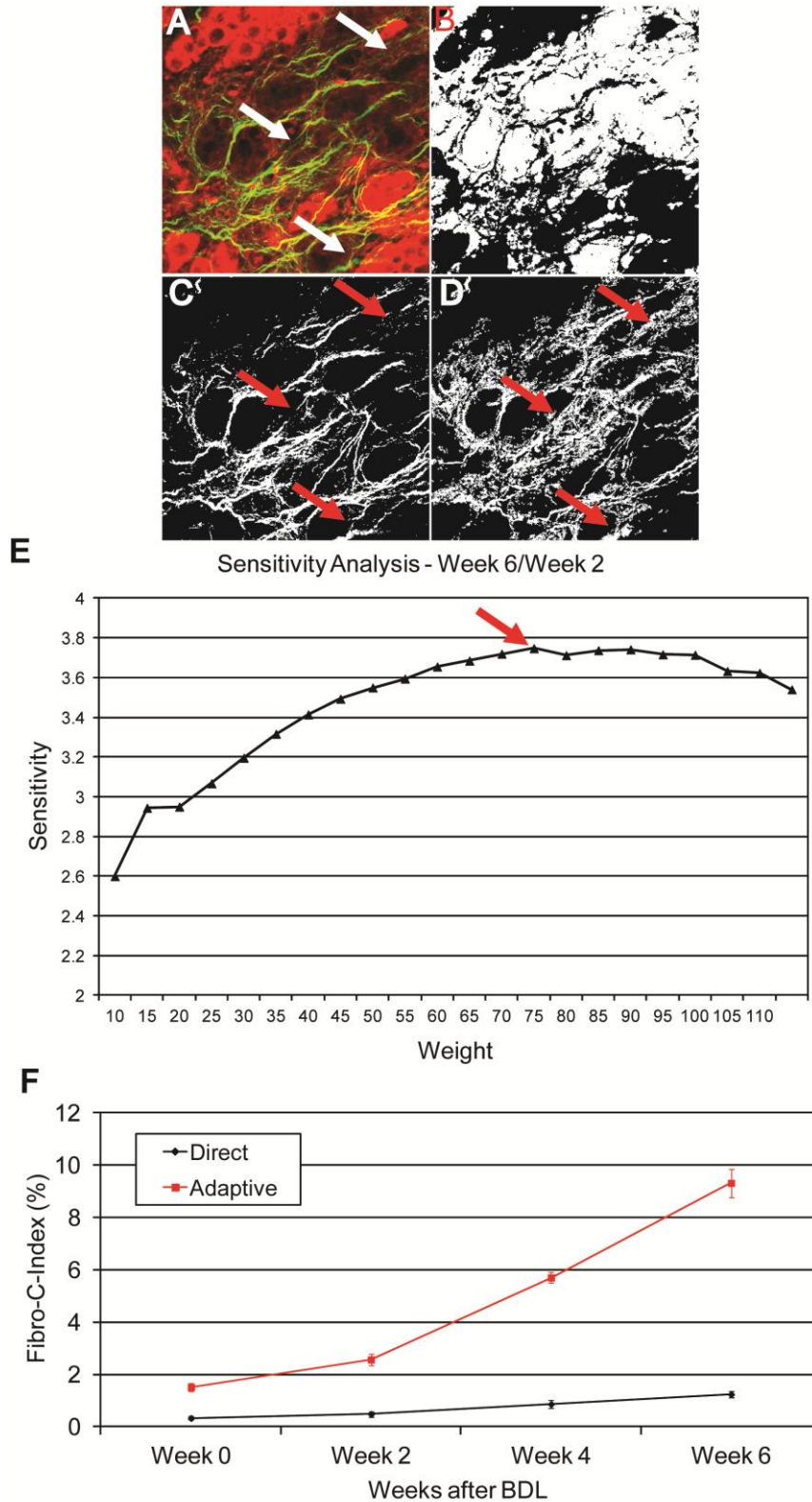
Figure 5: Comparison between direct and proposed quantification algorithms. The TPEF/SHG image of a typical region in the fibrotic liver is shown in (A), and the mask of the signal enhancing regions is shown in (B). The processed images using direct thresholding and proposed methods are shown in (C) and (D). The weight used in adaptive method is optimized as shown in (E) where the quantification results of Fibro-C-Index using two methods are compared in (F).

We then validated Fibro-C-index by comparing it with the conventional assessment technique using a histo-pathological scoring system. Fibrosis was scored in four different stages, 1, 2, 3, and 4. Staging results from tissue samples acquired at different time points (week 0, 2, 4, 6 after BDL) are shown in **Figure 6**. We then compared the histo-pathological results against the Fibro-C-Index detected using SHG microscopy and the optimized quantification algorithm (**Figure 7**). There is clear overlap of Fibro-C-Index between different stages: in early stages (1 & 2), overlap occurs by as much as 50%; in later stages (3 & 4), this problem was even more significant, with almost no difference in the Fibro-C-Index in the 2 groups. Within each stage, Fibro-C-Index varies from 11% to 45%.
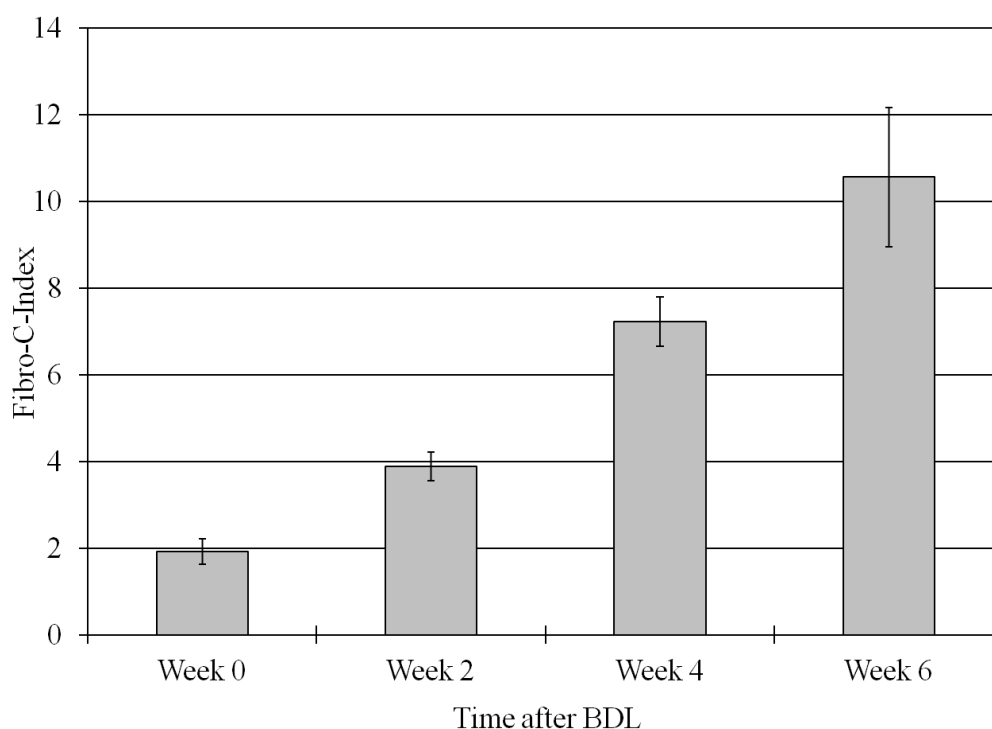
Figure 6: The Fibro-C-Index quantified at different time points after BDL.

On one hand, the high degree of overlap between the amount of liver fibrosis between stages and the variability of Fibro-C-Index within each stage clearly illustrates the

problems of inter- and intra- observer discrepancies when a qualitative staging system is used [32-34, 132, 133]. On the other hand, since Fibro-C-Index is not specifically addressed in any of the scoring systems, we should also question that whether Fibro-C-Index alone is good enough to characterize liver fibrosis progression given that histo-pathology scoring remains the gold standard.
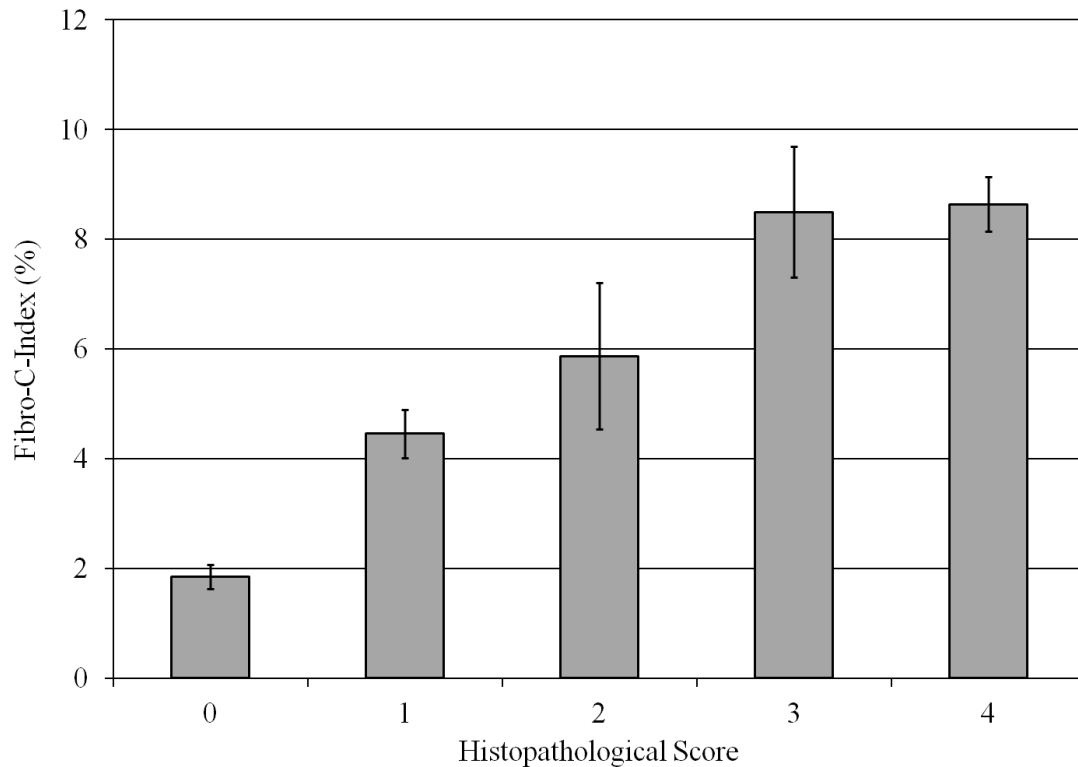
Figure 7: Investigation of Fibro-C-Index (CPA) at different fibrosis stages. The overlap of collagen proportionate area is clear between different fibrosis stages.

2.3.3 Fibro-C-index: Quantitative assessment of liver fibrosis progression in human samples

We then applied Fibro-C-index on 32 biopsy samples from CHB patients (**Figure 8**). The mean age $\pm$ SD of the study group was 46 years $\pm$ 12.2 years. The mean body mass index of the study population was 24.3 Kg/m^2 (95%CI, 22.8 – 25.7, range 18.6-32.7). The mean cumulative biopsy length was 22mm (95% CI, 19.5-24.3mm, range

11-33mm). The histological stages of fibrosis were F0 in 5, F1 in 10, F2 in 4, F3 in 5 and F4 in 8 patients.
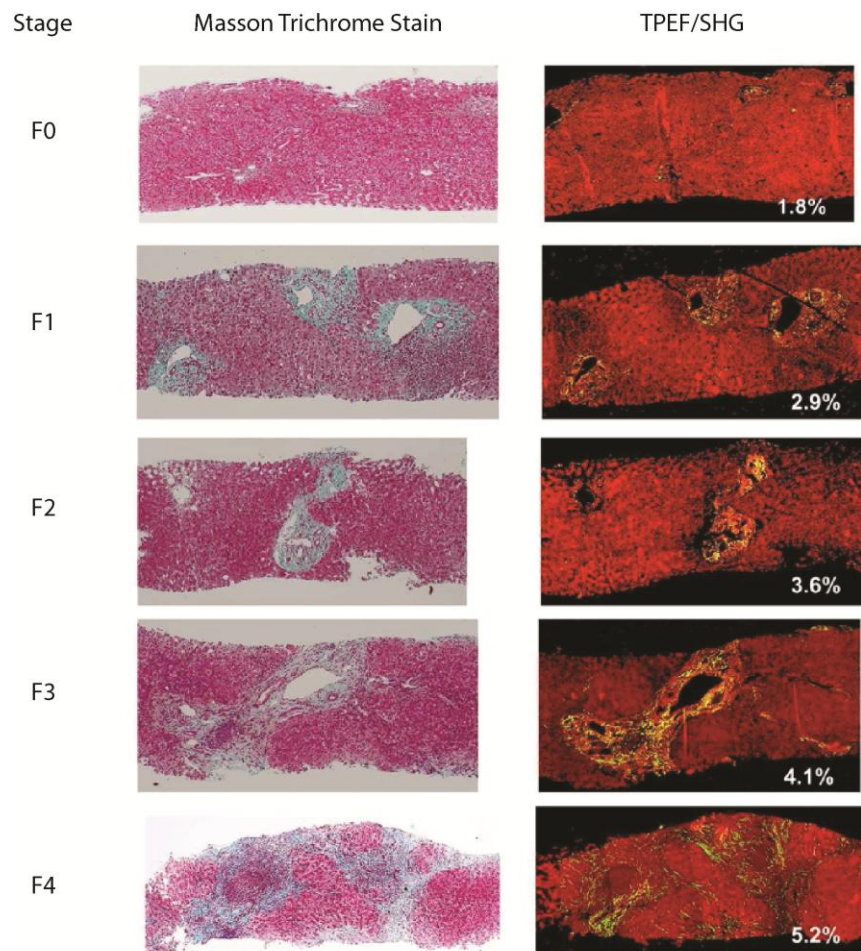
Figure 8: The fibrosis progression at different stages in Hepatitis B patients imaged by conventional MT staining and SHG/TPEF microscopy. The Fibro-C-Index value was calculated for each SHG/TPEF image as shown.

The mean Fibro-C-index of the study population was 2.5% (95% CI, 1.8%-3.2%, range 0.6%-7.4%), which showed increasing trend with stages of fibrosis (**Figure 9A**). There was significant correlation between fibrosis stages and Fibro-C-index (rho=0.80, 95% CI, 0.63-0.89, p<0.0001). A Kruskal-Wallis test showed significant differences in Fibro-C-index (p=0.003) among different stages of fibrosis. However, a trend of small incremental increase was observed in earlier stages of fibrosis. These

results are similar to an earlier observation in a study with morphometric quantification of liver fibrosis using stained samples [23].

Figure 9: Fibro-C-Index and MRE values of 32 Hepatitis patients are shown in (A) and (B) respectively. The correlation between Fibro-C-Index and MRE values are assessed in (C).

2.3.4 Correlation between Fibro-C-index and MRE

The mean time interval between liver biopsy and MRE was 83.8 days (95% CI, 60.6-107 days, range 2-180 days). MRI was successful in all the study subjects. The mean
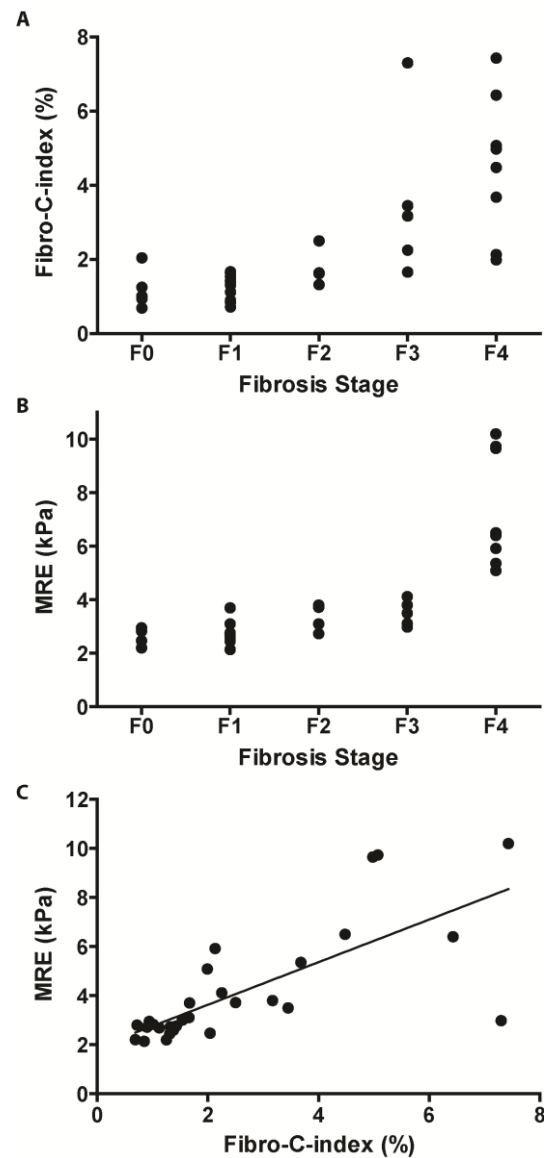
liver stiffness of the study population was 3.98 kPa (95% CI, 3.2-4.8 kPa, range 2-10.2 kPa).

Similar to Fibro-C-index, MRE also showed increasing trend with stages of fibrosis (**Figure 9B**). A significant positive correlation existed between Fibro-C-index and MRE (r=0.82, 95% CI, 0.66-0.91, p<0.0001) (**Figure 9C**). ROC analysis results showed MRE performing slightly better (but not statistically significant) than Fibro-C-Index in the detection of ≥F1 (0.87 vs. 0.81, P=0.67), ≥F2 (0.95 vs. 0.94, P=0.78), ≥F3 (0.98 vs. 0.96, P=0.76) and F4 (1.00 vs. 0.92, P=0.10).

In a previous study, liver stiffness evaluated with TE in CHB patients, correlated with collagen proportionate area using picosirus red for collagen and digital morphometric analysis with a photomicroscope [102]. In this study, only 5 periportal fields, 5 perivenular fields and 15 random pericellular fields were evaluated, therefore not a complete evaluation of fibrosis burden in the specimen. The correlation of stiffness with TE was made with pericellular, periportal and perivenular fibrosis. The correlations were reported to be statistically significant but low (r=0.43, 0.21 and 0.25 respectively). In our study, the correlation coefficient was much higher (r=0.78) than the previous study. This is probably due to the adoption of Fibro-C-index method, which is capable of evaluation of the whole biopsy specimen when only large vessels and subcapsular region were excluded. Fibro-C-index provides a relatively accurate estimation of degree of fibrosis as compared to histological staging.

2.4 Conclusions

Without varying factors such as staining quality and photobleaching [40, 41], quantification from SHG/TPEF microscopy images is highly reproducible and can be used as a standardized platform for assessing progression of liver fibrosis in a continuum. We have developed and validated Fibro-C-index method for SHG

microscopy images based on the morphological characteristics of collagen development observed in BDL model. Collagen proportionate area was calculated at same set time points (week 0, 2, 4, 6 after BDL) and correlated to histo-pathology scores. We also validated Fibro-C-index in a pilot study using 32 biopsy samples from CHB patients. It is also shown that Fibro-C-index has the potential to be used as a quantitative alternative of histo-pathology scores to validate other non-invasive fibrosis markers such as MRE.

These findings suggested that collagen proportionate area (Fibro-C-Index), as a quantitative measurement, has the potential to minimize the intra- and inter-observer discrepancies by providing a standardized indexing system which was consistent with other reports. By including SHG/TPEF imaging and quantification of collagen proportionate area as a part of the scoring criteria, we anticipate that the time required for diagnosis can be significantly reduced by removing the need of tissue staining (which takes at least 4 hours), and more importantly, intra and inter-observer discrepancies can be eliminated. On the other hand, we also reported the limitation of using collagen proportionate area to accurately predict fibrosis stages as it lacks histo-pathological information used by pathologists, which requires more advanced image analysis techniques to characterize other collagen architectural patterns that are more pathologically relevant.

Chapter 3

*q*Fibrosis, quantitative liver fibrosis assessment using pathological relevant approach

3.1 Introduction

Excessive accumulation of extracellular matrix (ECM) results in fibrosis, which is the hallmark of chronic liver diseases (CLD) [1]. Progression of liver fibrosis is closely related to the development of major complications of CLD [134]. Chronic hepatitis B (CHB), a leading global health burden, is the major cause of cirrhosis and liver cancer [135]. With recent advances in efficacious antiviral therapies, the endpoint of fibrosis/cirrhosis regression can be achieved in long-term treatment of CHB [136]. Herein lies an increasing need for accurate and precise assessment of fibrosis, a prognostic indicator of chronicity and CLD sequelae, in order to facilitate and monitor the effective utilization of therapeutic advances [137].

Liver biopsy has long been the gold standard for fibrosis assessment in CLD [138]. It has the capability of providing histopathological information on various morphological parameters that have been clinically validated for their pathophysiological relevance, but are not obtainable with non-invasive techniques [139, 140] such as liver stiffness measurements [6] and biochemical markers [141]. Currently, liver biopsy-based assessment remains the standard reference for monitoring therapeutic responses in both clinical research trials and actual practice [23, 136].

However, conventional histological staging of fibrosis in liver biopsy is semiquantitative and highly subjective to sampling error and observer variations, as it basically relies on a global assessment of architectural distortion and associated fibrosis. It cannot sufficiently and reliably reflect the complicated pathophysiological/functional status of the liver, which is incumbent for diagnostic decision-making in current CLD management [32, 137]. Furthermore, cirrhosis has recently been redefined to be a dynamic process with intra-stage progressive/regressive changes [142]; in this regard, the International Liver Pathology Study Group has called for biopsy-based histological markers that can quantify and predict intra-stage cirrhosis changes [143]. Thus, technologies that can provide feasible solutions to these issues may potentially improve fibrosis assessment in CLDs such as CHB.

Image-based morphometric analysis of biopsy samples has been explored as an alternative to histological staging systems [93]. The current method of choice is collagen proportionate area (CPA) measurement, which quantifies the extent of collagenous ECM deposition without incorporating architectural information about the damaged tissue landscape [91-93] as elaborated in Chapter 2. CPA correlates well with late stages of fibrosis but is highly sensitive to sample size [20]. Clinical applicability of CPA is still being critically evaluated.

The strengths and limitations of current assessment systems motivated us to develop an innovative method- *q*Fibrosis for liver biopsy assessment, based on the strategy of combining pathology-relevant collagen architectural features with automated computer-aided image analysis tools. With input of imaging data from liver sample, *q*Fibrosis is able to automatically compute the fully-quantitative fibrosis scores of the respective collagen architectural features. Such a strategy may potentially solve some

of the current issues encountered in biopsy-based histological fibrosis assessment with a more accurate and objective quantitative methodology. Thus, in this Chapter, we sought to establish *q*Fibrosis and to verify its potential as a fibrosis assessment tool in both animal model and CHB patients.

3.2 Materials and Method

3.2.1 Animal tissue preparation

Thioacetamide (TAA)-induced animal model is used for studying liver fibrosis in rats since it has similar characteristics as that caused by viral hepatitis in humans [144]. Similar histopathological changes are found in humans and TAA-induced animals which make it a valid model to study liver fibrosis progression in chronic hepatitis B [145, 146].

All the protocols for studying the TAA-induced liver fibrosis rat model were reviewed and approved by the Biological Resource Centre (BRC) Institutional Animal Care and Use Committee (IACUC). Male Wistar rats with an average weight of 220g were housed two per cage in BRC of Biopolis A*STAR with free access to laboratory chow and water in a 12:12h light/dark schedule. The rats were administered with intra-peritoneal (ip.) injections of TAA 200mg/kg of body weight with PBS, three times a week. Twenty-five rats were randomly separated into five groups, representing 5 time points, without drug treatment, and treated with TAA for 4, 8, 10 and 12 weeks.

Liver specimens from the left lateral lobe of each animal were formalin-fixed, paraffin-embedded and sectioned at a thickness of 50 μm for imaging, and at 5 μm for staining with haematoxylin and eosin and Masson Trichrome (a connective tissue

stain) for histological examination. Scoring was performed by an experienced pathologist using the Metavir staging system (F0=no fibrosis, F1=portal fibrosis without septa; F2=few septa, F3=numerous septa without cirrhosis, and F4=cirrhosis) [27].

3.2.2 Human sample preparation

In this study, clinical biopsy samples from two independent cohorts were included: 107 non-fragmented liver core biopsies for algorithm training and testing, and another well-balanced 55 long biopsy samples for demonstrating the technology reproducibility. Both cohort samples were from CHB patients in Nanfang Hospital (Guangzhou, China). The clinical study was conducted according to the Declaration of Helsinki guidelines and approved by the Ethical Committee of Nanfang Hospital. All patients have given written informed consent for liver biopsy as well as permission for use of their medical records. The average length of the 107 biopsies was 16.7 ±5.4 mm (minimum length: 10 mm, maximum length: 30 mm). The average length of the 55 biopsies was 30.4 ± 4.4 mm (minimum length: 25 mm, maximum length: 44 mm).

Table 2: Number and length of biopsy samples of chronic hepatitis B. Data are Mean ± SD.

	Metavir Fibrosis Score				
	F 1	**F 2**	**F 3**	**F 4**	**Total**
	Length ≥ 10 mm				
Number	18	19	27	43	107
Length (mm)	17.50 ±5.64	16.32 ±6.93	17.96 ±5.80	15.79 ±4.07	16.72 ±5.38
	Length ≥ 15 mm				
Number	12	9	18	30	69
Length (mm)	20.42 ±4.44	22.00 ±5.96	20.89 ±4.83	17.53 ±3.47	19.49 ±4.64
	Sample with complete clinical measurements				
Number	9	11	11	18	49
Length (mm)	15.89 ±3.72	19.09 ±7.40	19.36 ±6.82	15.28 ±4.13	17.16 ±5.75

All the liver biopsy specimens were routinely processed by formalin fixation and paraffin-embedding, and sectioned at 5 μm thickness for SHG-imaging, and then stained with Masson Trichrome for histological assessment. Biopsy samples were read independently by one hepatopathologist and one junior pathologist, and staged using Metavir and Ishak fibrosis scoring systems. The detailed distribution of all biopsies, together with their Metavir fibrosis stages is summarized in **Table 2**.

3.2.3 Image acquisition

The 107 samples for training and testing qFibrosis were imaged by the system of second harmonic generation/two photon excitation fluorescence (SHG/TPEF) microscopy established and adjusted as previously reported in Chapter 2. Image acquisition was performed with a 20 × objective on unstained sections of the tissue samples. To cover most of the sample areas, 3 of nine-by-nine multi-tile images were acquired for the animal samples with a final image size of 16 mm^2 (4 × 4 mm); and up to 10 three-by-three multi-tile images for each human biopsy sample with final image size of 1.8 mm^2 (1.35 × 1.35 mm). The additional 55 samples for reproducibility demonstration were imaged by Genesis system (HistoIndex, Singapore), a SHG/TPEF technology-based commercial device, at Southern Medical University (Guangzhou, China). Image acquisition parameters for these samples were set the same as the ones for the former cohort samples.

3.2.4 Establishment of qFibrosis

The procedure for establishing qFibrosis includes (i) identification of different collagen patterns, (ii) extraction of collagen architectural features, and (iii) statistical analysis of features of the respective collagen patterns, which were then combined into a single index.

55

The acquired images of samples were processed and calculated with the established *q*Fibrosis. A numerical value between 0 and 1 will be assigned to each sample while the higher value indicates more severe fibrosis.

3.2.4.1 Identification of portal, septal and fibrillar collagen

Automated image processing algorithms were developed to identify and differentiate portal, septal and fibrillar collagen (**Figure 10**).

The TPEF image (**Figure 10A.1**) was first used to locate the tissue samples into several region-of-interests (ROIs) while each ROI represents one portal tract or central vein region. Since the TPEF image records the autofluorescence signals of the liver tissue (hepatocytes), the portal tracts and central veins were shown as empty spaces in the TEPF channel image. These portal tracts and central veins were then identified on TPEF images by thresholding (**Figure 10A.1-A.2**). The segmentation process started with determining a threshold (5% of the maximum pixel intensity) separating those pixels belonging to portal tracts and central veins based on their intensity values. Next, we smoothed the spaces by applying morphological closing and hole-filling operations [148] (**Figure 10A.2-A.3**). We then removed spaces that were smaller than 100 μm^2 (size of one hepatocyte) and spaces with large major-axis-length to minor-axis-length ratio (which were assumed to be sinusoidal spaces) before further processing (**Figure 10A.3-A.4**).

Under normal circumstances, the portal tract contains three lumens, comprising one hepatic vein, one hepatic artery and one bile duct. However, we often encountered more lumens in a portal tract due to issues such as direction of tissue sectioning. Therefore, we considered those segmented spaces which were very close to each other as denoting one portal tract versus one central vein; after which we merged the spaces

into one ROI. We did this by generating a Delaunay triangulation diagram [149] treating the centre of each segmented space as a node and by connecting all nodes to their immediate neighbouring nodes such that there is no node inside any of the triangles formed (**Figure 10A.5**). We then merged small triangles by applying a threshold that equals the average length of all edges in the triangulation, and combined those nodes with triangle edge length smaller than the threshold. For each merged group, we created a larger space by essentially connecting individual spaces and covered all individual spaces using convex hull filling (**Figure 10A.5-A.6**).

After merging all nodes with triangle edge length less than the threshold, we updated the Delaunay triangulation diagram and used these new nodes to create a Voronoi diagram [149] (**Figure 10A.6-A.7**). For each ROI, we considered the node as either the portal tract or central vein region.

The collagen was then segmented from the SHG images (**Figure 10B.1 – 10B.2**) using a segmentation algorithm based on Gaussian mixture models [147]. The segmented collagen in each of the ROI (**Figure 10C**) was next differentiated into portal, septal and fibrillar collagen.
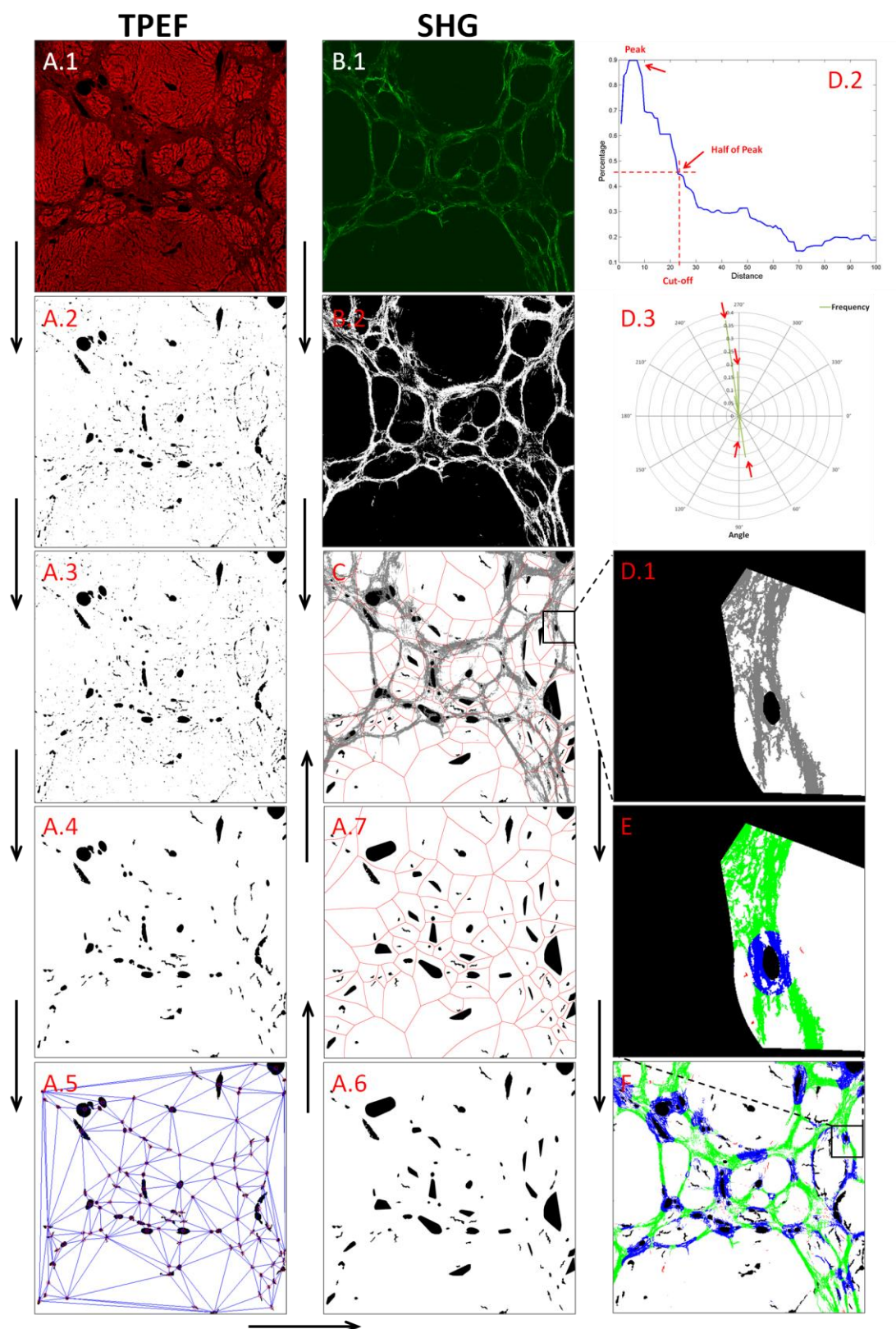
Figure 10: Diagram of image processing procedures to identify portal, septal and fibrillar collagen. The empty spaces in the TPEF image (A.1) was first segmented (A.2), smoothed (A.3) and the small holes were then removed (A.4). The Delaunay triangulation (A.5) was performed on the segmented vessels and veins and the closing

vessels and veins were merged together (A.6). The Voronoi diagram was next generated to form several region-of-interests each representing a portal tract or central vein region (A.7). The SHG image (B.1) was segmented to identify the collagen regions (B.2). The segmented collagen in each of the ROI (C) was next differentiated into portal, septal and fibrillar collagen. (D.1) shows one ROI as example, and the collagen distribution along the distance to the vessels was shown in (D.2) to figure out the cut-off value to identify portal collagen. The collagen distribution along different directions was then shown in (D.3) to find the local maxima which identifies the septal collagen. The identified portal, septal and fibrillar collagen in ROI (D.1) were illustrated in (E), where portal collagen is coded in blue, septal collagen in green and fibrillar collagen in red. The identified three collagen patterns in the entire image was demonstrated in (F).

In order to illustrate the definitions of portal, septal and fibrillar collagen, we use one ROI as an example (**Figure 10D.1**). To identify portal collagen, the percentage of collagen pixels measured at various distances from the boundary of the portal tract or central vein is shown in **Figure 10D.2**. A cut-off distance was chosen when the percentage of collagen pixels decreased to half from the maximum percentage. All the collagen within the cut-off distance was considered as portal collagen (blue, **Figure 10E**). For septal collagen, we measured the direction profile of the remaining collagen and the result is shown in **Figure 10D.3**. We then identified the local maxima of the collagen direction profile (red arrow, **Figure 10D.3**) and considered all collagen at these particular angles as septal collagen. Lastly, we interpreted all the remaining collagen as fibrillar collagen (red, **Figure 10E**). The same processing was performed in each of the ROI in the image and the overall collagen was separated into portal, septal and fibrillar collagen completely (**Figure 10F**).

3.2.4.2 Collagen feature extraction

*q*Fibrosis can quantify the morphological features of all the collagen patterns described above for accurate assessment of fibrosis. We labeled all collagen in each ROI as portal, septal or fibrillar collagen and extracted features for each group

separately. The detailed procedures for collagen feature extraction for each group are described as follows. In the process of feature extraction, each collagen pattern was classified into aggregated and distributed collagen. If a collagen fiber links to other fibers, it has more than one cross-link and is classified as aggregated collagen. Distributed collagens are those collagen fibers with no cross-links with others.

34 portal collagen features are shown in **Table 3**. Portal collagen is divided into two groups, aggregated and distributed collagen, based on their cross-linking properties. Aggregated collagen is cross-linked while the distributed collagen is not. Some of the collagen features were extracted from aggregated and distributed collagen separately. The major axis of each collagen fiber is tracked and the features such as fiber number, length, width, curvature, alignment, cross-link space and cross-link density are calculated as described in [114]. The caliber of the portal tract or central vein is measured as the cut-off threshold for differentiating portal and septal collagen patterns.

Table 3: Description of 34 portal collagen features. The 19 features selected after feature selection procedure are highlighted in grey.

Number	Feature	Description
1	CPA	Portal collagen proportionate area
2	Fiber Number	Portal collagen fiber number
3	Fiber Length	Portal collagen fiber length
4	Fiber Width	Portal collagen fiber width
5	Fiber Curvature	Portal collagen fiber curvature
6	Fiber Alignment	Portal collagen fiber alignment
7	Fiber CL Density	Portal collagen fiber cross-link density
8	Fiber CL Space	Portal collagen fiber cross-link space
9	Agg CPA	Portal aggregated collagen proportionate area
10	Agg Fiber Number	Portal aggregated collagen fiber number
11	Agg Fiber Length	Portal aggregated collagen fiber length
12	Agg Fiber Width	Portal aggregated collagen fiber width
13	Agg Fiber Curvature	Portal aggregated collagen fiber curvature
14	Agg Fiber Alignment	Portal aggregated collagen fiber alignment
15	Agg Fiber CL Density	Portal aggregated collagen fiber cross-link density
16	Agg Fiber CL Space	Portal aggregated collagen fiber cross-link space
17	Dis CPA	Portal distributed collagen proportionate area

18	Dis Fiber Number	Portal distributed collagen fiber number
19	Dis Fiber Length	Portal distributed collagen fiber length
20	Dis Fiber Width	Portal distributed collagen fiber width
21	Dis Fiber Curvature	Portal distributed collagen fiber curvature
22	Dis Fiber Alignment	Portal distributed collagen fiber alignment
23	Cut-off Width	Portal tract / central vein collagen thickness
24	CPA/ROI	Portal collagen proportionate area per ROI
25	Fiber Number/ROI	Portal collagen fiber number per ROI
26	Agg CPA/ROI	Portal aggregated collagen proportionate area per ROI
27	Agg Fiber Number/ROI	Portal aggregated collagen fiber number per ROI
28	Dis CPA/ROI	Portal distributed collagen proportionate area per ROI
29	Dis Fiber Number/ROI	Portal distributed collagen fiber number per ROI
30	Agg CPA/CPA	Ratio between portal aggregated collagen proportionate area and portal collagen proportionate area
31	Dis CPA/CPA	Ratio between portal distributed collagen proportionate area and portal collagen proportionate area
32	Agg CPA/CPA/ROI	Ratio between portal aggregated collagen proportionate area and portal collagen proportionate area per ROI
33	Dis CPA/CPA/ROI	Ratio between portal distributed collagen proportionate area and portal collagen proportionate area per ROI
34	CPA/Total CPA	Ratio between portal collagen proportionate area and total collagen proportionate area

28 septal collagen features are shown in **Table 4**. A similar approach is adopted to separate this collagen into aggregated and distributed collagen. The number of septa was recognized as the number of local maxima found in angle profile during the process of septal collagen identification. The width of each local maximum in the angle profile represents the width of each septum, and the collagen percentage along the local maxima represents the completeness of certain septa.

Table 4: Description of 28 septal collagen features. The 13 features selected after feature selection procedure are highlighted in grey.

Number	Feature	Description
1	CPA	Septal collagen proportionate area
2	Fiber Number	Septal collagen fiber number
3	Fiber Length	Septal collagen fiber length
4	Fiber Width	Septal collagen fiber width
5	Fiber Curvature	Septal collagen fiber curvature
6	Fiber Alignment	Septal collagen fiber alignment
7	Fiber CL Density	Septal collagen fiber cross-link density
8	Fiber CL Space	Septal collagen fiber cross-link space

Number	Feature	Description
9	Agg CPA	Septal aggregated collagen proportionate area
10	Agg Fiber Number	Septal aggregated collagen fiber number
11	Agg Fiber Length	Septal aggregated collagen fiber length
12	Agg Fiber Width	Septal aggregated collagen fiber width
13	Agg Fiber Curvature	Septal aggregated collagen fiber curvature
14	Agg Fiber Alignment	Septal aggregated collagen fiber alignment
15	Agg Fiber CL Density	Septal aggregated collagen fiber cross-link density
16	Agg Fiber CL Space	Septal aggregated collagen fiber cross-link space
17	Dis CPA	Septal distributed collagen proportionate area
18	Dis Fiber Number	Septal distributed collagen fiber number
19	Dis Fiber Length	Septal distributed collagen fiber length
20	Dis Fiber Width	Septal distributed collagen fiber width
21	Dis Fiber Curvature	Septal distributed collagen fiber curvature
22	Dis Fiber Alignment	Septal distributed collagen fiber alignment
23	Agg CPA/Septal CPA	Ratio between septal aggregated collagen proportionate area and septal collagen proportionate area
24	Dis CPA/Septal CPA	Ratio between septal distributed collagen proportionate area and septal collagen proportionate area
25	CPA/Total CPA	Ratio between septal collagen proportionate area and total collagen proportionate area
26	Number of Septa/ROI	Number of septa per ROI
27	Septa Width	Average septa width
28	Septa Completeness	Average septa completeness between ROIs

25 fibrillar collagen features are shown in **Table 5**. Morphological features are extracted from total fibrillar collagen, aggregated fibrillar collagen and distributed fibrillar collagen separately.

Table 5: Description of 25 fibrillar collagen features. The 8 features selected after feature selection procedure are highlighted in grey.

Number	Feature	Description
1	CPA	Fibrillar collagen proportionate area
2	Fiber Number	Fibrillar collagen fiber number
3	Fiber Length	Fibrillar collagen fiber length
4	Fiber Width	Fibrillar collagen fiber width
5	Fiber Curvature	Fibrillar collagen fiber curvature

6	Fiber Alignment	Fibrillar collagen fiber alignment
7	Fiber CL Density	Fibrillar collagen fiber cross-link density
8	Fiber CL Space	Fibrillar collagen fiber cross-link space
9	Agg CPA	Fibrillar aggregated collagen proportionate area
10	Agg Fiber Number	Fibrillar aggregated collagen fiber number
11	Agg Fiber Length	Fibrillar aggregated collagen fiber length
12	Agg Fiber Width	Fibrillar aggregated collagen fiber width
13	Agg Fiber Curvature	Fibrillar aggregated collagen fiber curvature
14	Agg Fiber Alignment	Fibrillar aggregated collagen fiber alignment
15	Agg Fiber CL Density	Fibrillar aggregated collagen fiber cross-link density
16	Agg Fiber CL Space	Fibrillar aggregated collagen fiber cross-link space
17	Dis CPA	Fibrillar distributed collagen proportionate area
18	Dis Fiber Number	Fibrillar distributed collagen fiber number
19	Dis Fiber Length	Fibrillar distributed collagen fiber length
20	Dis Fiber Width	Fibrillar distributed collagen fiber width
21	Dis Fiber Curvature	Fibrillar distributed collagen fiber curvature
22	Dis Fiber Alignment	Fibrillar distributed collagen fiber alignment
23	Agg CPA/Fibrillar CPA	Ratio between fibrillar aggregated collagen proportionate area and fibrillar collagen proportionate area
24	Dis CPA/Fibrillar CPA	Ratio between fibrillar distributed collagen proportionate area and fibrillar collagen proportionate area
25	CPA/Total CPA	Ratio between fibrillar collagen proportionate area and total collagen proportionate area

3.2.4.3 Combination of features into indices

To demonstrate how features were extracted and combined into indices, we used the portal index from the TAA animal model as an example. From the 34 portal collagen features (**Table 3**), 19 features were selected based on their relevance to fibrosis progression (**Figure 11A**), highlighted in grey in **Table 3**, using a class-specific ensemble feature selection framework that is explained in the following section. By using principal component analysis, we generated the two most significant principal components (PC) from the 19 features. These two PCs together contained more than 75% of the variance and each represented more than 10% of the total variance of the 19 selected features (**Figure 11B**). The values of the two PCs at different stages of

63

fibrosis are shown in **Figure 11C, 11D**. The first PC indicated an increasing trend along fibrosis progression and reflected the changes of the majority of selected features. The second PC was only sensitive to the difference between stages 1 and 2 where the distributed portal collagen percentage and distributed portal collagen number played the most important roles. Finally, we trained a multinomial logistic regression model [150] based on these two PCs to estimate the probability of each stage for a certain sample and normalized the probabilities into the portal index (**Figure 14A**).
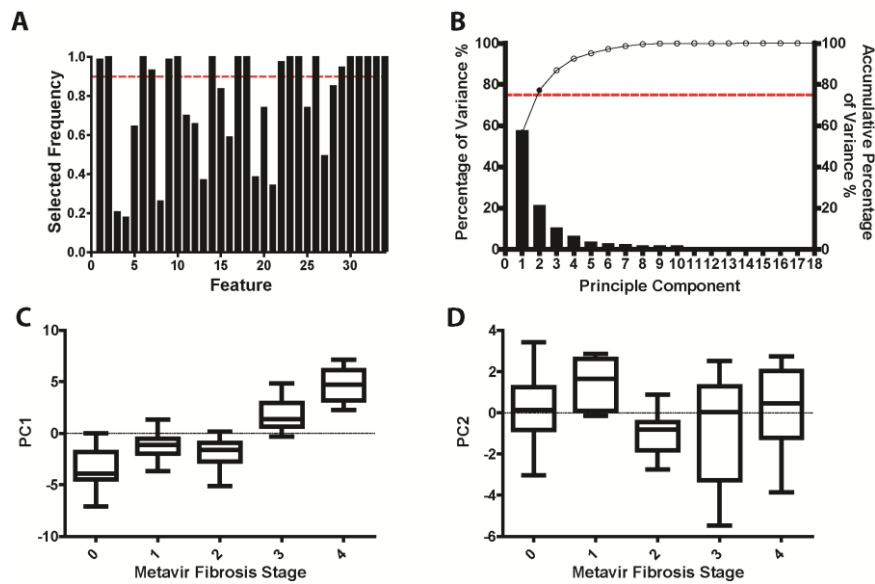
Figure 11: Statistical analysis to reduce the dimension of portal collagen features in Thioacetamide (TAA)-induced animal model. (A) 19 features were selected from 34 portal collagen features. (B) The 19 selected features were reduced to two principal components by principal component analysis. (C-D) The box-plots of the two principal components used show different trends along the Metavir stages of fibrosis progression.

Similar approaches were applied to septal collagen features (**Table 4, Figure 12**) and fibrillar collagen features (**Table 5, Figure 13**) to build the septal index (**Figure 14B**) and the fibrillar index (**Figure 14C**), respectively. All the PCs from portal, septal and fibrillar collagen were used together to create *q*Fibrosis.
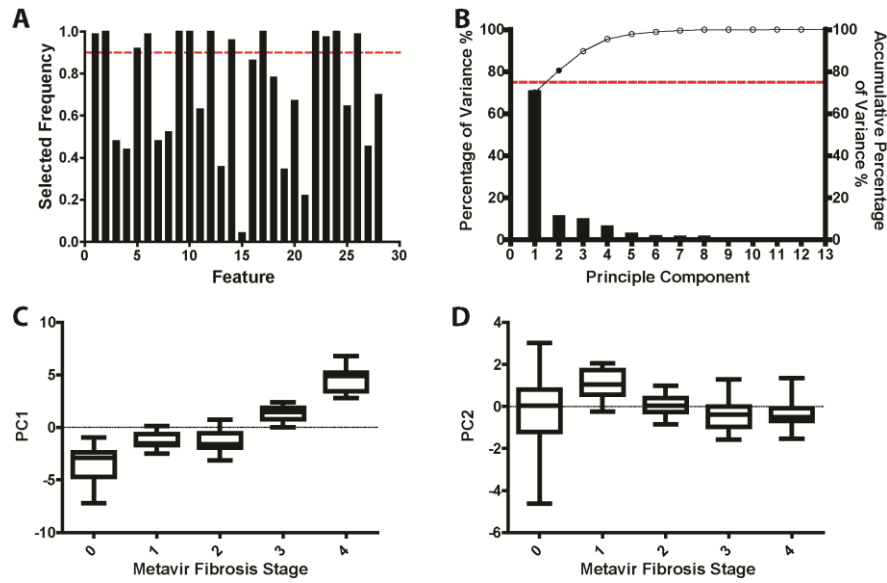
Figure 12: Statistical analysis to reduce the dimension of septal collagen features in Thioacetamide (TAA)-induced animal model. (A) 13 features were selected from 28 septal collagen features. (B) The 13 selected features were reduced to two principal components by principal component analysis. (C-D) The box-plots of the two principal components used show different trends along the Metavir stages of fibrosis progression.
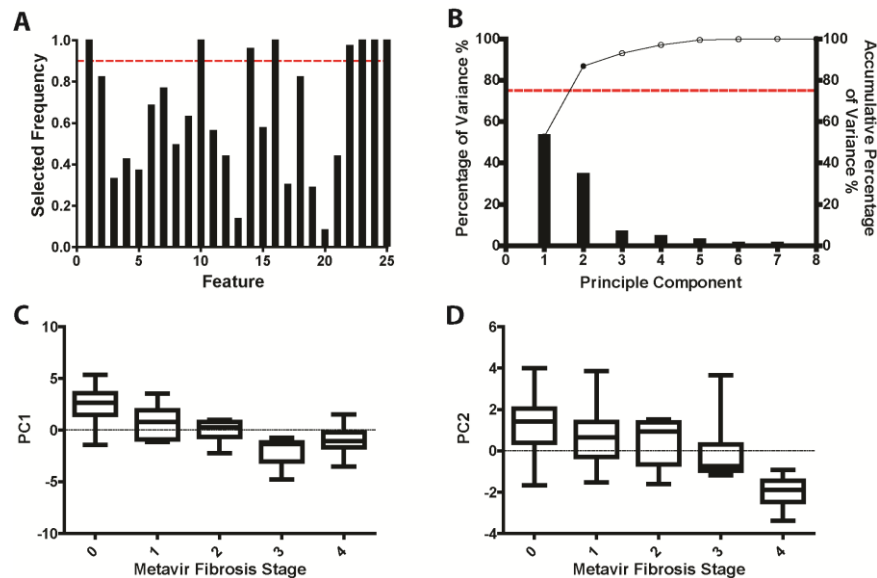
Figure 13: Statistical analysis to reduce the dimension of fibrillar collagen features in Thioacetamide (TAA)-induced animal model. (A) 8 features were selected from 25 fibrillar features. (B) The 8 selected features were reduced to two principal components by principal component analysis. (C-D) The box-plots of the two principal components used show different trends along the Metavir stages of fibrosis progression.
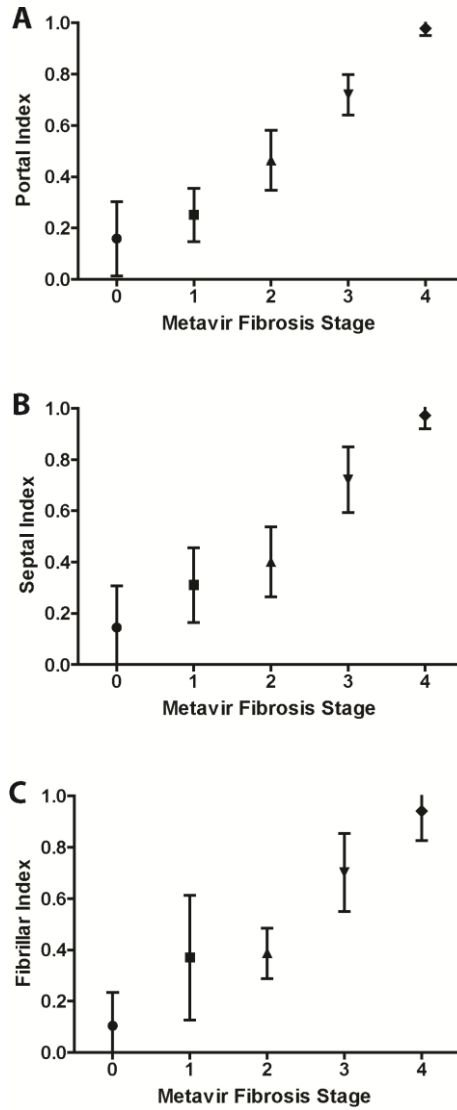
Figure 14: Portal, septal and fibrillar indices. (A) The most drastic increase in the portal index occurs from stage 1 to 2, when portal expansion is the dominant site of collagen deposition. (B) The septal index, on the other hand, increases most significantly from stage 2 to 3 when collagenous connections bridge adjacent portal tracts. (C) The change of fibrillar index.

3.2.4.4 Class-specific ensemble feature selection

To identify the most important features from all the features extracted, we designed a class-specific ensemble feature selection framework. One hundred bootstrap samples were created to generate diversities in training samples. For each bootstrap sample, the features were ranked using support vector machine recursive feature elimination

(SVM-RFE) method [151]. An ensemble rank of each feature was generated using the same approach in Abeel et al [152]. The best overall feature subset was selected according to the classification performance tested on the out-of-bag samples. The frequency of each feature to be selected from all 100 bootstrap samples was used as the criteria to evaluate its importance. The important features tend to be selected in most of the bootstrap samples no matter how the training set was altered. The cutoff frequency was set to 90% as those features which were selected at least 90 times from 100 bootstrap samples were recognized as important features for further analysis.

3.2.4.5 Principal component analysis

Principal component analysis [153] was used to convert the selected important features into a set of linearly uncorrelated principal components (PC). Each PC was a weighted summation of all the selected features with different weights. The first PC has the largest possible variance while each succeeding component has descending possible variances. We selected the PC with two criteria: the sum variance of all selected PC should exceed 75% of the total variance of the important features and each PC should have a variance with no less than 10% of the total variance. By doing this selection, we can better assess the fibrosis with those trends observed in these morphological features during fibrosis progression.

3.2.4.6 Multinomial logistic regression

To combine all PC to qFibrosis and its subindices, we used multinomial logistic regression (MNL) [154], a generalization of normal logistic regression which can create five or seven discrete outcomes (for Metavir and Ishak scores). To calculate the index (portal, septal, fibrillar and qFibrosis) for a testing sample, a training set of images was defined. The probability of the sample belonging to each stage from 0 to 4

was predicted from the trained MNL model. The index was calculated by the following equation:

$$qFibrosis = \alpha \sum pi * Ei, i = 0, 1, 2, 3, 4,$$

where p_i was the probability of stage i, $Ei = i$ was the expectation value of each stage and α was a scale factor to normalize the index into certain range. α was set to 1/4 in our study so that the index was a continuous variant located in the range from 0 to 1.

In the animal study, to calculate the index (portal, septal, fibrillar and qFibrosis) for each sample, the leave-one-out training is performed as all the other samples were used as the training set.

In the human experiment to investigate the performance of qFibrosis to replicate the fibrosis scores obtained with Metavir scores, the leave-one-out training is used to calculate the index for each sample, either using all the samples or using the long biopsy samples.

In the human experiment to study the performance of correction of sampling error-mediated intra-observer variation, the 69 good quality biopsy samples were used as the training set to test the remaining suboptimal biopsy samples.

In the human experiment to explore the performance of correction of inter-observer variation, the leave-one-out training is used to calculate the index for each sample using the scores from the experienced pathologist as the references.

In the human experiment to validate qFibrosis on another independent cohort, the original 107 biopsy samples were used as the training set to test another 55 biopsy samples in a new cohort.

3.2.5 Statistical analysis

The two-tailed Wilcoxon rank-sum test was performed to estimate the statistical differences of CPA and qFibrosis index between different Metavir and Ishak fibrosis stages, and differences of clinical measurements between Ishak stages 5 and 6. The DeLong test was used to compare the receiver-operating-characteristics curves (ROCs) and area under ROCs (AUCs) of qFibrosis and CPA. The stepwise logistic regression was performed to find the best combination of markers to differentiate Ishak stages 5 and 6. Statistical significance level was set as $p < 0.05$.

3.3 Results

3.3.1 qFibrosis, and automated assessment of changes in collagen patterns and quantification of liver fibrosis

qFibrosis was developed based on key architectural features, namely, portal expansion (portal collagen), fibrosis bridging mechanism (septal collagen), and general distribution of fine collagen in the pericellular/perisinusoidal space of Disse throughout the liver (fibrillar collagen) (**Figure 15A**). Using the Metavir staging system as an example, normal livers (F0) contain minimal collagenous tissue (blue) within portal tracts and around central veins. In early stage of fibrosis (F1), there is fibrous portal expansion (blue). In the next stage (F2), incomplete spike-like septa (green) emanate from some of the portal tracts. With progression of fibrosis (F3), some complete septa (green) begin to link some of the portal tracts and occasionally bridge portal tracts and central veins. The last stage, cirrhosis (F4), is established when broad complete septa (green) are formed between portal areas, and between portal areas and central veins, intersecting the lobular architecture and surrounding regenerative hepatocellular nodules [90]. qFibrosis is able to identify and differentiate

69

the collagen patterns at different stages of liver fibrosis (**Figure 15B**). In the statistical analysis framework of *q*Fibrosis (**Figure 15C**), a list of 87 collagen architectural features (Table 3, 4 and 5) was categorized into three groups: portal, septal and fibrillar collagen. The feature selection [151] was performed to identify the most important architectural features. We used principal component analysis [153] to reduce the dimension of the selected features and multinomial logistic regression to combine the principal components into a single index - *q*Fibrosis. The potential use of *q*Fibrosis in routine clinical practice is illustrated in **Figure 16**.
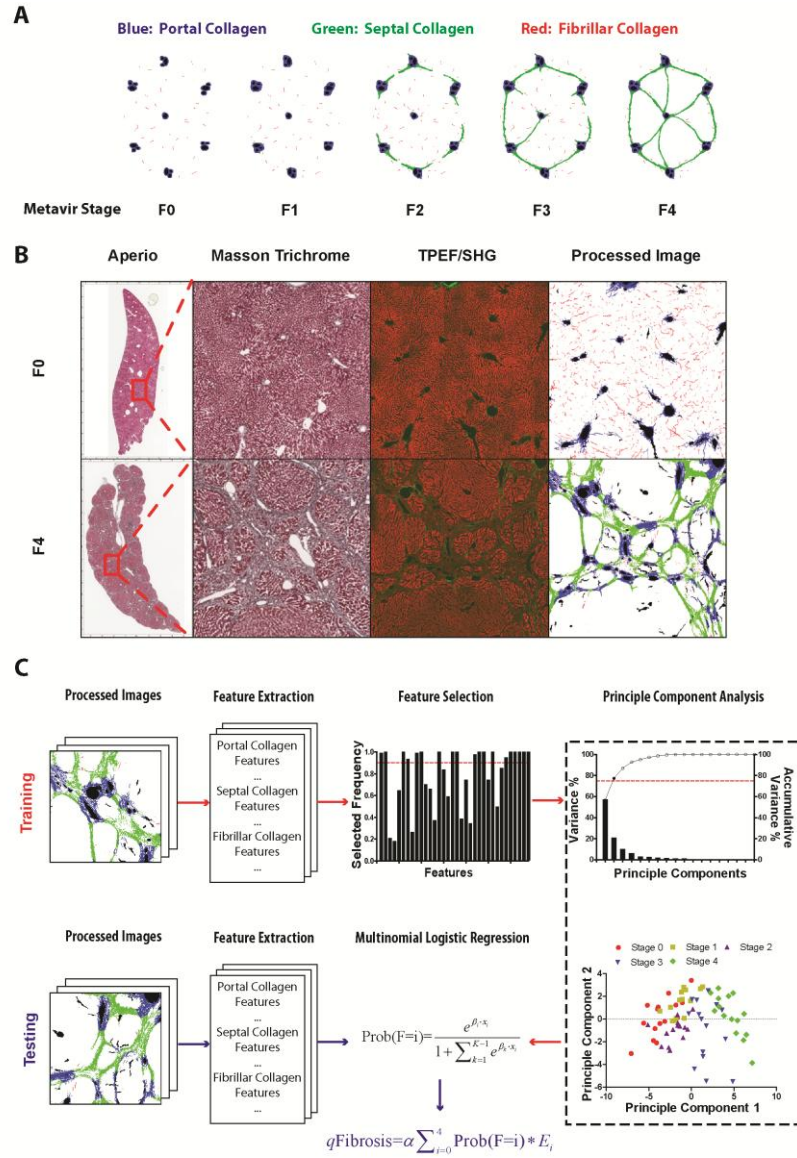
Figure 15: Schematic illustration of *q*Fibrosis establishment. (A) Representation of changes in collagen patterns in chronic liver disease based on Metavir staging system. Portal, septal and fibrillar collagen are denoted in blue, green and red, respectively. (B) The 3 types of collagen patterns are shown in Thioacetamide (TAA)-induced rat liver samples with normal and advanced fibrosis, as visualised by Masson Trichrome-stained, TPEF/SHG and processed images. (C) Computation framework to establish *q*Fibrosis.
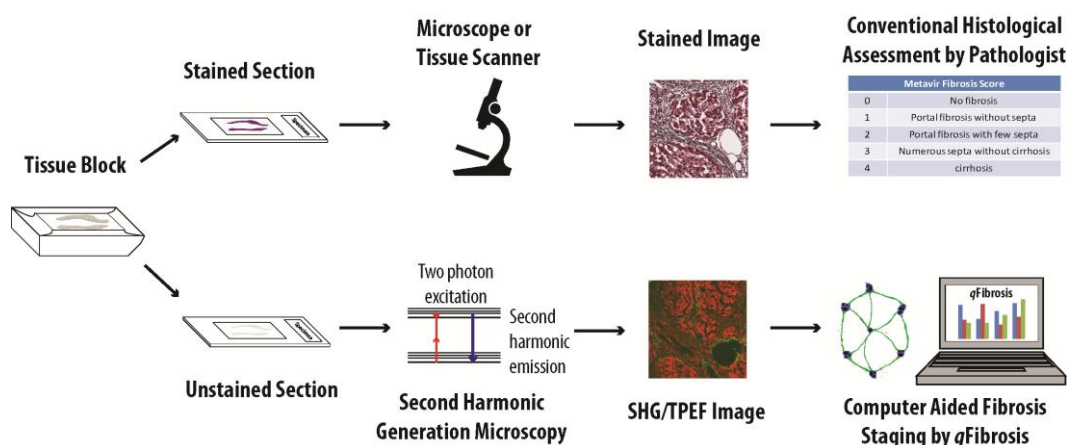
Figure 16: Illustration of qFibrosis application in liver biopsy-based fibrosis assessment. Conventional histological assessment of liver fibrosis requires human observation of microscopic images from stained tissue sections. *q*Fibrosis provides fully-automated, computer-aided liver fibrosis staging, which is fast, quantitative and consistent.

3.3.2 *q*Fibrosis scoring faithfully replicate Metavir fibrosis staging

We first investigated the performance of *q*Fibrosis to replicate the fibrosis scores obtained with conventional histological assessment such as Metavir staging system. *q*Fibrosis reflected a continuum of fibrosis progression that was consistent with Metavir fibrosis stages in both animal model and CHB patients, of which the values are summarized in **Tables 6** and **7**, respectively.

Table 6: *q*Fibrosis values of Thioacetamide-treated animal samples. (SEM: standard error of mean)

Fibrosis – Metavir Score	Fibrosis – *q*Fibrosis				
	25th percentile	75th percentile	Median	Mean	SEM
F0 (n= 15)	0.016	0.144	0.049	0.074	0.017
F1 (n= 15)	0.157	0.410	0.258	0.266	0.040
F2 (n= 15)	0.350	0.504	0.429	0.434	0.031
F3 (n= 15)	0.743	0.854	0.751	0.779	0.025
F4 (n= 15)	0.968	1.000	0.998	0.956	0.021

72

Table 7: *q*Fibrosis values in 69 chronic hepatitis B core liver biopsies longer than 15 mm. (SEM: standard error of mean)

Fibrosis – Metavir score	Fibrosis – *q*Fibrosis				
	25th percentile	75th percentile	Median	Mean	SEM
F1 (n= 12)	0.257	0.493	0.374	0.411	0.051
F2 (n= 9)	0.445	0.783	0.590	0.607	0.073
F3 (n= 18)	0.640	0.919	0.809	0.761	0.047
F4 (n= 30)	0.776	0.995	0.933	0.892	0.023

In the rat model, 75 liver tissue images (16 mm^2) were quantified with 15 images from each stage. *q*Fibrosis values increased with fibrosis progression and showed significant differences between all the stages ($p < 0.001$) (**Figure 17A**). CPA showed drastic changes only in late stages and could not differentiate between early stages (stages 1 and 2) (**Figure 17B**). In the CHB biopsies, *q*Fibrosis values, obtained from 69 biopsies longer than 15 mm, successfully differentiated between all stages ($p < 0.05$) (**Figure 17C**). In comparison, CPA could only differentiate between stages 3 and 4 (stages 1 versus 2, $p = 0.124$; stages 2 versus 3, $p = 0.194$) (**Figure 17D**).
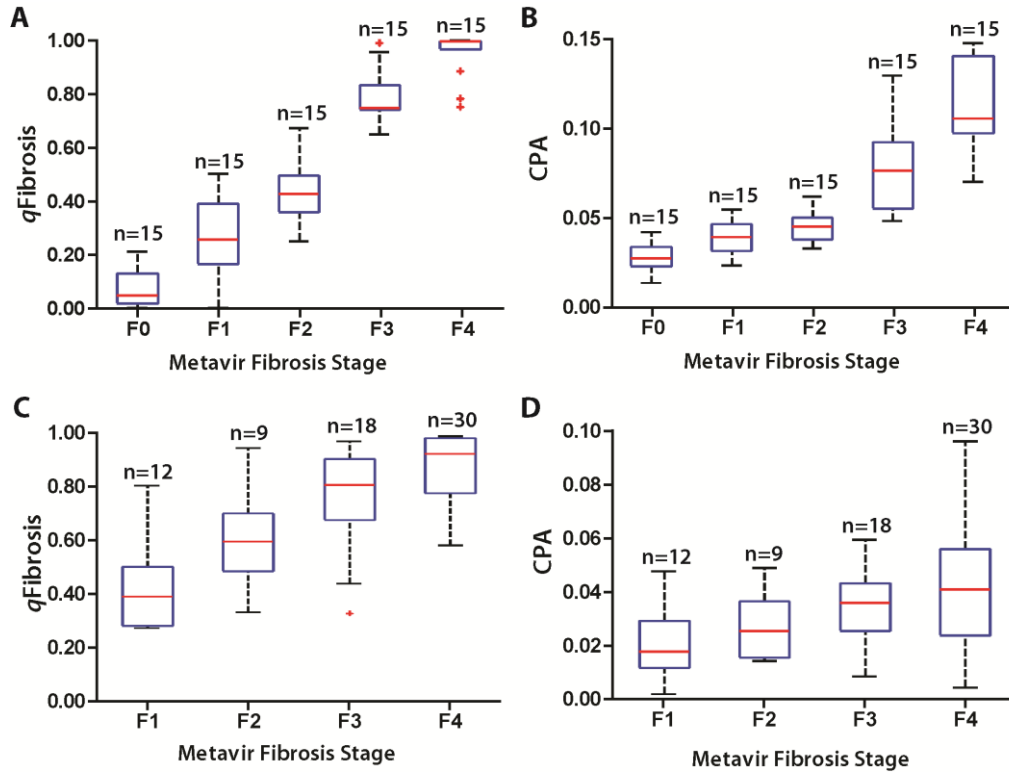
Figure 17: *q*Fibrosis faithfully matches Metavir fibrosis staging. (A) Changes of *q*Fibrosis with fibrosis progression between the various stages in Thioacetamide (TAA)-treated animals ($p < 0.001$). (B) Changes of collagen proportionate area (CPA) with fibrosis progression in TAA-treated animals. (C) Changes of *q*Fibrosis with fibrosis progression between the various stages in core biopsy samples from chronic hepatitis B patients ($p < 0.05$). (D) Changes of CPA with fibrosis progression in the same core biopsies. The boxes indicate the median, 25th and 75th percentiles, whereas vertical bars display the adjacent value and '+' symbols represent outliers.

3.3.3 *q*Fibrosis is less sensitive to sampling error

Sampling error is a major limitation when applying quantification methods such as CPA [20]. To assess the sensitivity of *q*Fibrosis to sampling error, we first performed a proof-of-concept demonstration with animal samples. Different sizes were divided from a large-size section of liver containing sufficient number of portal tracts for accurate scoring by an experienced pathologist. Images of the large sections were cropped to simulate samples of varying sizes (**Figure 18**). The coefficient of variation (CV) of *q*Fibrosis was calculated for each sample at different sizes; the CV values

gradually increased from 18% to 28% whilst the sample sizes decreased from 8 mm^2 to 1 mm^2 (**Figure 19**). In contrast, the CV of CPA increased more drastically from 20% to 46% for the same sample size (**Figure 19**). The CV of qFibrosis was significantly smaller than that of CPA for samples sizes at 4 mm^2 ($p = 0.02$), 2 mm^2 ($p < 0.001$) and 1 mm^2 ($p < 0.001$).
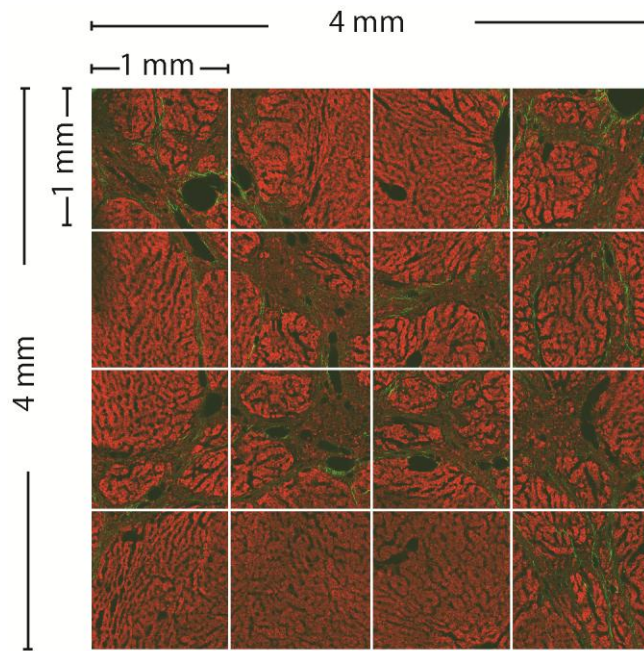
Figure 18: The image of each sample was cropped into half, one-fourth, one-eighth and one-sixteenth of the original size. Coefficient of variance (CV) of qFibrosis and collagen proportionate area (CPA) was calculated.
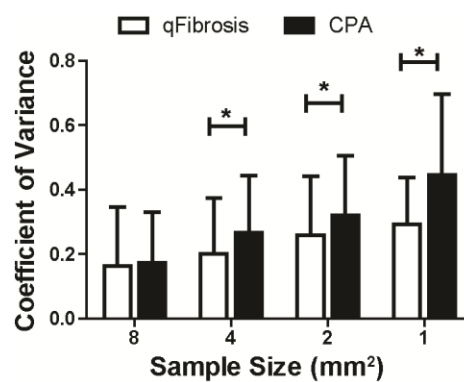
Figure 19: Coefficient of variance of qFibrosis and CPA in animal samples (*: $p < 0.05$).

The performances of *q*Fibrosis versus CPA for fibrosis scoring with different sample sizes were evaluated with ROC analysis (**Figure 20, Table 8**). The AUC values of *q*Fibrosis decreased slightly along with the reduction in sample sizes (**Figure 20A**). CPA achieved similar AUC values as *q*Fibrosis using large samples at 16 mm^2; however, the AUC values of CPA decreased drastically when the sample sizes were reduced (**Figure 20B**). The differences of AUC between *q*Fibrosis and CPA values became significant at half (8 mm^2) (stages 0 versus 1, 2, 3, 4 and 0, 1 versus 2, 3, 4; *p* < 0.05, respectively) to one fourth (4 mm^2) (all stages, *p* < 0.001) of the original size for differentiating liver fibrosis stages. The performance achieved by *q*Fibrosis at 1 mm^2 sample size (AUC: 0.95 - 0.93) was similar to that obtained by CPA at sample size of 8 mm^2 (AUC: 0.96 - 0.90).
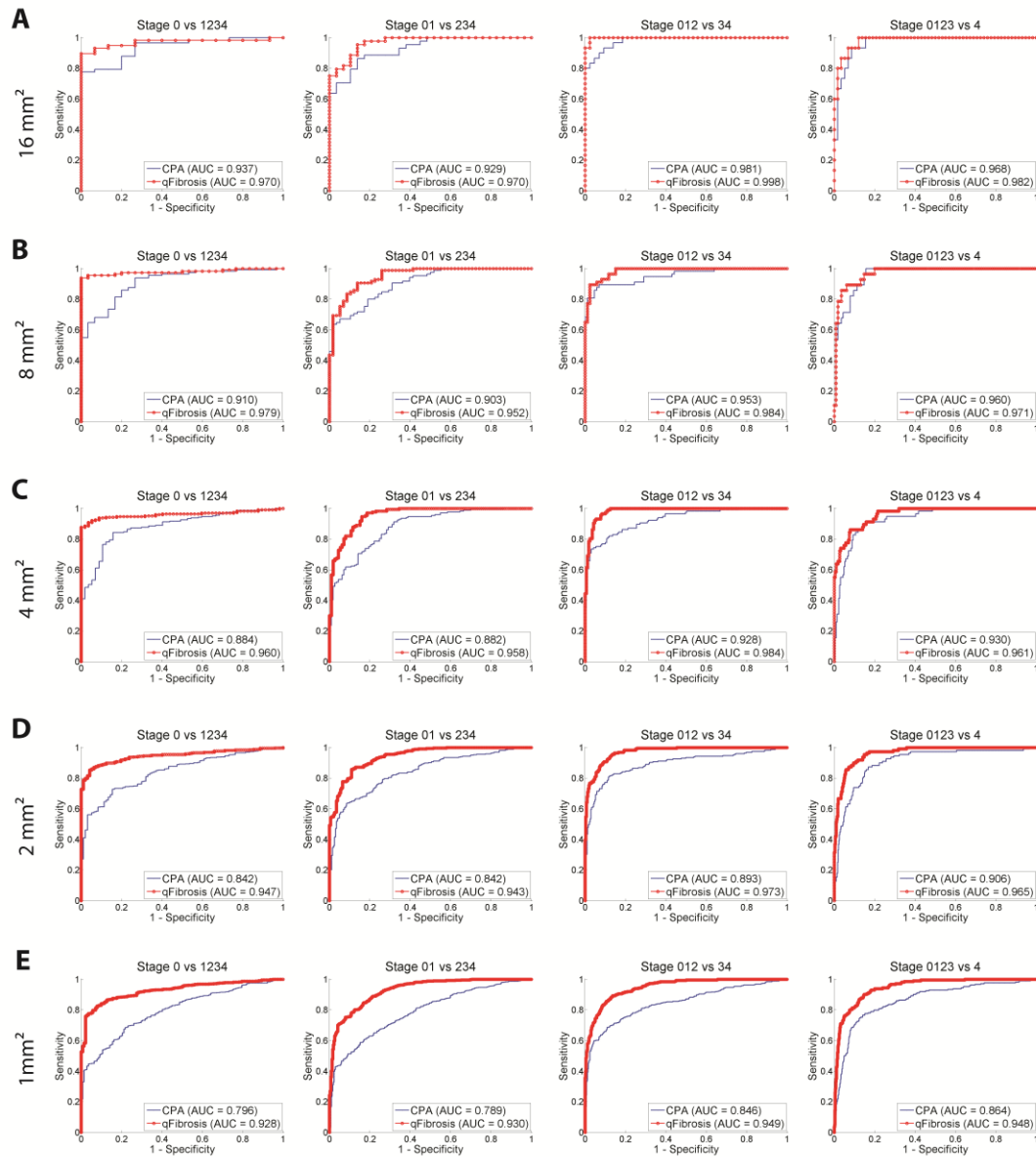
Figure 20: Performance of *q*Fibrosis and collagen proportionate area (CPA) to differentiate fibrosis stages on rat samples of different size. For the detection of any stage in the fibrosis progression, the AUCs of *q*Fibrosis were higher than those of CPA at all sample sizes (A-E). For the detection of fibrosis (stage 0 versus stages 1-4) and significant fibrosis (stages 0-1 versus stages 2-4), the improved performances of *q*Fibrosis over CPA were significant at all sample sizes except for the largest sample size tested (16 mm^2) (A). For differentiating stages 1-2 and stages 3-4, as well as non-cirrhosis and cirrhosis (stages 0-3 versus stage 4), the AUCs of *q*Fibrosis remained above 0.95 in smaller sample sizes (4 mm^2 to 1 mm^2) (C-E) while the AUC of CPA decreased to 0.85 (1 mm^2) (E). The improved performances of *q*Fibrosis were significant in these sample sizes (4 mm^2 to 1 mm^2) (C-E). The standard error and 95% confidence interval of all ROC curves are shown in **Table 8**.

Table 8: Statistics of ROC analysis of *q*Fibrosis and collagen proportionate area (CPA) on animal samples of different sizes. (AUC: area under the ROC curve, SE: standard error, CI: confidence interval)

Fibrosis Stage	Sample Size									
	16 mm^2		8 mm^2		4 mm^2		2 mm^2		1 mm^2	
	AUC (SE)	95% CI	AUC (SE)	95% CI	AUC (SE)	95% CI	AUC (SE)	95% CI	AUC (SE)	95% CI
*q*Fibrosis										
0 vs. 1234	0.970 (0.019)	[0.901, 0.996]	0.979 (0.011)	[0.940, 0.996]	0.960 (0.011)	[0.931, 0.980]	0.947 (0.009)	[0.925, 0.964]	0.928 (0.009)	[0.910, 0.944]
01 vs. 234	0.970 (0.016)	[0.901, 0.996]	0.952 (0.017)	[0.903, 0.981]	0.958 (0.011)	[0.928, 0.978]	0.943 (0.009)	[0.903, 0.981]	0.930 (0.008)	[0.912, 0.945]
012 vs. 34	0.998 (0.002)	[0.948, 1.000]	0.984 (0.007)	[0.947, 0.998]	0.984 (0.005)	[0.962, 0.995]	0.973 (0.005)	[0.955, 0.985]	0.949 (0.006)	[0.933, 0.962]
0123 vs. 4	0.982 (0.012)	[0.918, 0.999]	0.971 (0.013)	[0.929, 0.992]	0.961 (0.011)	[0.932, 0.980]	0.965 (0.007)	[0.946, 0.979]	0.948 (0.007)	[0.932, 0.961]
CPA										
0 vs. 1234	0.937 (0.028)	[0.854, 0.980]	0.910 (0.027)	[0.851, 0.951]	0.884 (0.022)	[0.841, 0.919]	0.842 (0.019)	[0.808, 0.871]	0.796 (0.017)	[0.769, 0.821]
01 vs. 234	0.929 (0.027)	[0.845, 0.976]	0.903 (0.024)	[0.842, 0.946]	0.882 (0.020)	[0.839, 0.917]	0.842 (0.017)	[0.809, 0.872]	0.789 (0.015)	[0.762, 0.814]
012 vs. 34	0.981 (0.011)	[0.918, 0.999]	0.953 (0.018)	[0.904, 0.981]	0.928 (0.015)	[0.891, 0.955]	0.893 (0.015)	[0.864, 0.918]	0.846 (0.013)	[0.821, 0.868]
0123 vs. 4	0.968 (0.018)	[0.897, 0.995]	0.960 (0.015)	[0.913, 0.985]	0.930 (0.017)	[0.894, 0.957]	0.906 (0.016)	[0.878, 0.929]	0.864 (0.015)	[0.841, 0.885]
Significance of difference between *q*Fibrosis and CPA (P-value)										
0 vs. 1234	0.301		0.013		< .001		< .001		< .001	
01 vs. 234	0.060		0.009		< .001		< .001		< .001	
012 vs. 34	0.090		0.066		< .001		< .001		< .001	
0123 vs. 4	0.267		0.250		0.011		< .001		< .001	

In the clinical scenario provided by the CHB biopsies, the AUC values of *q*Fibrosis for the detection of different stages of fibrosis on 69 samples longer than 15 mm were from 0.92 to 0.84, while the AUC values of CPA were smaller (0.76 - 0.71) (**Figure 21A-C, Table 9**). We further evaluated *q*Fibrosis on all 107 non-fragmented human core biopsy samples that included both long ($\geq$ 15 mm) and short samples (< 15 mm), as short samples are unavoidable in routine clinical practice. AUC values of *q*Fibrosis were maintained at higher than 0.8 for detection of significant fibrosis and cirrhosis, whereas the AUC of CPA dropped to 0.71 (**Figure 21D-F, Table 9**). Thus, we demonstrated that *q*Fibrosis can potentially differentiate fibrosis at different stages in core biopsy samples of different sizes.
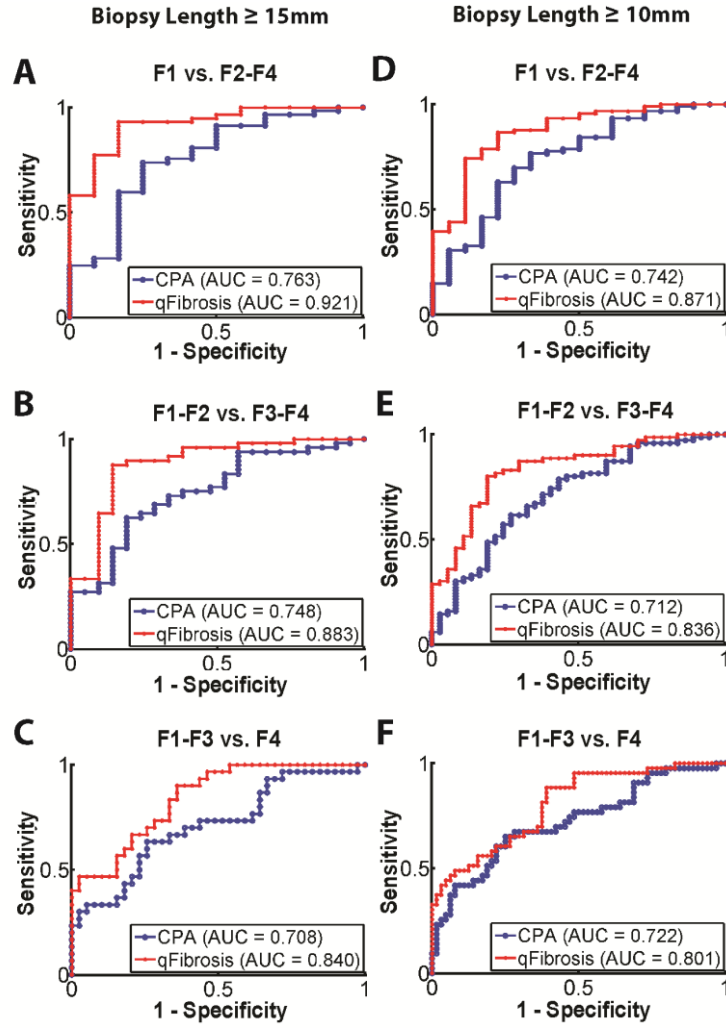
Figure 21: *q*Fibrosis is superior to collagen proportionate area (CPA) in resolving biopsy-related issues of sampling error. (A)-(C) Performances of *q*Fibrosis and CPA in differentiating all fibrosis stages for human core biopsies longer than 15 mm. (D)-(F) Performances of *q*Fibrosis and CPA in differentiating all fibrosis stages for human core biopsies, including short ones ($\geq$ 10 mm in length).

Table 9: Statistics of ROC analysis of *q*Fibrosis and collagen proportionate area (CPA) on human samples of different sizes. (AUC: area under the ROC curve, SE: standard error, CI: confidence interval)

Fibrosis Stage	Sample Length			
	≥15 mm		≥10 mm	
	AUC (SE)	95% CI	AUC (SE)	95% CI
*q*Fibrosis				
1 vs. 234	0.921 (0.041)	[0.831, 0.972]	0.871 (0.047)	[0.793, 0.928]
12 vs. 34	0.883 (0.048)	[0.783, 0.948]	0.836 (0.041)	[0.751, 0.900]
123 vs. 4	0.840 (0.046)	[0.732, 0.917]	0.805 (0.042)	[0.717, 0.875]
CPA				
1 vs. 234	0.763 (0.082)	[0.645, 0.857]	0.742 (0.067)	[0.649, 0.822]
12 vs. 34	0.748 (0.064)	[0.629, 0.845]	0.712 (0.054)	[0.616, 0.795]
123 vs. 4	0.709 (0.064)	[0.587, 0.812]	0.722 (0.051)	[0.627, 0.805]
Significance of difference between *q*Fibrosis and CPA (P-value)				
1 vs. 234	0.068		0.097	
12 vs. 34	0.049		0.014	
123 vs. 4	0.037		0.100	

3.3.4 *q*Fibrosis can aid in correction of sampling error-mediated intra-observer variation

Short core biopsy samples are known to yield underestimated scores in fibrosis staging [29]. We simulated the scenario of a pathologist scoring short core biopsy samples to investigate whether *q*Fibrosis can identify the potential underestimation. We used all 69 good quality (≥ 15 mm) biopsy samples to train a multinomial logistic regression model and applied it to the remaining 38 suboptimal (< 15 mm) biopsy samples to obtain *q*Fibrosis values. The underestimation of fibrosis stages by pathologists on suboptimal biopsy samples was accurately predicted by *q*Fibrosis (**Figure 22A**). CPA cannot predict the underestimation in all stages except for stage 4 (**Figure 22B**). It is generally accepted that there is rare underestimation of Metavir F4 samples. Therefore, *q*Fibrosis can potentially aid pathologists to adjust for the degree of aggressive versus conservative scoring decisions to compensate for sampling error-mediated intraobserver variation.
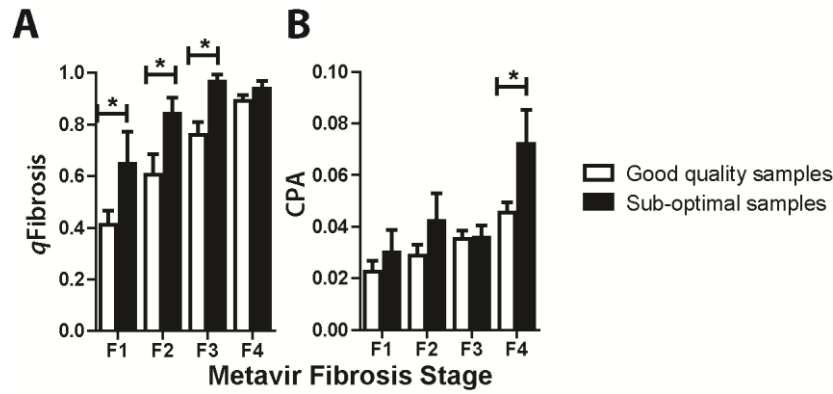
Figure 22: Comparison of the capability to highlight potential underscoring of suboptimal biopsy samples to address size-dependent sampling error-mediated intraobserver variation by qFibrosis (A) and CPA (B), respectively. The qFibrosis values of suboptimal biopsy samples scored as stages 1 to 3 are significantly higher than the qFibrosis values of good quality biopsy samples scored as the same stages, indicating that these suboptimal samples are underscored and may belong to later fibrosis stages (*: $p < 0.05$).

3.3.5 qFibrosis can aid in correction of inter-observer variation

We investigated whether qFibrosis can identify the trend of deviation of a pathologist's scoring with reference to an experienced pathologist's scores. All 107 human samples were independently scored by two pathologists, A and B. Cohen's and Fleiss's kappa statistics were used to assess the interobserver agreement between two (Cohen's) or any number (Fleiss's) of observers. The Cohen's kappa of the scores from the two pathologists was 0.40 ($p < 0.001$), suggesting a fair but not strong agreement (**Figure 23**).
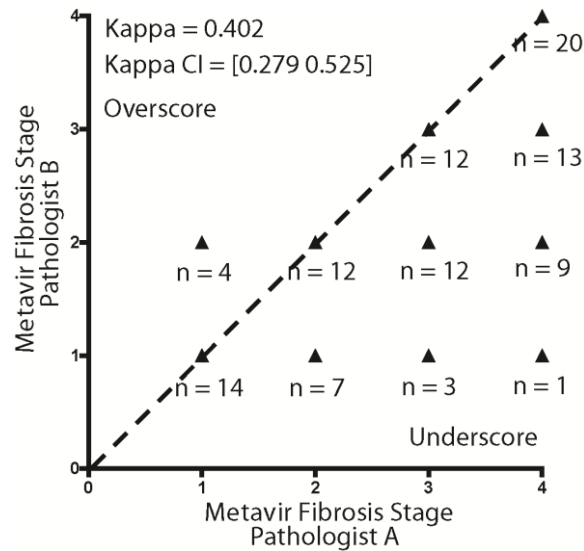
Figure 23: Deviation of fibrosis staging between one experienced pathologist and one non-expert pathologist in 107 human biopsy samples. Cohen's kappa score between 2 pathologists was 0.4.

Forty-nine out of 107 human samples with available FibroScan measurements were chosen to compare the consistency of fibrosis scores by the two pathologists. The cut-off values of non-invasive fibrosis markers, such as FibroScan, APRI, and FIB-4, to predict cirrhosis (F4) or significant fibrosis (F2-4) were established in large cohort studies of CHB patients [155-157]. The scores from pathologist A were more consistent with all the clinical markers (with higher Fleiss's kappa indicating stronger overall agreement) than pathologist B (**Table 10**). Thus, scores from pathologist A were used to train the multinomial logistic regression model to yield *q*Fibrosis values for all 107 samples.

Table 10: Thresholds of FibroScan, APRI and FIB-4 to predict cirrhosis (F 1, 2, 3 versus F 4) and significant fibrosis (F 1 versus F 2, 3, 4) are excerpted from literature. The Fleiss's kappa values indicate that the fibrosis scores from pathologist A are more consistent with FibroScan, APRI and FIB-4 results than the scores from pathologist B.

Pathologist	A	B
Prediction of Cirrhosis		
	Cohen's Kappa	
FibroScan > 12.5 kPa	0.50	0.45
APRI > 1	0.36	0.26
FIB-4 > 1.6	0.55	0.29
	Fleiss's Kappa	
Overall	0.50	0.43
Prediction of Significant Fibrosis		
	Cohen's Kappa	
FibroScan > 7.1 kPa	0.22	0.31
APRI > 0.5	0.31	0.31
FIB-4 > 1	0.22	0.34
	Fleiss's Kappa	
Overall	0.35	0.32

Compared to the scores from pathologist A, the scores from pathologist B were overestimated and underestimated by 3.7% and 42%, respectively. Such over- and underestimation can be accurately predicted by qFibrosis but not by CPA (**Figure 24**). Thus, qFibrosis can aid in the correction of interobserver variation in fibrosis assessment by serving as a reliable proxy for experienced pathologists.
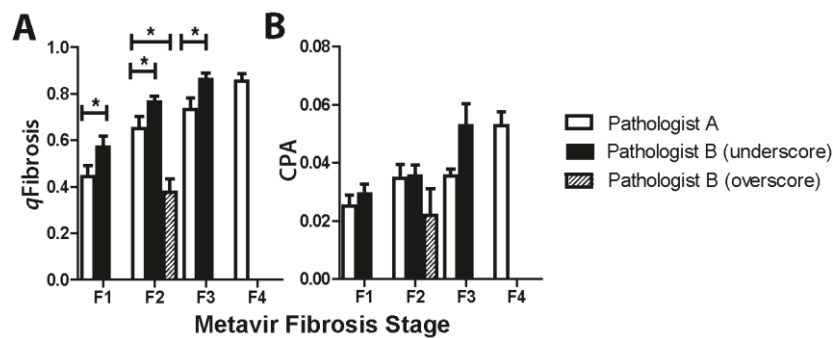
Figure 24: Comparison of the capability to predict interobserver over-/underestimation of biopsy samples by qFibrosis and CPA, respectively. The values of qFibrosis can significantly reflect the scoring-deviation under the same stages except for F4 (*: $p < 0.05$).

3.3.6 *q*Fibrosis can aid in detection and monitoring of intra-stage cirrhosis changes

To differentiate intra-stage cirrhosis changes, we calculated *q*Fibrosis values from 43 human samples that were categorized as cirrhosis (F4) on Metavir and under two substages 5 and 6 according to Ishak staging. *q*Fibrosis accurately differentiated these two substages ($p = 0.008$) with AUC of 0.73 whereas CPA failed to do so ($p = 0.302$) (**Figure 25A-C**). We also investigated whether the combination of *q*Fibrosis with non-invasive clinical markers would improve the detection of intra-stage cirrhosis. Nine routine clinical biomarkers and stiffness measurements by FibroScan were first assessed in 17 of the 43 Metavir F4 samples, which had complete clinical data; only FibroScan could differentiate intra-stage cirrhosis changes amongst these markers (**Table 11**). By stepwise logistic regression analysis, including all the 10 markers together with *q*Fibrosis and CPA, the combination of *q*Fibrosis, FibroScan and international normalized ratio (INR) was the most predictive for differentiating intra-stage cirrhosis (**Table 12**); the AUC improved from 0.81 (*q*Fibrosis only) to 0.93 (combination of *q*Fibrosis, FibroScan and INR) (**Figure 25D**). Thus, *q*Fibrosis can differentiate intra-stage cirrhosis changes alone or in combination with FibroScan and INR.
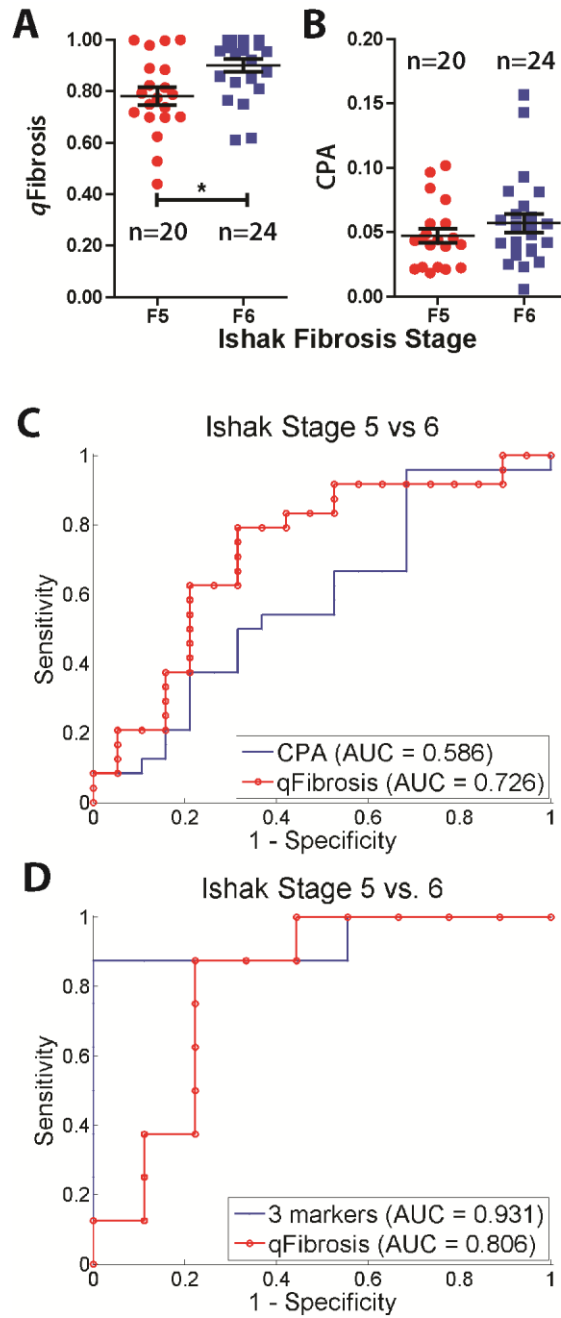
Figure 25: *q*Fibrosis is superior to collagen proportionate area (CPA) in intra-stage discrimination in cirrhosis. (A)-(B) Differentiation of Ishak stage 5 from 6 by *q*Fibrosis (*: $p = 0.008$) and CPA ($p = 0.302$). (C) ROC curve demonstrated the improved sensitivity and specificity of *q*Fibrosis to differentiate between Ishak staging scores of 5 and 6 than CPA in 44 human biopsy samples. (D) ROC curves of *q*Fibrosis and the combination of three markers (*q*Fibrosis, Fibroscan and INR) to detect intra-stage cirrhosis change on 17 cirrhotic biopsy samples with complete clinical measurement. The cut-off point for best sensitivity and specificity of *q*Fibrosis is 0.294 with 87.5% sensitivity and 77.8% specificity. The cut-off point for best sensitivity and specificity of the combination of 3 markers is 0.205 with 87.5% sensitivity and 100.0% specificity. The combination of clinical markers with *q*Fibrosis improves the detection of intra-stage cirrhosis changes.

85

Table 11: Comparison of *q*Fibrosis, collagen proportionate area (CPA) and clinical parameters for Ishak stages 5 and 6. Data are Mean ± SD. ALT: alanine transaminase, AST: aspartate transaminase, ALB: albumin, TBIL: total bilirubin, INR: international normalized ratio, PT: prothrombin time, APRI: AST-to-platelet ratio index, and FIB-4: FIB-4 index.

	Ishak Stage 5	Ishak Stage 6	*P* Value
CPA (%)	4.61 ± 2.30	7.22 ± 3.58	0.08
*q*Fibrosis (a.u.)	0.80 ± 0.16	0.94 ± 0.08	**0.03**
ALT (U/L)	149.33 ± 70.70	214.9 ± 236.9	0.44
AST (U/L)	110.33 ± 64.25	136.56 ± 82.84	0.46
ALB (g/L)	43.89 ± 4.61	43.01 ± 1.57	0.6
TBIL (mol/L)	23.51 ± 21.18	20.90 ± 5.64	0.73
INR (a.u.)	1.11 ± 0.09	1.11 ± 0.08	0.9
PT (s)	13.32 ± 1.14	13.28 ± 1.09	0.93
PLT (10^9/L)	199.67 ± 41.76	195.67 ± 30.63	0.82
FibroScan (kPa)	9.93 ± 3.37	17.13 ± 8.79	**0.04**
APRI (a.u.)	1.10 ± 0.85	1.22 ± 0.58	0.74
FIB-4 (a.u.)	2.09 ± 1.59	2.80 ± 2.08	0.43

Table 12: *q*Fibrosis, collagen proportionate area (CPA) and 10 clinical markers associated with intra-stage cirrhosis changes according to multiple logistic regression analysis. Stepwise forward analysis include 12 markers, namely, *q*Fibrosis, CPA, alanine transaminase, aspartate transaminase, albumin, total bilirubin, platelet count, prothrombin time and its international normalized ratio (INR), APRI, FIB-4 and FibroScan. Best model was found with three predictors (*q*Fibrosis, FibroScan and INR): r^2 = 0.80, χ^2 = 15.54, p = 0.0014 (intercept: regression coefficient, -6.40; p = 0.65). Using any additional marker will not improve the model.

Makers	Regression Coefficient	SE	Chi-square β	*P* value
*q*Fibrosis	17.61	11.17	2.49	0.11
FibroScan	0.84	0.55	2.33	0.13
INR	-17.52	13.04	1.80	0.18

3.3.7 Validation of *q*Fibrosis on another independent cohort of CHB biopsy samples

We further tested the reliability of *q*Fibrosis with the images of another 55 core biopsy samples acquired by a commercial SHG/TPEF imaging device. The values of *q*Fibrosis can faithfully replicate Metavir fibrosis scoring as the previous experiments indicated, of which the differentiation ability between stages is obviously better than CPA measurement (**Figure 26A-B**). The performances of both *q*Fibrosis and CPA are improved in this cohort due to the good sample quality (average length of 30.4 ± 4.4 mm), but *q*Fibrosis still performs better than CPA. The AUC values of *q*Fibrosis for detection of different stages were from 0.90 to 0.95, while the AUC values of CPA were smaller (0.84 - 0.92) (**Figure 26C-E**).
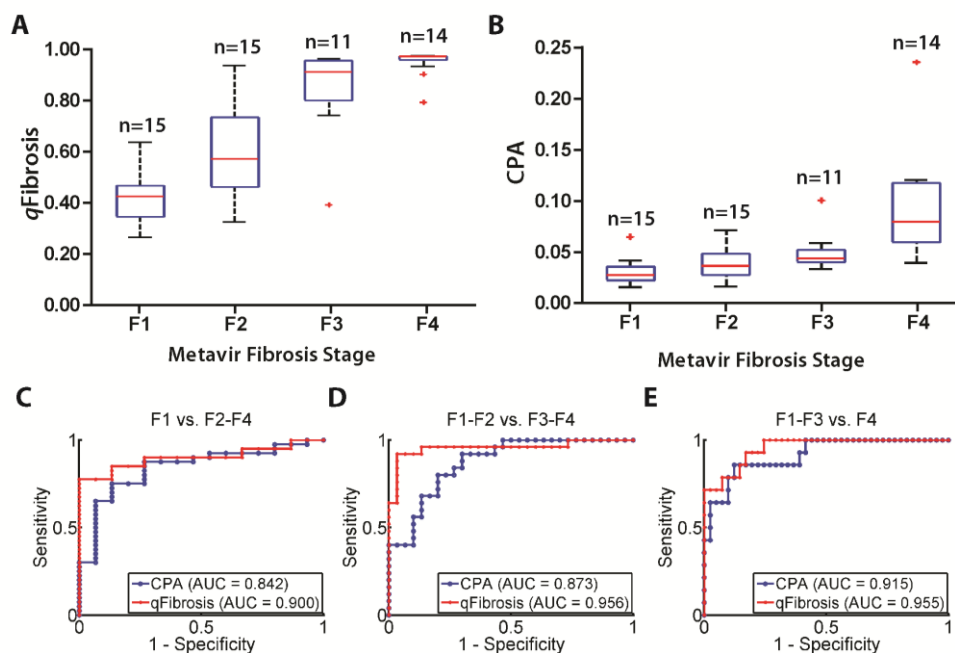
Figure 26: Validation of *q*Fibrosis in another independent cohort. (A) Changes of *q*Fibrosis with fibrosis progression between the various stages in 55 core biopsy samples from chronic hepatitis B patients. ($p < 0.001$). (B) Changes of collagen proportionate area (CPA) with fibrosis progression in the same core biopsies. The boxes indicate the median, 25th and 75th percentiles, whereas vertical bars display the

adjacent value and '+' symbols represent outliers. (C-E) Performances of *q*Fibrosis and CPA in differentiating all fibrosis stages for these 55 core biopsies.

3.4 Discussions

By incorporating spatial architectural features of pathological relevance at tissue level, we have established a fully-quantitative method - *q*Fibrosis - that can reliably recover liver fibrosis staging, but with reduced variability of sampling error and inter-/intraobserver bias in assessment of both animal samples and CHB core biopsies. In addition, *q*Fibrosis also showed the potential to discriminate fine changes within cirrhosis stage.

*q*Fibrosis establishment is based on two key elements. One is the suitable imaging techniques for efficient collection of tissue architectural information. For this purpose, we employed the nonlinear optical SHG/TPEF microscopy that was reported in Chapter 2. SHG/TPEF can quantify and localise collagen in 2D and 3D formats by its endogenous fluorescence in the stain-free samples [158], so as to accurately identify and discriminate the spatial parameters of the respective collagen patterns. Another is the qualified identification of histopathological architectural features. We used TAA-treated animal model to simulate the changes of CHB liver fibrosis [144], for serial sampling to sufficiently accumulate, select and test the parameters of image analysis; so that diversity and quality of tissue samples were guaranteed for appropriate pre-acquisition of architectural information for setting-up the *q*Fibrosis framework. All the considerations were justified by the better results of *q*Fibrosis performance testing in animal samples.

Histological staging is the fundamental concept for *q*Fibrosis design. In order to fully recapitulate the informative characteristics of traditional descriptive assessment, we designed the *q*Fibrosis index to encompass three key morphological phenotypes of

common pathological interest, and quantified them into three subindices by measuring the spatial parameters of fibrillar collagen within the individual phenotypic location. We observed that during the dynamics of fibrosis development, there were different trends of change between the three subindices (**Figures 11-14**); implying that *q*Fibrosis might be used to sensitively and precisely monitor the independent evolution of different collagen patterns. This applicability will certainly go a long way to address the emerging needs for insightful analysis into the pathophysiological developments occurring in different types of CLDs [137]. In viral hepatitis, it is known that the early progression of fibrosis mainly occurs in the portal tract region which is consistent with the trend in **Figure 11** that the most obvious increase appears at the transition from stage 1 to 2. The forming of septal collagen appears at the mid stage and progresses most significantly in the late stages where we see the significant increase of septal index at stage 3 to 4 in **Figure 12**.

We set Metavir system as the reference to develop *q*Fibrosis; other systems such as Knodell and Ishak systems can also be conveniently translated into *q*Fibrosis, since they essentially employ the similar architectural principles to categorize liver disease stages [23]. Within the framework of histopathological categorization, *q*Fibrosis provides scores of continuous variables due to its inherent full-quantification algorithm; thus, it potentially would have more discriminative power for precisely reflecting the dynamics of fibrosis/cirrhosis progression/regression.

Employing the similar imaging technique, Gailhouste *et al* first comprehensively validated SHG on 119 clinical liver tissue samples of mixed CLDs for scoring the amount of fibrosis via detecting fibrillar collagen density, which is similar to CPA measurement [92]. Our present study is innovative in its strategy for establishing *q*Fibrosis index with histopathological architectural features by quantitatively defining

the spatial parameters of fibrillar collagen. Another distinct contribution of our study is that *q*Fibrosis was specially trained and validated with CHB samples; thus, promoting the ready applicability of our method to align closely with clinical practice of this particular disease.

We further analyzed the performance of *q*Fibrosis against CPA. While CPA showed limitations in discrimination accuracy and higher sensitivity to sampling error, as reported before [20, 23], *q*Fibrosis exhibited significantly improved capacity to overcome the above issues. Considering the strategy taken for *q*Fibrosis design, it is rational that *q*Fibrosis would behave more similarly to conventional histological assessment system than CPA. This partly accounts for the robustness of *q*Fibrosis to sample size-dependent sampling error (i.e. sample adequacy). On the other hand, CPA has significant deviation between different samples of the same stage scores, since histological staging and amounting fibrosis (CPA) are entirely different assessments [23, 159, 160]. Collectively, the results not only support the technical strength of *q*Fibrosis for future applications, but also validate our hypothesis that the improved discriminative power of *q*Fibrosis is due to the additional input of histopathological architectural features.

We also showed that the performance of *q*Fibrosis is reproducible between the original cohort of 107 samples and the independent cohort of 55 samples imaged by different SHG imaging devices. *q*Fibrosis is highly reproducible when the image quality is consistent. The inconsistency of SHG images due to different sample processing procedures or different imaging systems could be corrected using different optical settings and be calibrated according to Guilbert *et al* [67, 161]. Thus, *q*Fibrosis is most likely to be suitable for the potential multicenter clinical research studies.

There are several exciting areas in which *q*Fibrosis may have a role in the near future. First is in the realm of antiviral clinical research and management of CHB. It has been verified recently that long-term effective antiviral therapy can lead to regression of liver fibrosis and cirrhosis in CHB patients [136, 162]. Histological analysis is currently the standard reference for performing the evaluation. Primarily established and validated with CHB samples, *q*Fibrosis may soon be sufficiently improved to serve as an automatic and reliable adjunctive tool for liver biopsy evaluation. Second is in the area of cirrhosis assessment. Regression of cirrhosis is now recognized, bringing with it increasing requirement for substaging [137, 143, 163, 164]. Due to its fully-quantitative scoring and sensitive discriminability indicated in our study, it could be interesting and valuable to further investigate the potential of *q*Fibrosis to facilitate this refinement of the dynamic subclasses of cirrhosis in comprehensively designed studies, coupled with the possible replication or correlation to other clinical markers such as FibroScan [165] and hepatic vein pressure gradient (HVPG) [103]. Last but not least, since experienced hepatopathologists are a rare breed in most setups, *q*Fibrosis might act as a valuable aid to pathologists to produce consistent staging of liver fibrosis; as well as to provide on-site expert consultation to the non-expert pathologists. In laboratories without SHG microscopy, *q*Fibrosis values can be obtained from images of stained biopsy samples using routine light microscopy, as long as accurate identification of collagen can be ensured. The examples of both Masson Trichrome-stained and Sirius Red-stained images with *q*Fibrosis evaluation are shown in **Figure 27**.
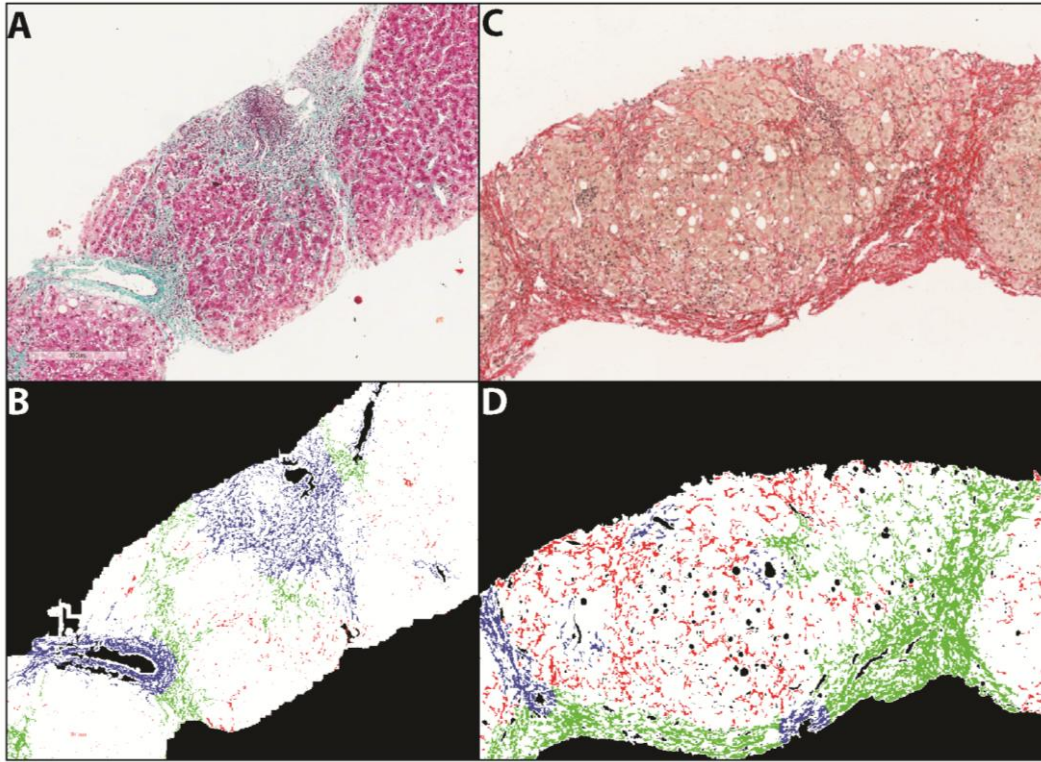
Figure 27: An example of the processing of Masson Trichrome-stained human biopsy sample. (A) The Masson Trichrome-stained image of a human biopsy sample of stage 4 is shown. The collagen patterns are stained green. (B) The portal (blue), septal (green) and fibrillar (red) collagen patterns are successfully identified using the proposed image analysis technique.

Meanwhile, it must be noted that performance of qFibrosis can be affected by the quality of samples in the training set; as evident from the higher AUC values obtained in staging larger animal samples in our results. This is because establishment of qFibrosis is basically the generation of an algorithm by training-and-learning with the sample's imaging data. Thus, in our future work, more qualified biopsy samples for training purpose will be needed to improve the performance of qFibrosis; and recruiting a larger set of samples for a multicentre clinical study would be necessary to generalize the capability of qFibrosis and validate its clinical applications. In addition, since its target sample is liver biopsy, however superior the diagnostic utility of qFibrosis, invasiveness of the assessment is still an inherent limitation against its

widespread application. Moreover, since liver biopsy provides comprehensive information not limited to fibrosis, but also necroinflammtion, steatosis and other specific pathological features, *q*Fibrosis should be used properly only when the fibrosis assessment is needed.

The performance of *q*Fibrosis is also affected by the image analysis tools used. Regarding to the recognition of three collagen patterns, one of the key step is to accurately locate the portal tract and central veins from the tissue image. In the TPEF image from the unstained tissue sample, as no additional cellular or nuclei information can be used, it is very difficult to separate the targeted tracts and veins with the other artifacts such as irregular shaped sinusoidal spaces. More importantly, it is almost impossible to separate portal tract and central vein according to morphology only. This could possibly be achieved in stained images where special staining can be potentially performed to highlight centre-lobular cells around central veins. It would have a huge improvement if portal tract and central vein regions can be separated as the progression of fibrosis varies differently in these two regions, indicating different stages of disease progression.

More features could also be explored from the three collagen patterns identified. Besides the morphological and spatial features adopted in this study, other features such as fractal geometry or texture could potentially play an important role. Other machine learning approaches can also be tested in future, such as support vector machine or artificial neural network. The proper design of the machine learning framework can significantly improve the final classification performance. The study in this chapter has proved the advantage of using pathological relevant approach to build the automated analysis system for liver fibrosis assessment, but it is always

worth the further investigation and tuning of the proper pieces and parameters in the analysis framework to optimize the system performance.

3.5 Conclusions

*q*Fibrosis has been established and validated in this chapter to provide fully-quantitative scores incorporating histopathological features for liver fibrosis evaluation. It faithfully recovers the staging results of conventional histological assessment systems; while in the meantime, effectively ameliorating the inherent issues of current systems regarding sampling error, observer variation and cirrhosis intra-staging. *q*Fibrosis can potentially be a valuable adjunctive tool to enhance the role of liver biopsy for accurate and objective assessment of fibrosis in clinical research and management of CLD.

Chapter 4

Capsule Index, quantitative liver fibrosis assessment from liver surface

4.1 Introduction

Liver fibrosis is associated with the excessive accumulation of collagen in the extra-cellular matrices of the liver, which occurs in chronic liver diseases that affect millions of people worldwide causing high morbidity and mortality rates [1]. Hence, much effort has been placed in developing markers for staging and grading fibrosis, evaluating anti-fibrotic drug efficacy, and predicting fibrosis progression, regression and liver de-compensation [166]. Liver biopsy is the gold standard for staging liver fibrosis in patients with chronic liver diseases [167]. However, it has several disadvantages such as being invasive, providing poor sampling volume, and inter-/intra-pathologist staging variations [23]. Most importantly, repeated biopsies for monitoring disease status and efficacy of treatment are painful for patients, and risk other complications [168].

To overcome these problems, various non-invasive diagnostic tools are proposed ranging from advanced medical imaging modalities to serum biomarker assays [169]. Nevertheless, ultrasound and magnetic resonance imaging (MRI) [170] cannot identify early and mild fibrosis stages due to their limitations in image resolution [171]. Liver stiffness measurement using transient ultrasound elastography (Fibroscan) [172, 173] or magnetic resonance elastography (MRE) [174, 175] provide no cellular and tissue level information; and their performances in fibrosis evaluation are still

under validation [176, 177]. The accuracy of serum biomarkers to predict fibrosis progression is also reported to be unsatisfactory since these biomarkers are indirect expression of the liver fibrosis process and are easily affected by other factors such as systemic inflammation [178, 179]. Motivated by our previous findings that surrogate histological markers such as collagen proportionate area (CPA) in liver sub-capsule region are consistent with those measured in liver interior and are well-correlated with fibrosis stages [180], we hypothesize that liver surface scanning can be a potential alternative to liver biopsy. With the advance in endomicroscopy and laparoscopic surgical techniques [181], we envision the possibility of liver surface scanning to reduce the invasiveness and associated risks of liver biopsy taking samples from the liver interior. Liver surface scanning with SHG endomicroscopy has the potential to replace liver biopsy in most of the scenarios in routine clinical practice where liver biopsy is needed for fibrosis assessment, such as the prognostic of fibrosis progression and regression for treatment planning and evaluation of treatment efficacy. Liver surface is covered by a collagenous layer called the Glisson's capsule [182]. The thickness of the Glisson's capsule has been reported to increase during fibrosis progression [107, 180] as imaged from the biopsied liver tissue sections perpendicular to the liver surfaces, which does not reflect the overall structural changes of the collagen in the Glisson's capsule. The histo-pathological features that are used in routine semi-quantitative scoring systems [183-185] by pathologists to stage liver fibrosis are also derived from the cellular and tissue structures in the liver interior that cannot be observed on the liver surface. To investigate the feasibility of liver surface scanning as an alternative to liver biopsy for scoring fibrosis, we would need to extract all relevant liver surface features, especially on the Glisson's capsule which is essentially bundles of collagen fibers [109]. Second harmonic imaging (SHG) is a

96

powerful tool for visualization and quantification of collagen fibers in various tissue states including liver fibrosis [92, 186-188]. As the capsule collagen is the outer-most layer wrapping the entire liver; and it generates appreciable backward second harmonic signals, SHG imaging in reflective mode can be employed for stain-free quantitative imaging of the liver surface. It would also be possible to image larger areas of the liver surface than liver biopsy whose limited sampling volume often causes errors in fibrosis scoring [20, 189].

In the study of this chapter, we have imaged the liver surfaces from 65 rats of two disease models, thioacetamide (TAA) and bile duct ligation (BDL), which represents parenchymal and biliary fibrosis [190, 191] respectively, to induce liver fibrosis, using reflective second harmonic (R-SHG) imaging. Image analysis was performed to extract 125 features that characterize the morphology and texture of the collagen network of the Glisson's capsule. These features, together with the capsule thickness, were combined to build one single index – capsule index by multinomial logistic regression (MNL) after feature selection. Good performance is found for the detection of fibrosis at different stages by capsule index, enabling liver surface scanning as a viable alternative to biopsy.

4.2 Materials and Method

4.2.1 Animal tissue preparations

Male Wistar rats at an average weight of 220g were housed two per cage in the Biological Resource Centre (BRC) of Biopolis, A*STAR with free access to laboratory chow and water in a 12:12h light/dark schedule. The Institutional Animal Care and Use Committee (IACUC) approved all animals-related experiments.

Thioacetamide (TAA) induced fibrosis

Thirty-five rats were randomly separated into seven groups, and a group of five as control rats. These were treated with thioacetamide (TAA) 200mg/kg by intraperitoneal injection three times a week for 14 weeks to induce liver fibrosis. The 35 rats in the TAA-treated group were sacrificed at time-points of 2, 4, 6, 8, 10, 12, and 14 weeks (n = 5 per week). 5 rats of the control group were also sacrificed at week 0, without treatment. Cardiac perfusion with 4% paraformaldehyde was performed to flush out blood cells and the liver was fixed before harvesting.

Bile duct ligation (BDL) induced fibrosis

Twenty-five rats were randomly separated as five groups of five. BDL of rats was performed under general anesthesia with ketamine (100mg/kg body weight). A midline abdominal transverse incision was performed after shaving of the abdomen, exposing the liver and intestines. After gently and skillful displacing of the liver and intestines, the lower end of the bile duct was identified at its insertion into the small intestines and traced up towards the porta, which was then doubly ligated in two areas near the porta with silk sutures (USP 3-0) and transacted between the two ligation points. Abdominal contents were gently rearranged and the wound closed in a double-layered tissue closure with vicryl sutures. A total of 20 rats were ligated and sacrificed at intervals of 1, 2, 4 and 6 weeks (n = 5 per week). Similarly, 5 rats were sacrificed at week 0, without ligation, to serve as the control group. Cardiac perfusion with 4% paraformaldehyde was performed to flush out blood cells and the liver was fixed before harvesting.

The left lobe of each liver was used for imaging, as there were no differences of the features between the left and right lobe of the same liver, both from the capsule and sub-capsule regions [180]. The volume of left lobe of liver increased significantly along fibrosis progression in BDL model (stage 0: 4.1 ± 0.2 cm^3, stage 1: 4.4 ± 0.6 cm^3,

stage 2: 4.6±0.4 cm^3, stage 3: 6.8±1.2 cm^3, stage 4: 9.4±1.3 cm^3). On the other hand, the volume of left lobe of liver decreased in the course of fibrosis progression in the TAA model (stage 0: 4.1±0.2 cm^3, stage 1: 3.6±0.6 cm^3, stage 2: 3.1±0.6 cm^3, stage 3: 2.7±0.5 cm^3, stage 4: 1.9±0.4 cm^3).

4.2.2 Image acquisition

The non-linear optical microscope was developed based on a multiphoton and confocal imaging system (LSM510Meta, Carl Zeiss, Heidelberg, Germany) using an external tunable mode-locked Ti:Sapphire laser (Mai-Tai broadband, Spectra-Physics, USA). A schematic of the set-up is shown in **Figure 28**, where the laser was passed through a pulse compressor (Femtocontrol, APE GmbH, Berlin, Germany) and an acousto-optic modulator (AOM) for group velocity dispersion compensation and power attenuation respectively. Laser was then routed by a dichroic mirror (reflect >700nm, transmit <543nm), through an objective lens (plan-neofluar, 20X, NA=0.5, Carl Zeiss, Heidelberg, Germany), to the tissue specimen. The average power at the objective lens is ~80mW. Two-photon excitation fluorescence microscopy (TPEF) signals in the epi-direction was collected by the same objective lens and recorded by a photo-multiplier tube (PMT, Hamamatsu R6357, Tokyo, Japan), after passing through the dichroic mirror (reflect <490nm, transmit >490nm) and a 500-550nm band-pass (BP) filter. SHG signals were collected similarly but with a 390-465nm band-pass filter before reaching the PMT.
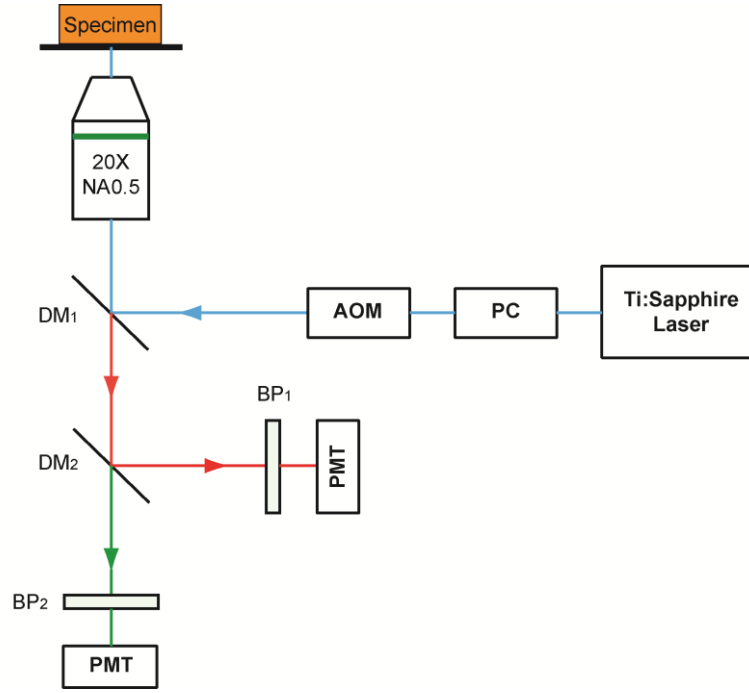
Figure 28: Schematic illustration of the optical set-up.

The detector gain and amplifier gain and offset settings of the photomultiplier tube of our system were optimized to eliminate under- or over-saturation. Noise floor was typically around 200 intensity counts. The number of pixels per image plane was fixed at 1024 by 1024 for varying depths into the tissue with a 12-bit data depth. A z-stack of TPEF and SHG images were taken at 10 randomly selected sites on the anterior surface of the left lobe of each liver sample with a field of view of 450 μm by 450 μm. The thickness of the z-stack is variable as it depends on the complete attenuation of the reflective SHG signals as we scan deeper into the tissue. Time taken to image a typical 450 μm by 450 μm by 30 μm z-stack is about 100 seconds (1024 by 1024 pixels per plane with a spot dwell time of 3.2×10^{-6} seconds). Hence, imaging 10 random sites would need 1000 seconds (about 17 minutes) per sample without considering the time taken in between stage movement and re-focusing. Images were acquired 3 days after formalin fixation of the harvested livers so as to allow stable cross-links to form and the morphology be preserved.

For comparison with conventional histopathology scoring, 5 µm thick tissue slices were sectioned from each liver sample, the biopsy spot being within 0.5 cm radius of the imaged sites, stained with Masson Trichrome (MT) stain kit (ChromaView advanced testing, #87019, Richard-Allan Scientific) and imaged with bright-field microscopy (Aperio Digital Pathology Environment).

4.2.3 Histo-pathological scoring

Each sample was scored by a pathologist based on blind reading of the MT image to reduce any bias using Metavir score [183]. In the Metavir scoring system, liver fibrosis was classified into five stages from F0 to F4 according to the severity of fibrosis: no fibrosis, fibrous portal expansion, few bridges or septa, numerous bridges or septa, and cirrhosis [192].

4.2.4 Image pre-processing

To reduce computation time and cost for image segmentation and feature extraction, the original three-dimensional (3D) image z-stack was rendered by a 2D representative image. Since the liver surface was not always perpendicular to the z-direction of the image stack, the 3D stack was rotated first. To identify the rotation angle, MIP was first performed along the y-direction (**Figure 29A**) and the centerline of the capsule was recognized by extracting the maximum intensity pixels along the z-direction in x-z images, after which the stack was rotated around the y-axis by the degree θ calculated from the angle between the centerline and the z-axis (**Figure 29D**). Similar procedure was performed to rotate the stack around the x-axis; where MIP was applied along x-direction and the rotation angle was identified from the angle between the centerline and the y-axis (**Figure 29B, E**). MIP was finally applied to the rotated image stack along z-direction to generate the representative 2D image (**Figure**

29C, F). As the Glisson's capsule was generally less than 20 μm thick in z-direction only, the projected image contained most of the structure and architectural information of the 3D image stack and hence, it is a good representation of the Glisson's capsule.
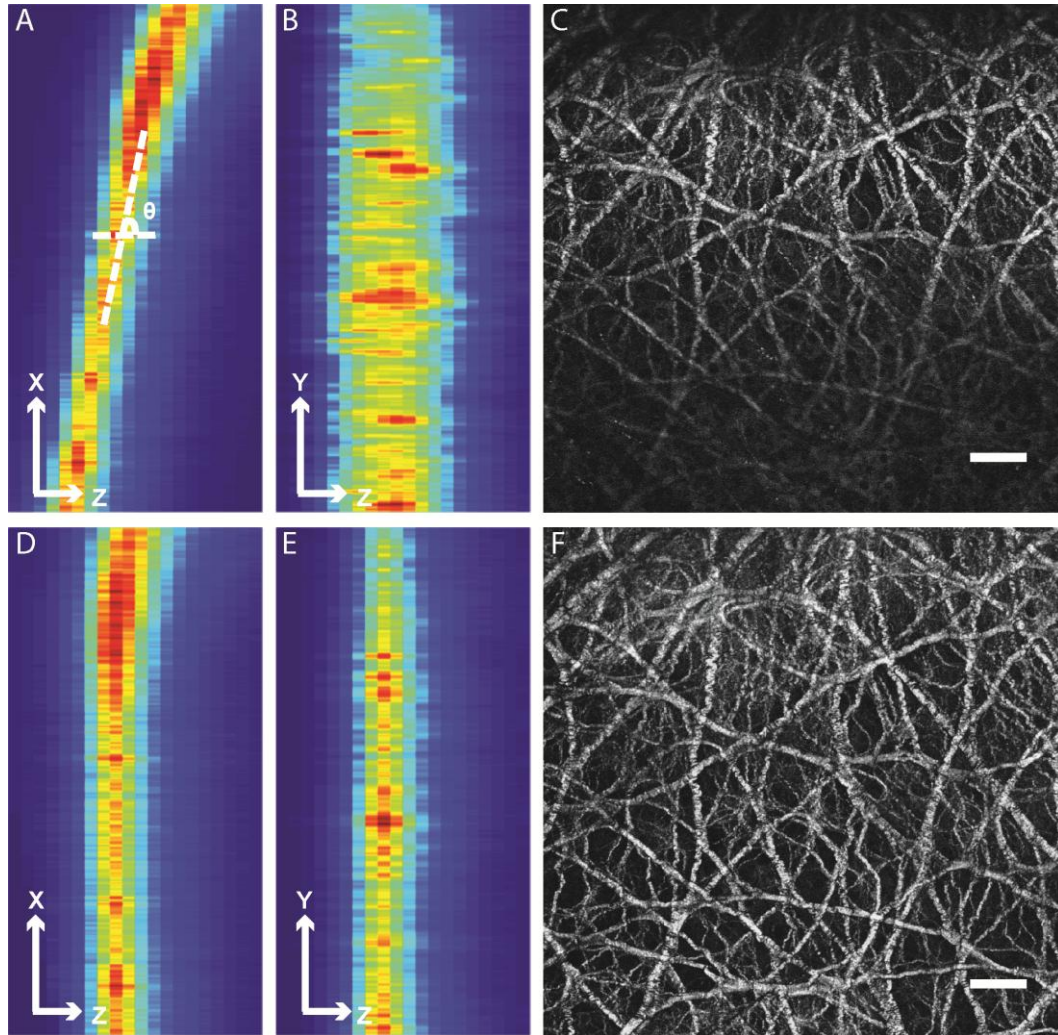
Figure 29: Comparison between the Glisson's capsule images before and after pre-processing. (A) Maximum intensity projection (MIP) of the image stack along y-direction before pre-processing. The rotation angle was defined as the angle between x-axis and the centerline of the band with high pixel intensities. (B) MIP of the image stack along x-direction before pre-processing. (C) The 2D representative image of the image stack before pre-processing. The scale bar represents 50um. (D) MIP of the image stack along y-direction after pre-processing. (E) MIP of the image stack along x-direction after pre-processing. (F) The 2D representative image of the image stack after pre-processing. The scale bar is 50um. The pixel intensity distribution is more uniform in the representative 2D image after pre-processing.

4.2.5 Fiber tracing in capsule collagen network

We follow the existing skeletonization based method to extract the centerlines of the collagen fibers, and adopt a gap filling method to connect broken fiber ends. The collagen fiber tracing algorithm proposed has three stages: vectorization stage, gap filling stage, and tracing stage (**Figure 30**). The first stage is to generate a vector representation of the collagen fibers segmented from the original SHG image. The second stage is to correct the errors in the graph representation of the collagen fiber network, due to the degradation of image quality and the segmentation procedure, by connecting proper gaps between the nodes in the graph according to a confidence score calculated. Such processing could preserve the topology of the collagen fiber network at the Glisson's capsule. Finally, the centerline of each collagen fiber is traced in the last stage.
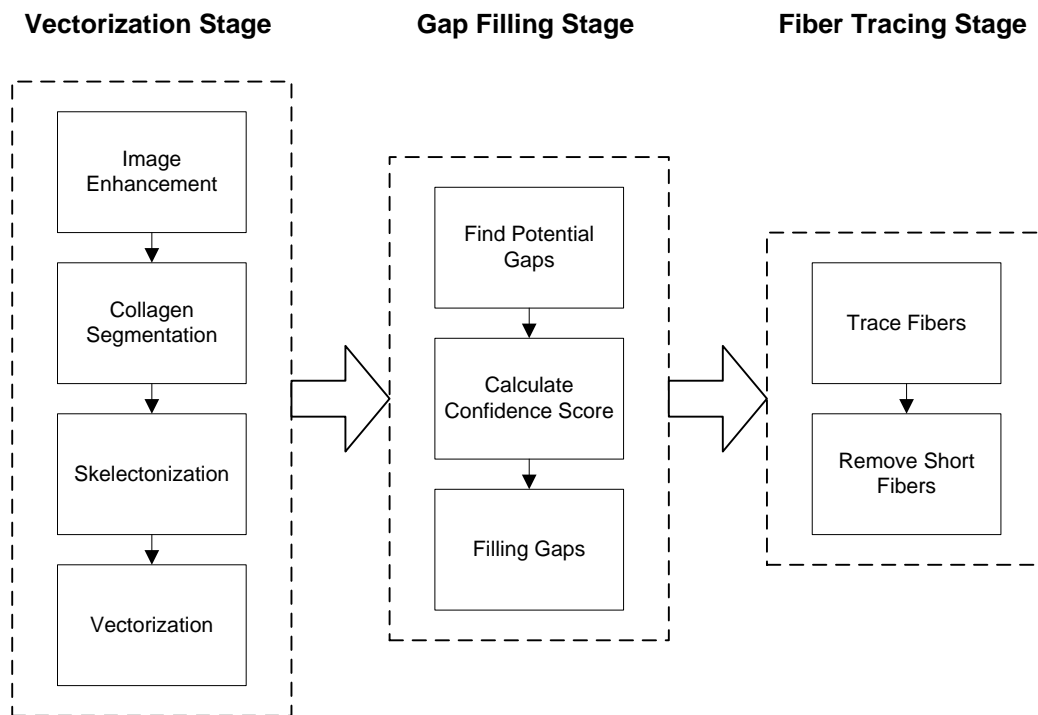
Figure 30: The flow chart of the proposed fiber tracing algorithm.

4.2.5.1 Network vectorization

Image enhancement

The SHG image was first filtered by the Frangi filter [193] to enhance the collagen structures from the noisy background. The Frangi filter is designed to convolve the image with second derivation of a Gaussian kernel at different directions and the convolution results of each pixel are recorded in the Hession matrix,

$$H(p) = \begin{bmatrix} I_{xx}(p) I_{xy}(p) \\ I_{yx}(p) I_{yy}(p) \end{bmatrix} , \quad \text{where} \quad I_{xx}(p) = (I * \frac{\partial^2}{\partial_x \partial_x} G)(p) , \quad I_{yy}(p) = (I * \frac{\partial^2}{\partial_y \partial_y} G)(p) ,$$

$$I_{xy}(p) = f_{yx}(p) = (I * \frac{\partial^2}{\partial_x \partial_y} G)(p) \quad \text{and} \quad G = \frac{1}{2\pi\sigma^2} \exp(-\frac{x^2 + y^2}{2\sigma^2}) , \quad * \text{ denotes the spatial}$$

convolution. If there is a linear structure existed, a principle direction could be found by decomposition of these second order structures through eignvalue analysis. Hence, if we denote the two eignvalues from the Hessian matrix as λ_1 and λ_2, we should have the absolute value of one eigenvalue much higher than the absolute value of another. To enhance the intensity of pixels that are more likely to present a linear structure, their values are then replaced by a measure defined as

$$I_{frangi}(p) = \exp(-\frac{(\lambda_1/\lambda_2)^2}{2\beta^2})(1 - \exp(-\frac{(\lambda_1^2 + \lambda_2^2)}{2c^2})) , \text{ where } |\lambda_1| < |\lambda_2| \text{ and } \lambda_2 < 0 .$$

As explained, we will have small λ_1/λ_2 and large $\lambda_1^2 + \lambda_2^2$ for a pixel with linear structure which tends to assign a high I_{frangi} value for such pixels. Although the Frangi filter is originally designed for vessel enhancement, it could be extended to the applications of any tubular/linear structures such as neuron [194]. We feel that it is

also appropriate for collagen structure enhancement as collagen fiber consists of triple helix structure which is tubular as well.

In our experiment, we fixed the β and c at 0.5 and 15 respectively, and investigated different scales of the Gaussian kernel with σ from 1 to 8. Every pixel was assigned the maximum output value among all the scales assessed.

Segmentation

The enhanced image was then segmented into collagen and background using the segmentation algorithm based on Gaussian mixture models, which was shown to be more accurate than other methods such as global thresholding and clustering methods for collagen segmentation in the previous chapter. The morphological closing is then performed to smooth the binary mask of the collagen and any segment with less than 5 pixels was removed.

Skeletonization

The initial centerlines of the binary mask of the segmented collagen are extracted by skeletonization. Since the boundaries of the segmented collagen areas are usually noisy, the classic skeletonization methods based on morphological thinning are not appropriate as the skeletons extracted could be affected by spurious branches. We implemented a skeletonization method proposed by Telea et al. [195] which is based on the distance transform of the boundary points. Fast Marching Method (FMM) was used to evolve the boundary towards inside of the collagen area. The original image was initialized by calculating the count of boundary points followed by FMM to generate the map of evolved count inside the object. The derivative count map was then produced after computation and thresholding was performed on the map to locate

the skeleton points. The thinning processing is further performed for the identified skeleton points if they are not one-pixel in width.

Vectorization

The skeleton is next represented by a graph, $G = (V, E)$, where each vertex $v_i \in V$ is a point on the skeleton and each edge $e_k = (v_i, v_j) \in E$ connects two neighboring vertexes on the skeleton. The vertexes are further identified into three types (end points, curve points and branch points) based on the number of their neighboring vertexes:

$$v_i = \begin{cases} End\ Po\text{int}, & if\ \deg(v_i) = 1 \\ Curve\ Po\text{int}, & if\ \deg(v_i) = 2 \\ Branch\ Po\text{int}, & if\ \deg(v_i) = 3 \end{cases}.$$

The graph G, together with the original SHG image, the binary mask of the segmented collagen and the filtered grey-scale image, are used in the following stages to fill the gaps and trace the collagen fibers.

4.2.5.2 Gap filling

The collagen network topology is strongly affected by the discontinuities of the segmented collagen fibers due to the influence of noise. The gaps are formed between the closest discontinuous collagen fibers, which could be reduced to a certain extent by the proper usage of image enhancement and segmentation methods. However, the disconnected fibers still exist in the resulting network, which makes the following quantification of collagen network features not accurate. Hence, it is necessary to adopt a gap filling algorithm to preserve the real collagen network topology.

Locate potential gaps

A direction profile is established for each end point, which uses a plurality of directions in its neighborhood. The distribution of intensities is characterized in each direction to decide whether a tubular structure existed. For any existing tubular structure without the identified skeleton, a gap is located and will be filled.

We first create a circular neighborhood with radius N_{ep} around each end point, where N_{ep} is defined as five times of the shortest distance from that end point to the background. Hence, the size of neighborhood assessed is proportional to the width of collagen fiber that end point belongs to. In the neighborhood, the direction profile is defined as the intensity variation with respect to the directions to that point. It is assumed that, along the direction where a tubular structure existed, the variation of intensity should be low. We adopted and modified the definition of "vesselness" measure from Qian [196] by using the average squared intensity deviation as the measure of the intensity variation, which is defined as

$$Sid_i(\theta) = \exp(-\frac{1}{N_{ep}}\sum_{r=1}^{N_{ep}}(I(v_i) - I(u_{i,r,\theta}))^2), 0 \leq \theta < 2\pi$$, where v_i is the end point i and

$u_{i,r,\theta}$ is the point with distance r and direction θ to the end point i.

In each direction profile, there exists a significant peak representing the direction where the original collagen fiber is. If there is any other peak existed in the direction profile which has *Sid* measure higher than 50% of that of the significant peak, these directions are considered as where the potential gaps are. The ratio can be tuned to control the sensitivity of the detection of potential gaps.

Finally, starting from an end point through each of the directions detected for the potential gaps, we find the nearest vertex located on this direction as the other end of the potential gap and will decide whether an edge needs to be built to fill this gap according to a confidence score illustrated in the following section.

Calculate confidence score

A path is first recognized to link the two ends of each potential gap by finding the optimal connections of image pixels between them. A confidence score is proposed to reflect the intensity variation on this path. A low confidence score indicates that the path should not be kept and the gap does not need to be filled.

For a potential gap, we consider the local image area in the bounding box of the points at the two ends of the gap as a weighted graph $G_a = (V, E, W)$, where V is the vertex set containing all the pixels in the local image area, E is the set of all the edges that connect neighboring vertexes/pixels, and W consists of the weights of each edge in set E. Given the points v_0 and v_n at the two ends of the gap, we aim to find a path p from v_0 to v_n in the graph G_a which has the smallest overcall weight. We design the overall weight W_{all} for a path $p = \{v_i \mid i = [0, n]\}$ as $W_{all}(p) = \sum_{i=0}^{n-1} W(v_i)$, and $W(v_i) = w_1 |v_{i+1} - v_i| + w_2 \left(1 - 0.5 * (I_{frangi}(v_i) + I_{frangi}(v_{i+1}))\right)$. The first term in the weight function W emphasizes the distance between the neighboring vertexes on the path which gives higher cost for the longer path. The second term generates higher cost if the vertexes on the path that are less likely the collagen points which tend to have smaller frangi filtered values. The Dijkstra's algorithm [197] is applied to find the path with the lowest cost.

The confidence score for the identified path p is defined as

$$CS(p) = \exp(-(\frac{1}{n}\sum_{i=1}^{n} Dev(p)) \Big/ \arg\max_{i=1}^{n}(Dev(p))), \text{ where } Dev(p) = (I(v_i) - I(v_0))^2.$$

This probability function computes the generalized likelihood ratio test of the linear structure, which is used as the criteria to determine the connection of the gap through the identified path.

Filling gaps

We set a threshold of 0.1 to the confidence score. If the score is higher than 0.1, the gap is filled by updating the vertexes and edges in the graph G. This threshold is tuned and chosen according to several experiments on some sample images and is kept consistent for all the images.

If one end of the gap to be filled is originally an endpoint, it is updated as a curve point in the graph; otherwise, it is updated as a branch point. If a branch point is added, we further check whether it is close to any of the existing branch point and merge them if any exists.

4.2.5.3 Fiber tracing

Trace fibers

To trace each fiber in the graph G, we start from each end point through the connecting curve points towards another end point or branch point. If another end point is reached, a complete fiber is traced and updated in the fiber list. Otherwise, the fiber is stored as an uncompleted fiber for further processing. We next start from each branch point through the connecting curve points towards another branch point and updated in the uncompleted fiber list as well.

For all the uncompleted fibers which share same branch point as one end, they are connected if having similar orientations that the difference of the orientation of these two uncompleted fibers was smaller than a threshold of 60 degrees. The connected uncompleted fibers were finally updated in the complete fiber list.

Remove short fibers

The short fibers will be removed since they are likely the false branches from the skeleton of collagen fibers. A fiber will be considered as the candidate of short fiber to be deleted if at least one end is a branch point. The threshold is set as 5 pixels to delete all candidates shorter than this.

An example of the image processing of fiber tracing was show in **Figure 31**.
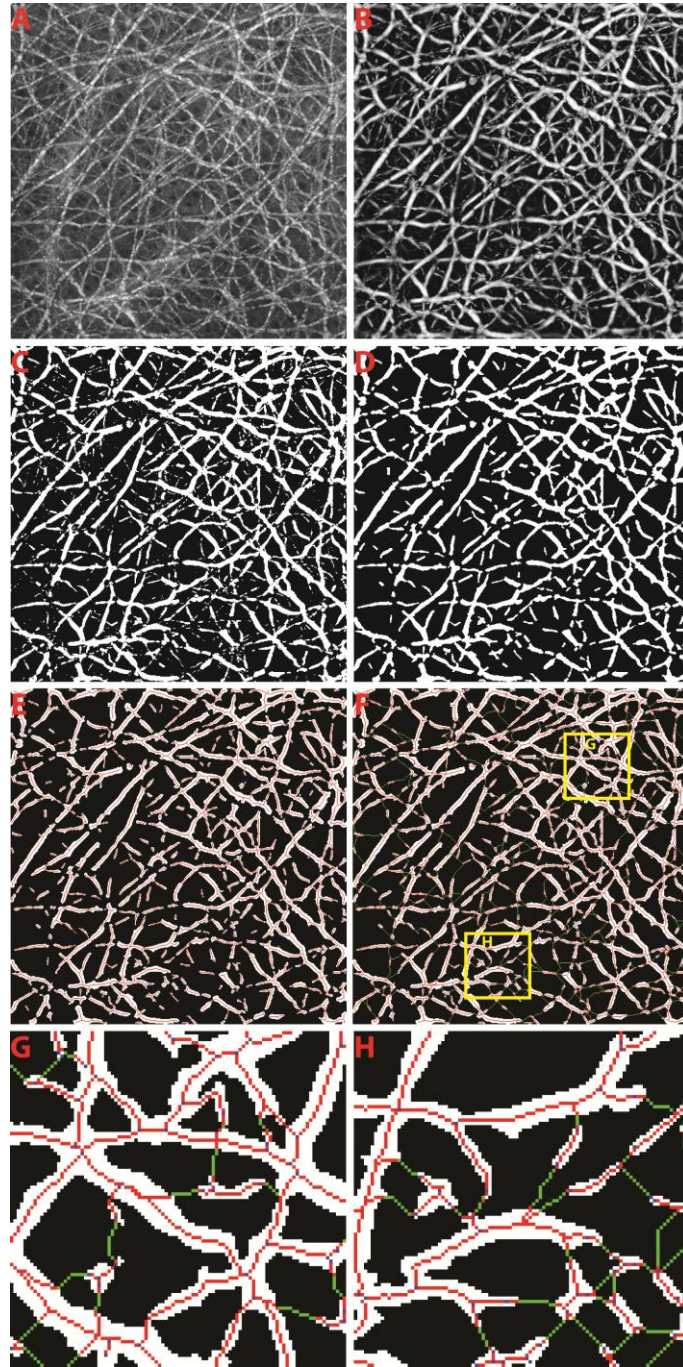
Figure 31: The illustration of image processing to trace collagen fibers from the collagen network. The raw capsule image is shown in (A). The enhanced image after Frangi filtering is shown in (B). The binary image after collagen segmentation is presented in (C). (D) shows the final segmented image of collagen after morphological operations to remove the small objects. The initial skeletons of each collagen segment are shown in (E). (F) The gap filling method was performed to finally connect the broken collagen fibers where the connected pixels are shown in green. Two regions-of-interest are shown for example in (G) and (H).

4.2.5.4 Generation of artificial collagen network

The artificial network is generated by growing one fiber at a time until the network achieves the desired fiber number N_A. The image size of each artificial network is set to 512 pixels by 512 pixels which is the same as the SHG image from the liver capsule. The lengths of all N_A collagen fiber were assigned by following an exponential distribution with mean at 200 pixels. When a new fiber is added, an initial point was generated at a random position in the image. The initial direction of the fiber was also randomly generated. The fiber was extended from the initial point to a new end at the step of 3 pixels (around $1\,\mu m$) followed the initial direction. If the length of the fiber has not reached the assigned length and the fiber did not reach the boundary of the image, the fiber continued to extend to a new end at the same step size. The new direction of the extension was defined by adding a random turbulence generated between 0 to 60 degrees to the previous fiber extension direction. This fiber growing process is repeated until all N_A fibers were added to the image and the skeletons of the artificial network were generated.

The next step is to locate the cross-link points of all the collagen fibers. A threshold at 3 pixels was set as the minimum distance between two cross-link points, and any pair of cross-link points was merged if their distance was lower than the threshold. The skeleton image of the artificial network was then convolved with a 2D Gaussian filter with standard deviation of 3 pixels to create the artificial image. We chose the same value for the standard deviation of the Gaussian filter and the threshold of the minimum distance between two cross-link points to ensure that every cross-link point in the image was detectable in the convolved artificial image. In order to test whether the developed fiber tracking algorithm is suitable for noisy SHG images of the liver

capsule, we finally added the random generated noise to the image at different signal levels.

4.2.6 Capsule feature extraction

To characterize the collagen capsule network at liver surface, we extracted 125 features as listed in **Table 13**.

Table 13: Summarization of all 125 features extracted.

No.	Feature Descriptions
Morphological Features [114]	
1	Number of fibers
2	Number of cross-links
3-4	Mean and variation of the size of pores
5	Number of pores
6-7	Mean and variation of fiber length
8-9	Mean and variation of fiber width
10	Amount of collagen
11-12	Mean and variation of cross-link spaces
13-14	Mean and variation of cross-link densities
15-16	Mean and variation of the straightness of fibers
Texture Features	
17-28	Contrast, correlation, energy and homogeneity from the GLCM given three different pixel distances at two, four and eight pixels [198]
29-34	Energy, entropy, mean, standard deviation, third moment and fourth moment of the coefficients from Fourier transform [201]
35-94	Energy, entropy, mean, standard deviation, third moment and fourth moment of the wavelet decomposition coefficients from ten sub-images generated by Daubechies wavelet transform [199]
95-124	Energy, entropy, mean, standard deviation, third moment and fourth moment of the magnitude of the convolution over the image with Gabor filter at five scales [200]
3D Feature	
125	Capsule thickness

4.2.6.1 Morphological features

The reticular properties of a collagen network are important for the better understanding of its microstructure and biological role. We characterized 16 morphological features to represent the geometrical and topological distributions of the collagen network.

1. Number of fibers: the number of medial axis traced in the image.

2. Number of cross-links: the number of cross-link points that is defined as those points on the medial axis belonging to more than one collagen fibers.

3-4. Mean and variation of pore sizes: the average and standard deviation of the areas of empty spaces that are completely surrounded by fibers in the network.

5. Number of pores: the number of empty spaces that are completely surrounded by fibers in the network.

6-7. Mean and variation of fiber length: the average and standard deviation of the lengths of medial axis of each collagen fiber.

8-9. Mean and variation of fiber width: the average and standard deviation of the fiber width was defined as the area of the collagen segment divided by the length of the medial axis of the segment.

10. Amount of collagen: the number of pixels that belongs to collagen divided by the total area of the image.

11-12. Mean and variation of cross-link spaces: the average and standard deviation of the cross-link spaces quantified as the distance between two neighbouring cross-link points on the same fiber.

13-14. Mean and variation of cross-link densities: the average and standard deviation of the cross-link densities defined as the number of cross-link points from one collagen fiber divided by its fiber length.

15-16. Mean and variation of the fiber straightness: the average and standard deviation of fiber straightness calculated as the the absolute distance between the two ends of the fiber divided by its length.

4.2.6.2 Texture features

Textures are important information of any object in an image. Thus, we extracted a total of 108 texture features including gray-level co-occurrence matrix (GLCM) based features [198], Daubechies wavelet transform based features [199], Gabor filters based features [200] and Fourier transform based features [201].

GLCM features

GLCM is one of the most widely used texture analysis methods proposed by Haralick [198] first. Each entry $Co(i,j)$ in GLCM corresponds to the number of occurrences of the pair of gray levels i and j which are a certain distance apart in original image. Several second order texture features can be calculated from GLCM, including contrast, correlation, energy and homogeneity. These second order measures consider the relationship between groups of two (usually neighbouring) pixels in the image which are defined as below.

$$\text{Contrast} = \sum_{i,j} |i-j|^2 Co(i,j)$$

$$\text{Correlation} = \frac{\sum_{i=1}^{Ng} \sum_{j=1}^{Ng} (ij)Co(i,j) - \mu_x \mu_y}{\sigma_x \sigma_y}$$

$$\text{Energy} = \sum_{i,j} Co(i,j)^2$$

$$\text{Homogeneity} = \sum_{Co \in \Omega} \frac{Co(i,j)}{1+|i-j|}$$

where $Co(i,j)$ is the entry of co-occurrence matrix, Ng is the number of grey-level in the original image after quantization, and μ_x, μ_y, σ_x and σ_y are the means and standard deviations of $Co_x(i) = \sum_{j=0}^{Ng-1} Co(i,j)$ and $Co_y(j) = \sum_{i=0}^{Ng-1} Co(i,j)$.

We calculated contrast, correlation, energy and homogeneity [198] from the GLCM with three different pixel distances of 2, 4 and 8 used as the distance between the pixel of interest and its neighbours to create the co-occurrence. At each pixel distance,

each feature was averaged from four different directions of adjacency (horizontal, vertical, left and right diagonals) from the GLCM.

Fourier features

Fourier transform transforms the original image into the frequency domain to generate the power spectrum of the signal so as to detect the repetitive patterns of texels and to capture the details of the texture. After Fourier transform of the capsule SHG image, we calculated energy, entropy, mean, standard deviation, third moment and fourth moment of the coefficients of the Fourier series.

Daubechies wavelet features

The wavelet features are also widely used in different image retrieval applications. As a wavelet is defined as a function to represent a continuous time signal into different frequency components, an image could be decomposed into several sub-bands by applying discrete wavelet transform while each sub-band represents the original image at different levels of details.

One of the most widely used families of orthogonal wavelets is Daubechies wavelets. Thus, in this study, a three-level Daubechies wavelet transform was preformed to generate ten sub-images from the original image. For each sub-image, the first 10 nonzero wavelet decomposition coefficients were used and the energy, entropy, mean, standard deviation, third moment and fourth moment [199] of these coefficients were calculated as the Daubechies wavelet features.

Gabor wavelet features

The Gabor wavelet transform used a Gaussian kernel function so that both frequency and spatial representations are similar to the human visual system. Its advantage is to be able to decompose the original signals in frequency and spatial domains simultaneously.

To calculate Gabor wavelet transform features, the original image was initially convolved with a Gabor filter with five wavelet scales and six filter orientations. Energy, entropy, mean, standard deviation, third moment and fourth moment [200] of the magnitude of the convolution over the image at each scale were then calculated by averaging each measurement from six orientations at the same scale.

4.2.6.3 Capsule thickness

The capsule thickness was calculated from the rotated image stack before the MIP was performed. The thickness was defined as the width of the band with high pixel intensities in the x-z or y-z image (**Figure 29**) [180].

4.2.7 Feature selection

Feature selection was applied to recognize the best subset among all 126 features that are the most relevant to fibrosis progression. Support vector machine recursive feature elimination (SVMRFE) approach [202] was first adopted to rank all the features. SVMRFE was introduced as a multivariate feature ranking method that uses SVM weights as the ranking criterion of features. Starting from using all the features, a SVM was trained and features were sorted by the absolute value of their weight in the hyper-plane. The feature with the least weight was least important and was eliminated from the feature set and a SVM was trained again using the new feature set after elimination, this process was performed iteratively until all the features had been removed. All the features were hence ranked during this recursive elimination procedure.

The diversities were generated on the training set by the bootstrapping method [203], after which SVMRFE was applied on each of these bootstrap samples and a diverse set of feature rankings was obtained. The ensemble rankings of all the features were aggregated by summing the ranks over all bootstrap samples [152] for each feature.

116

Different numbers of the features were selected according to the ensemble rankings from the top order to train a SVM on the bootstrap samples and be evaluated on the out-of-bag samples based on the area under the receiver operating characteristic curve (AUC) [204], which was a measure of test performance. The subset of the features that lead to the highest AUC among all was finally selected.

4.2.8 Establishment of Capsule Index

The image analysis system developed to quantify capsule index, a continuous measurement of the Glisson's capsule, to stage liver fibrosis was shown in **Figure 32**.
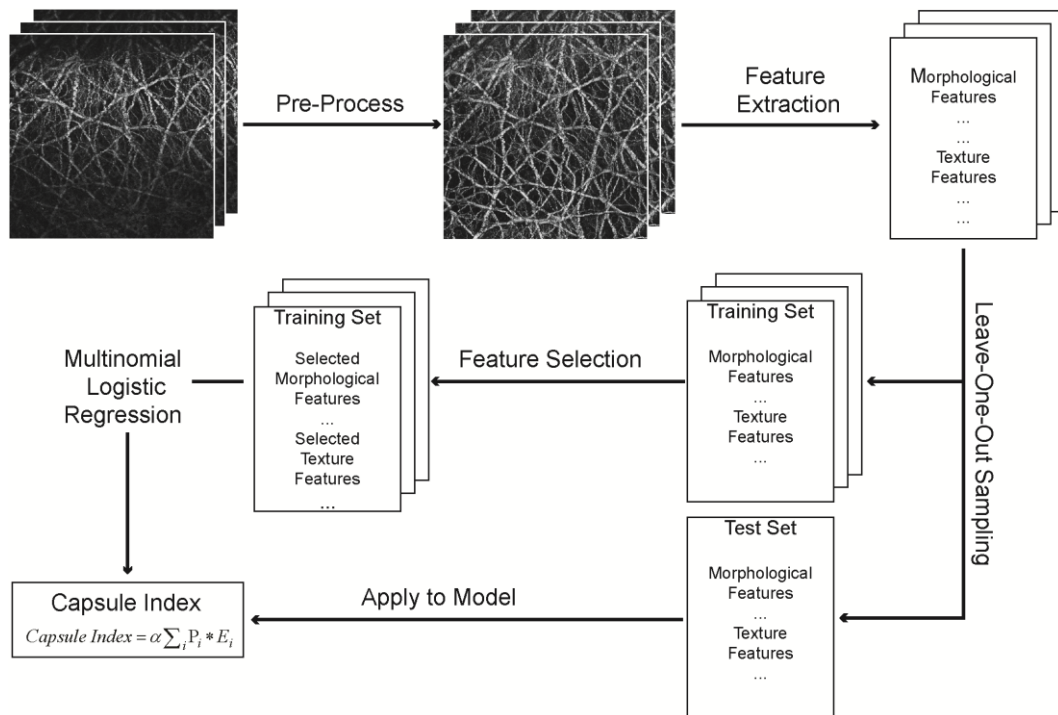
Figure 32: Schematic illustration of the procedures to create capsule index. Most significant parameters were selected from all the morphological and texture features extracted from the pre-processed capsule image to build a multinomial logistic regression model, which was used to create capsule index.

Each image stack of a site on the anterior surface of the sample was first rotated and the maximum intensity projection (MIP) [205] was performed along the z-direction to

generate a two-dimensional (2D) image which is a good representation of the Glisson's capsule in the original image stack, in order to save computation time and cost in further processing. The 2D capsule image was then segmented and 125 features were extracted, followed by feature selection to identify the most significant measurements for monitoring fibrosis progression. A leave-one-out cross-validation approach was adopted, where one sample was used as the test set to calculate capsule index while all other samples were used for training. MNL model [206] was used for the training set with selected features to predict the probabilities of all the stages from 0 to 4 for the test sample. MNL is a generalization of normal logistic regression by allowing more than two discrete outcomes that were appropriate, as we need to classify each image into one of the five stages. We then combined the probabilities of each stage for the test sample into the capsule index by the equation as follows:

$$Capsule\,Index = \alpha \sum_i p_i * E_i, i = 0,1,2,3,4 \,,$$

where p_i is the probability of stage i, $E_i = i$ is the expectation value of each stage i and α is a scale factor to normalize the capsule index into certain range. α was set to 0.25 in our study so that the capsule index is a continuous measurement ranging from 0 to 1.

4.3 Results

4.3.1 Reflective SHG reveals collagen architectures of the Glisson's capsule

TPEF/SHG microscopy on unstained samples is a good substitute for conventional histological imaging of liver fibrosis where most of the important features used in scoring system can be observed [92, 188]. A Masson Trichrome (MT) stained image of a normal liver which contains minimal collagen within portal tracts and around central veins is shown in **Figure 33A**. Similar collagen patterns were observed in the

TPEF/SHG image of the same location (**Figure 33B**). In a late stage fibrotic liver of TAA model, the collagen patterns changed significantly where broad complete septa are formed between portal areas, and between portal areas and central veins. These changes can be clearly identified in both MT stained (**Figure 33D**) and TPEF/SHG images (**Figure 33E**). The proliferation of bile duct cells is obvious in the late stage fibrotic liver of BDL model and collagens are found to aggregate around bile duct cells as shown in the MT stained image (**Figure 33G**) as well as TPEF/SHG image (**Figure 33H**).

None of the pathological features related to the cellular and collagen structures in the interior of the liver showed up in the Glisson's capsule as the outermost layer of the liver. Reflective SHG microscopy used to scan the front surface of the livers from TAA and BDL models successfully revealed collagen network architectures of the Glisson's capsule. In the capsule layer of the normal liver (**Figure 33C**), capsule collagen fibers or fibrous bundles are dense with wavy sub-filament structures. In fibrotic liver of TAA model (**Figure 33F**), the capsule collagen fibers or fibrous bundles are denser than that of the normal liver and the spaces in between the fibers or bundles are smaller. However, the capsule collagen fibers or fibrous bundles are less dense in fibrotic liver of BDL model (**Figure 33I**). The fibers are straight with loss of curry sub-filament structures and spaces between the fiber bundles are larger than the normal liver. These structural changes are likely due to the dramatic alteration of liver mechanical properties because of increased extracellular matrix (ECM) deposition and portal hypertension, which in turn affect the cellular and tissue functions or structures [207, 208]. The different progression patterns of the capsule collagen network architecture between the two animal models may be related to the different etiologies of the diseases. One possible explanation is that the accumulation of bile in

the liver in the BDL model causes the livers from the BDL model to be much larger in volume [209] (measured to be 4.1 cm^3 - 9.4 cm^3) than those from the TAA model [210] (measured to be 4.1 cm^3 - 1.9 cm^3). The decrease of volume in the TAA model is due to the loss of hepatocytes in the course of ECM accumulation. This leads to higher expansion force in the fibrotic liver of the BDL model, both on the surface and the interior causing straight fibers and large space between fibers of the Glisson's capsule.
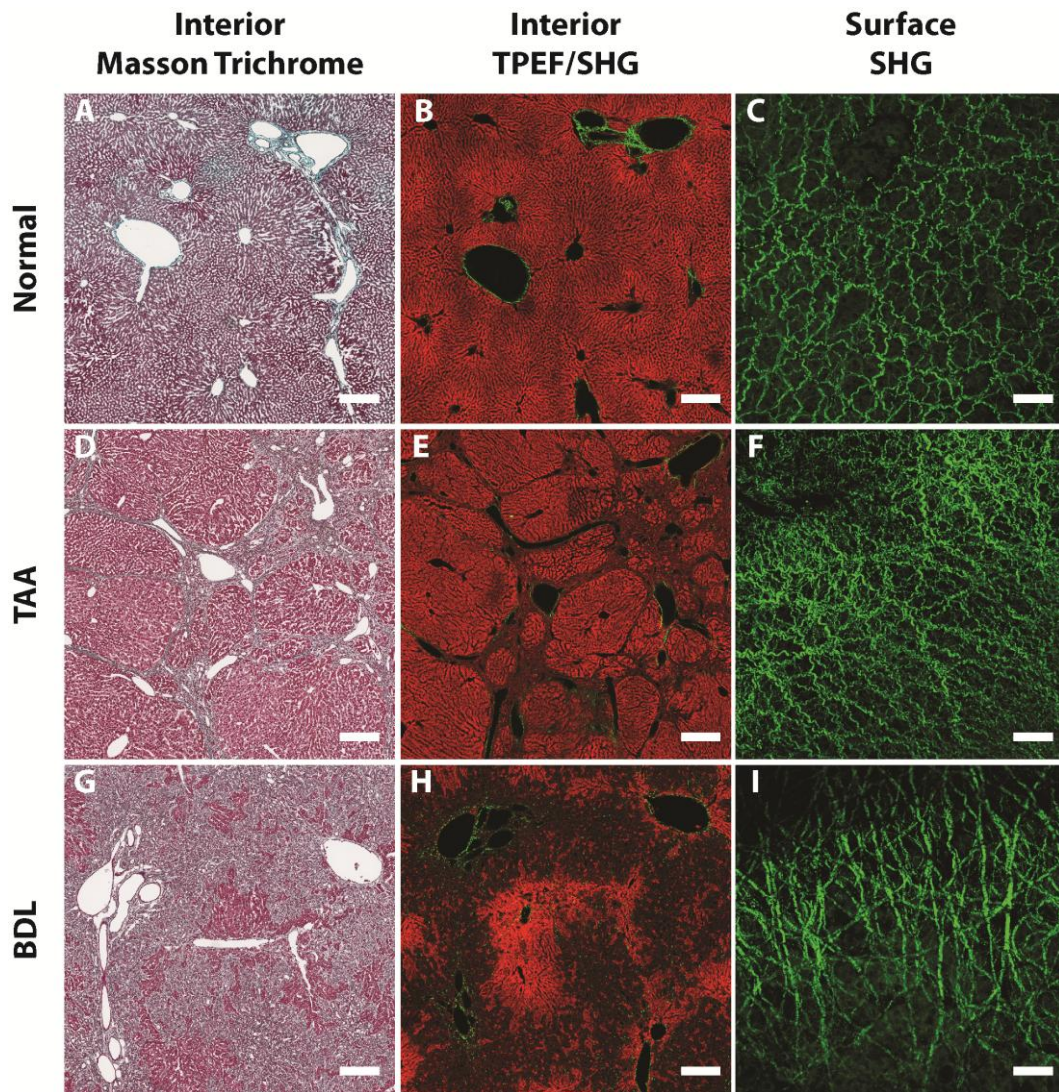
Figure 33: Comparisons between liver interior images and liver surface images. (A) to (C) are Masson Trichrome stained interior image, TPEF/SHG interior image and SHG surface image from a normal liver respectively. (D) to (F) are interior and surface images from a late stage fibrotic liver of the TAA model. (G) to (I) are interior

and surface images from a late stage fibrotic liver of the BDL model. The scale bar represents 100 um for interior images and 50um for surface images.

The capsule images of the normal and fibrotic livers from two animal models were shown at different imaging depth from 0 to 16 μm in **Figure 34**. The morphology of collagen network is consistent in the images at different depth. Thus, the 2D image generated by MIP from the z-stack image is well representative of the entire collagen network of the Glisson's capsule and is valid for additional quantification.
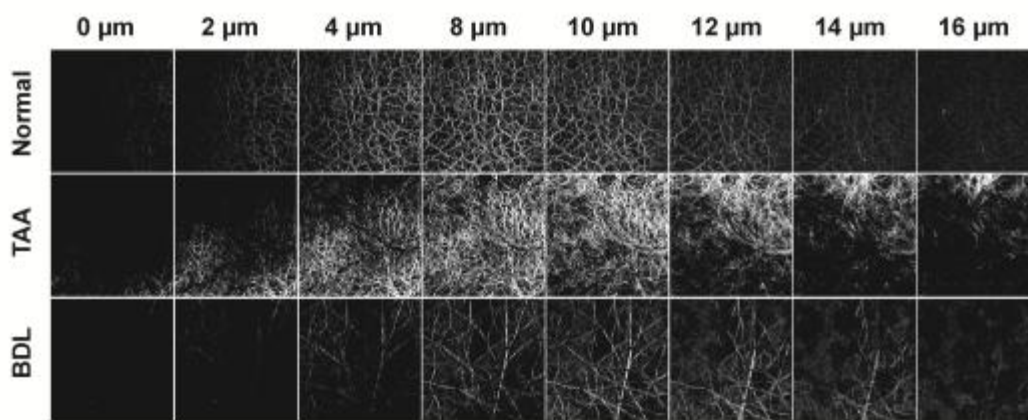
Figure 34: Illustration of SHG images at different imaging depth from the top of the Glisson's capsule. The morphology and structure of collagen network are consistent at different imaging depth.

4.3.2 Quantitative assessment of liver fibrosis from liver surface

4.3.2.1 Improved characterization of capsule morphology

The existing algorithms to extract collagen network morphology are mostly developed for biopolymer network created in collagen gels which is normally imaged using confocal microscopy with a relatively more clear background and higher signal-to-noise level. While the reflective SHG images of the collagen network from liver capsule are usually noisier, we proposed a modified fiber tracking algorithm which

tends to retain more accurate morphology of the collagen network when the image quality is not ideal and the noise level is high.

To evaluate the performance of the proposed fiber tracking method compared to one of the widely used existing method, FIRE [114], a series of artificial collagen network images were generated for testing. We simulated the artificial collagen network with different fiber numbers at 25, 50, 100 and 200. For each fiber number, 50 images were generated and noises at three different levels were added to each image. The examples of the images from the artificial collagen network with different fiber numbers at different noise level were shown in **Figure 35**.
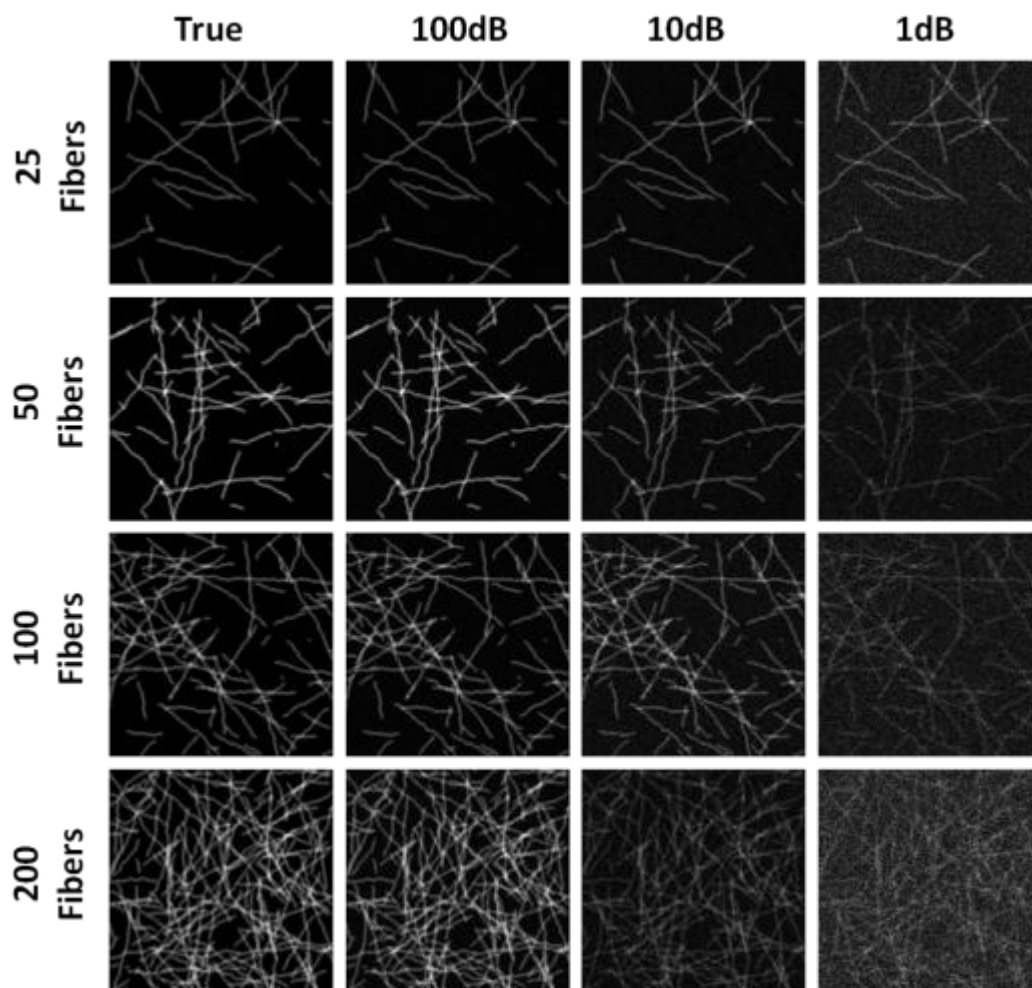
Figure 35: Simulated artificial collagen networks with different fiber numbers at different SNR level.

We chose average fiber length and average cross-link space as two representative features to evaluate the performances of proposed method. The Kolmogorov-Smirnov test was performed to compare the distribution of quantified average fiber length/cross-link spaces with the known ground-truth from each image and the K-S distance was calculated. The histograms of the K-S distance from 50 images with different fiber numbers at different signal-to-noise ratios (SNRs) were shown in **Figure 36 and 37**.

We first assessed the performance of fiber length quantification (**Figure 36**). When the number of fibers in the network is low (25 fibers), the proposed method presents similar results as the FIRE method at all noise levels. When the fiber numbers increases (50 fibers and 100 fibers), the proposed method started to show the superiority over the FIRE method with smaller K-S distances to the ground-truth, especially when the SNR is low (1dB). In the scenario of very dense collagen network (200 fibers) which is similar to the network at liver capsule, the proposed method achieved significantly better results than FIRE method even when the SNR is high (100dB). The improvements were more obvious in the images with decreased SNR (10dB, 1dB).
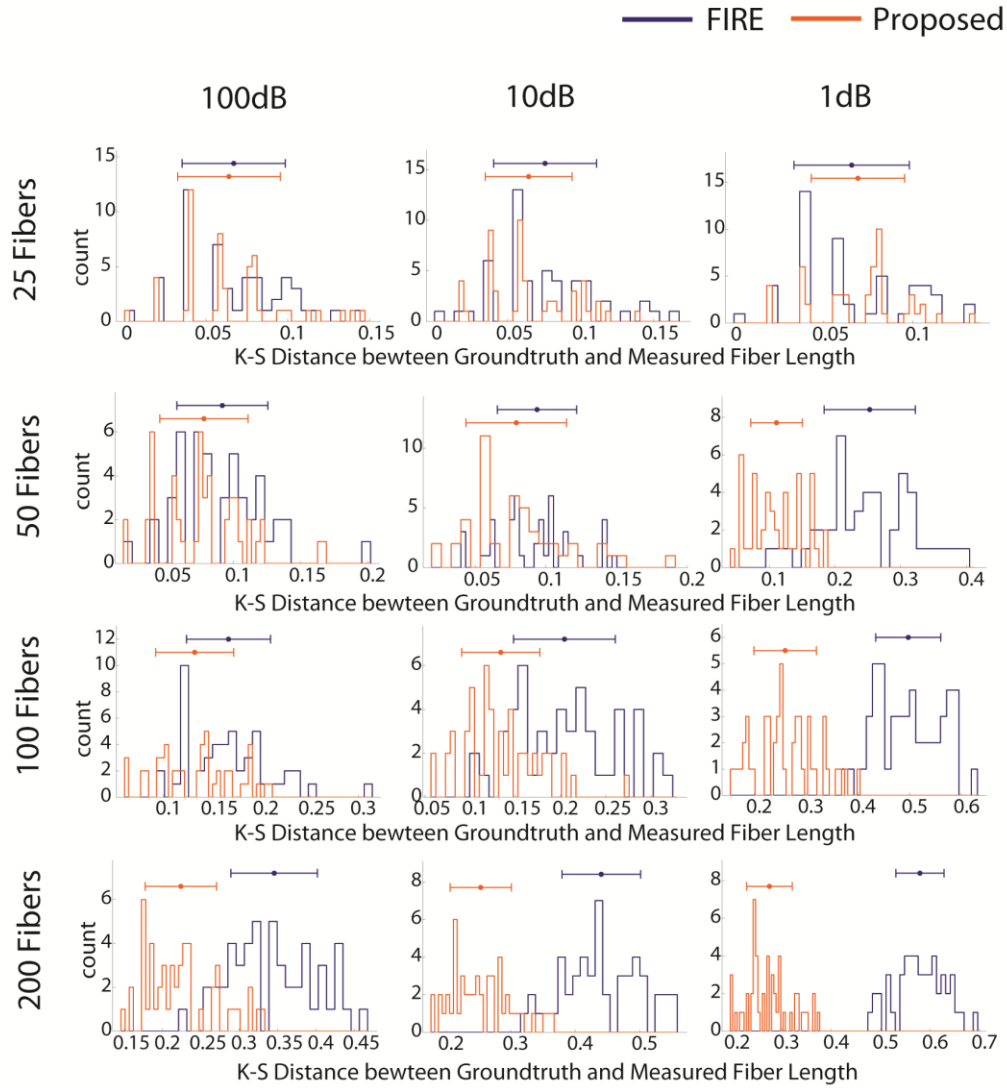
Figure 36: Assessment of the performance of fiber length quantification using proposed algorithm and FIRE method in artificial collagen network images with different fiber numbers and different SNRs.

Similar results were found when we evaluated the cross-link spaces (**Figure 37**). In the sparse collagen networks (25, 50, 100 fibers), the proposed method has smaller K-S distance than FIRE method, and the improvement is more significant when the SNR is low (1dB). When the fiber number increases to 200, the proposed method performs better than FIRE method regardless of SNR levels.
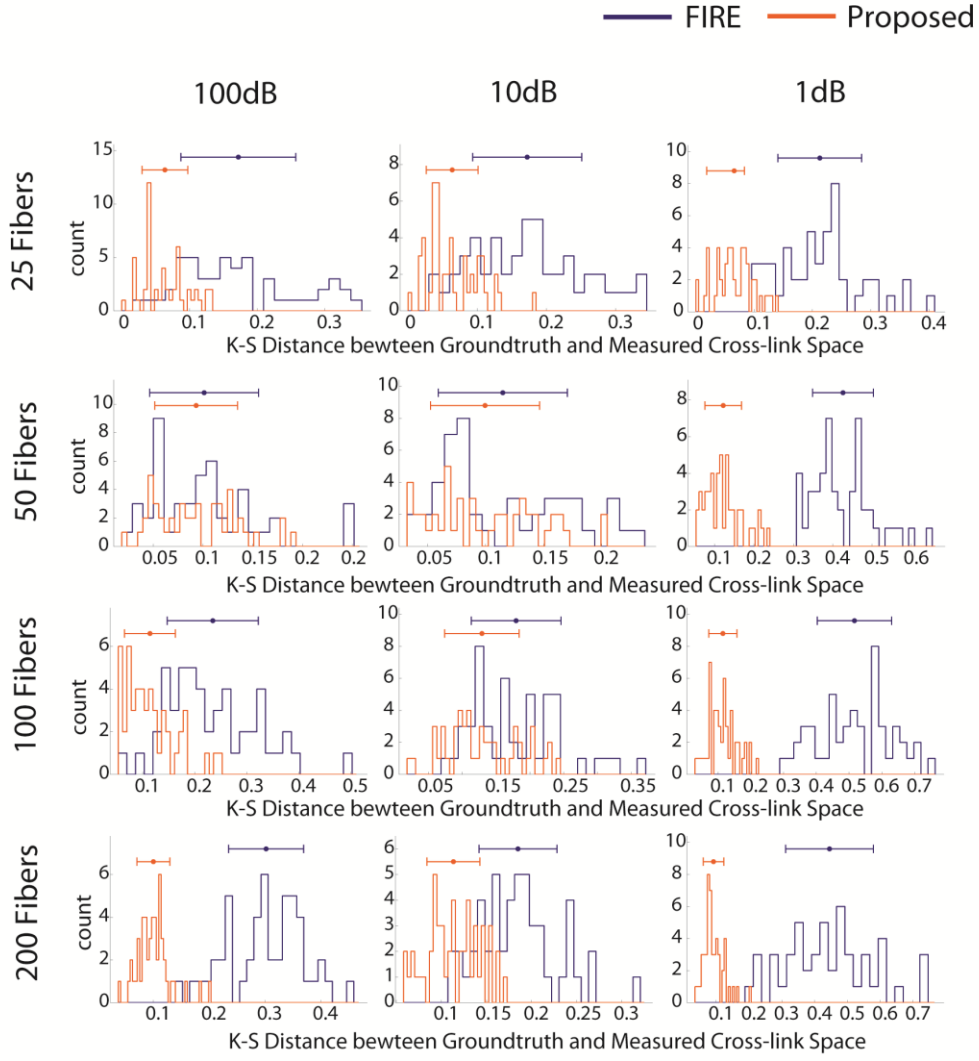
Figure 37: Assessment of the performance of cross-link spaces quantification using proposed algorithm and FIRE method in artificial collagen network images with different fiber numbers and different SNRs.

With the proposed method, we were able to better characterize the morphology of the collagen network from the liver surface, thus the features extracted would be more useful for the following analysis to generate the Capsule Index.

4.3.2.2 Capsule Index could accurately reflect fibrosis progression

The Capsule index values of the BDL and TAA rat models samples at different Metavir stages are shown in **Figure 38**. The Metavir scores were assigned by an experienced pathologist from reading the MT stained slices of the interior of the same liver of which the surface was scanned. We also presented the capsule thickness and collagen proportionate area (CPA) quantified from the capsule images at different fibrosis stages for the comparison.

In the BDL model, capsule index was observed to increase with the fibrosis progression (**Figure 38A**). One-way analysis of variance (ANOVA) revealed that there are significant differences of the average capsule index between at least two stages. Further pair-wise comparison of the mean value of capsule index between every two stages showed the significant difference between all the groups. However, no increasing trend was observed for capsule thickness with fibrosis progression as the capsule thickness decreased first in early stages and increased later in mild and late stages. No statistical significance between stage 1, stage 2 and stage 3 was found for capsule thickness (**Figure 38B**). The CPA decreases along the fibrosis progression (**Figure 38C**) due to the expansion of collagen network in the late stages in the BDL model. However, the differences were not significant between stage 2, stage 3 and stage 4.

Similar results were obtained from the TAA model, as an increasing trend of the capsule index could be observed with fibrosis progression (**Figure 38D**). One-way ANOVA indicated that the means of the capsule index of each stage were not all equal (p<0.0001). Further analysis revealed that the capsule index could differentiate between all fibrosis stages. On the other hand, capsule thickness decreased until stage 3 and a sharp increase was observed in the late stage. No significant differences were

found between stages from 0 to 3 in the TAA model for capsule thickness (**Figure 38E**). No trend was observed for CPA along the fibrosis progression (**Figure 38F**).
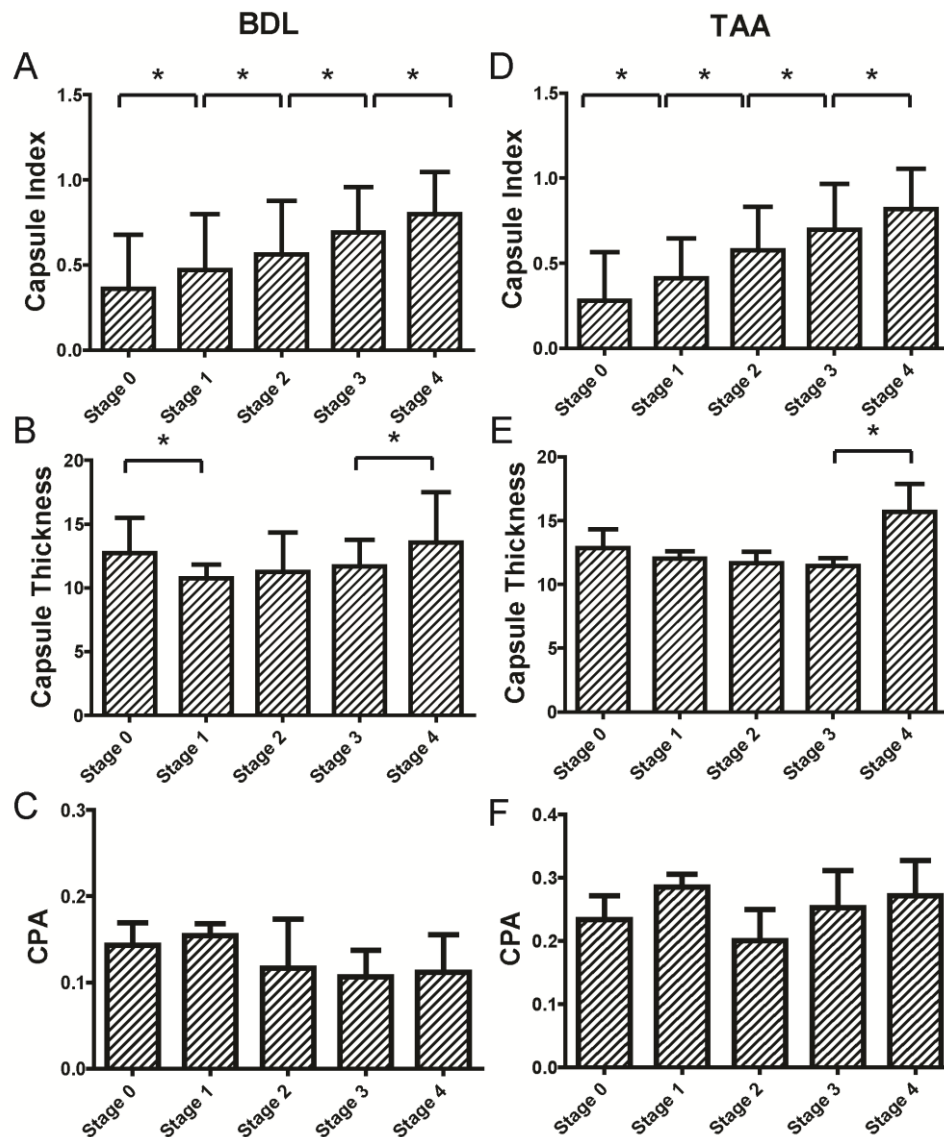
Figure 38: Validation of capsule index with conventional histopathology scoring system for bile duct ligation (BDL) and thioacetamide (TAA) model. Comparison between scoring results from conventional histo-pathological scoring system against capsule index were shown in (A) for the BDL model and (D) for the TAA model. (B) and (E) show the capsule thickness of the BDL and the TAA model for different stages. (C) and (F) show the collagen proportionate area (CPA) of the BDL and the TAA model for different fibrosis stages.

These results showed that the conventional quantification of the Glisson's capsule by measuring capsule thickness was not sufficient to accurately monitor fibrosis

progression. CPA was useful to quantify fibrosis progression in the liver interior [92]; however, it is not a good indicator for liver fibrosis assessment from the surface.

4.3.2.3 Capsule Index could detect liver fibrosis at different stages

The performances of capsule index for detection of fibrosis at different stages were evaluated with receiver operating characteristics curve (ROC) analysis. The larger area under the ROC curve (AUC) indicates the better sensitivity and specificity for the detection of certain stages. The AUC of 0.5 represents a random classification.

For the detection of fibrotic samples against normal samples (stage 0 versus. stages 1-4,), the AUCs of capsule index was 0.72 and 0.80 for the BDL and TAA model, respectively, and were significantly higher than 0.5 (**Figure 39A, D**, *p*<0.001). The AUCs of capsule thickness and CPA were 0.59 and 0.52 for the BDL model and 0.53 and 0.65 for the TAA model. Since these AUCs were not significantly higher than 0.5, both capsule thickness and CPA failed to differentiate between normal and fibrotic samples.

The detection of significant fibrosis (stages 2-4) versus non-significant fibrosis (stages 0-1) is critical for assessing the need of antiviral therapies [211]. Capsule index achieved AUCs at 0.76 and 0.84 for detection of significant fibrosis in the BDL and TAA models (**Figure 39B,E**). The best cuff-off value was 0.51 for BDL model with 69.2% sensitivity and 75.0% specificity, and was 0.52 for TAA model with 81.8% sensitivity and 71.4% specificity. The AUCs of capsule thickness and CPA were smaller (0.52-0.69).

The detection of cirrhosis (stage 4) versus non-cirrhosis (stages 0-3) is also an important indication for the end stage of fibrosis progression which has the higher risk of developing liver cancer such as hepatocellular carcinoma [211]. The AUCs of

capsule index were 0.77 and 0.91 for the detection of cirrhosis in two animal models (**Figure 39C,F**). The best cuff-off value was 0.59 for the BDL model with 72.0% sensitivity and 83.3% specificity, and was 0.62 for the TAA model with 90.9% sensitivity and 90.0% specificity. The capsule thickness can detect cirrhosis well in the TAA model with the AUC at 0.88, but cannot achieve comparable performance in the BDL model (AUC=0.61). The performance of CPA was as not good as the capsule index in both of the animal models with lower AUCs (0.60-0.69).
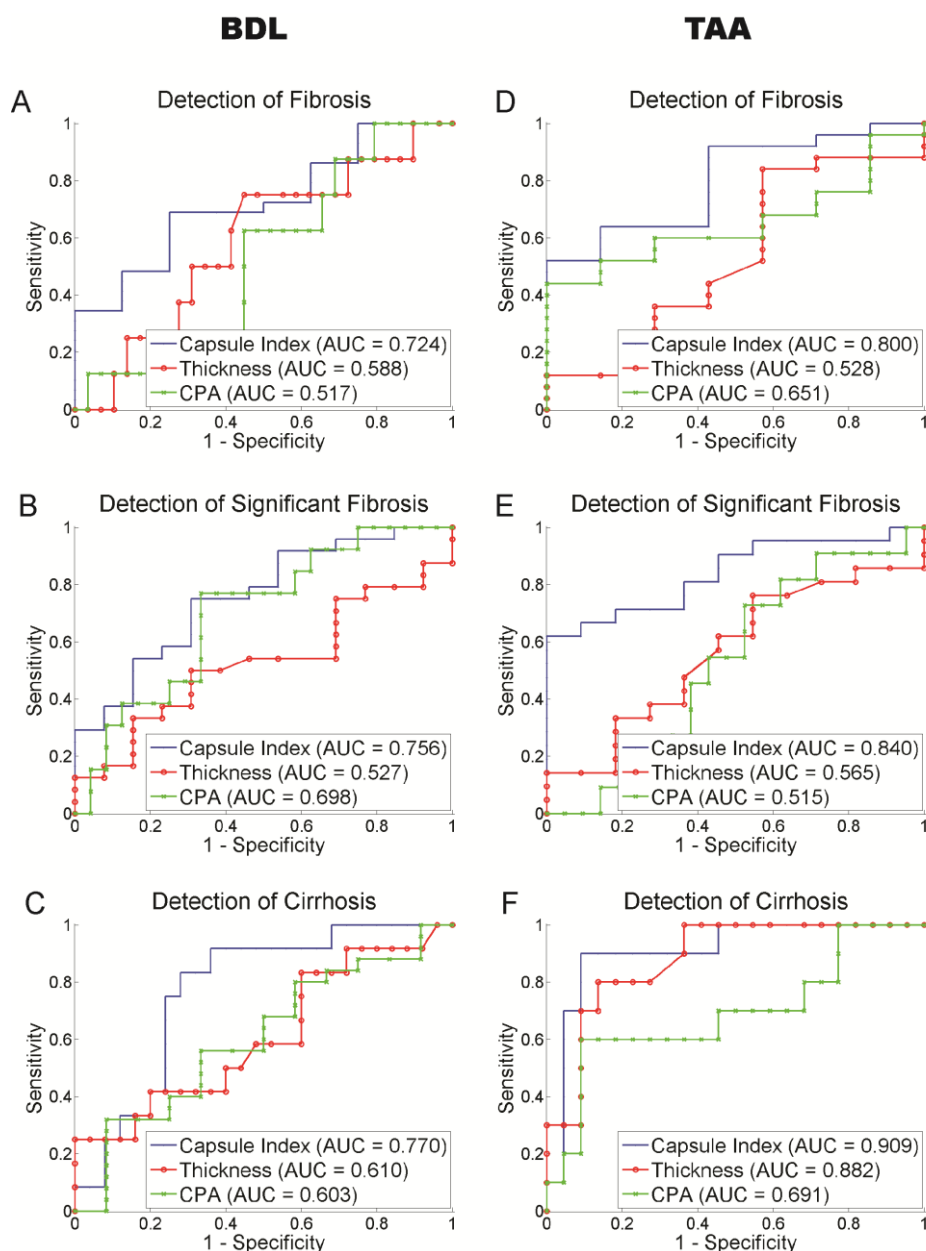
Figure 39: Receiver operating characteristics curve (ROC) analysis of capsule index to demonstrate performance for fibrosis detection at different stages. For the detection of fibrosis (stage 0 versus stages 1-4), significant fibrosis (stages 0-1 versus stages 2-4) and cirrhosis (stages 0-3 versus stage 4), capsule index performs better than capsule thickness and collagen proportionate area (CPA) in both BDL and TAA models, with area under ROC (AUC) from 0.72 to 0.91.

Thus, the capsule index can monitor the liver fibrosis progression in both TAA and BDL animal models, and can detect liver fibrosis at different stages with reasonable sensitivity and specificity. The superiority of the capsule index over the capsule

thickness and CPA for fibrosis staging comes from the detailed collagen network structure imaged by reflective SHG microscopy and quantified by our image analysis algorithm. Capsule collagen structures are highly correlated with the fibrosis progression.

4.4 Discussions

The TAA animal model has similar characteristics as viral hepatitis in humans [144], such as hepatitis B and C which are the leading and important targets for fibrosis assessment in chronic liver diseases (CLDs). The good performance of capsule index to detect different fibrosis stages in the TAA model (AUC: 0.80-0.91) showed that it is a useful marker for prognosis of fibrosis progression and regression for treatment evaluation in CLDs. The performance of capsule index to detect different fibrosis stages in the BDL model (AUC: 0.72-0.77) was not as good as in TAA model and the capsule index needs to be further improved. We have previously demonstrated the correlation of sub-capsular features to the interior liver features and the correlation of sub-capsular features to fibrosis stages in the BDL model [180]. Hence, it would be beneficial to further investigate the sub-capsular collagen and cellular information beneath the Glisson's capsule to improve the sensitivity and specificity of the capsule index for the detection of liver fibrosis at different stages.

Due to the different etiology of the two animal models we studied, the architecture changes of the capsule collagen network along fibrosis progression for the two models are different. Although similar trends of capsule index for the two animal models were found, the frequency of each feature to be selected in each training set varied. The important features should have higher frequencies since they tend to be selected more often no matter how the training set changes. The frequency of the features selected from all measurements to build the regression model in the BDL and TAA

models were shown in **Figure 40**. The importance of each feature was found to be different in the two animal models. For example, the average area of the pore space (no. 3) in the collagen network was selected in 84% of the training sets in the TAA model but was only selected in 2.7% of the training sets in the BDL model. In contrast, the average cross-link space (no. 12) was selected in the 83.8% of the training sets in the BDL model but was only selected in 12.5% of the training sets in the TAA model. Thus, it is important to fine-tune capsule index in liver diseases of different etiologies by building the specific multinomial logistic regression model for each disease with proper training set of capsule images. One advantage of the proposed framework to calculate capsule index in this study is that the rule of combination of various features to create the index was automatically learned from the training set using the pathology scores as the ground-truth.
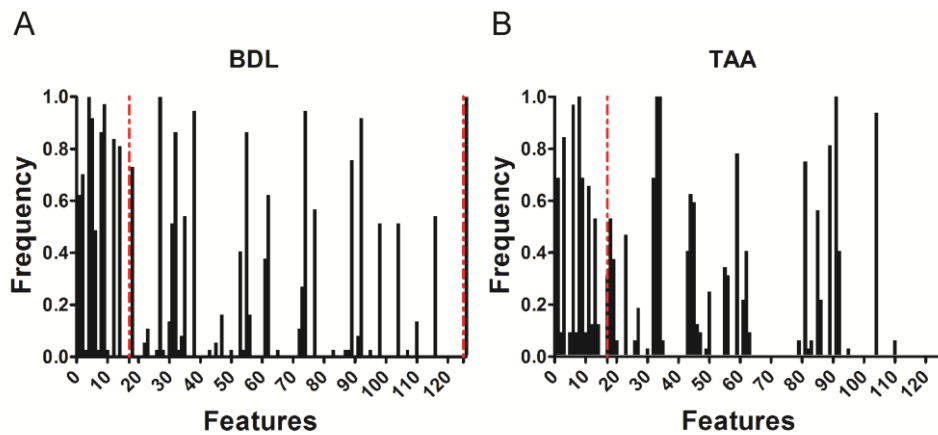
Figure 40: Comparison of the selected features between TAA and BDL models. The frequency of each feature to be selected in each training set varies between TAA and BDL model which are shown in (A) and (B). The first 16 features are morphological and structural features (left side of the first red line). The next 108 features are texture features (between the two red lines), and the final one is capsule thickness, which is the only 3D feature used.

Translation of the TPEF/SHG microscopy into potential clinical applications *in vivo* requires the establishment of minimally invasive diagnostic imaging tools. Recent studies have reported the development of nonlinear endoscopy technology and their

applications for imaging in different organs, such as kidney, liver, lung, colon and cervix [212-217]. Nonlinear endoscope is capable of acquiring images with distinct features that are similar in the images acquired by conventional nonlinear microscope. Two liver species used in this study were imaged by a SHG endoscope ex vivo (**Figure 41**). Similar collagen networks were observed in liver capsule as seen from SHG microscope, which reveals the feasibility of applying the quantification methods presented in this study to the endoscopy images. Hence, we foresee that similar collagen network images can be acquired for the Glisson's capsule by SHG endoscopes that would yield a similar framework to quantify capsule index to differentiate different stages of liver fibrosis for scoring. It should be noted that endoscopy is still a minimal invasive procedure thus its potential application needs to be further investigated. Another necessary study is to address some of the critical issues in real practice, such as the minimized number of focal spots to be imaged using the endoscopy to achieve the satisfied performance from the analysis.
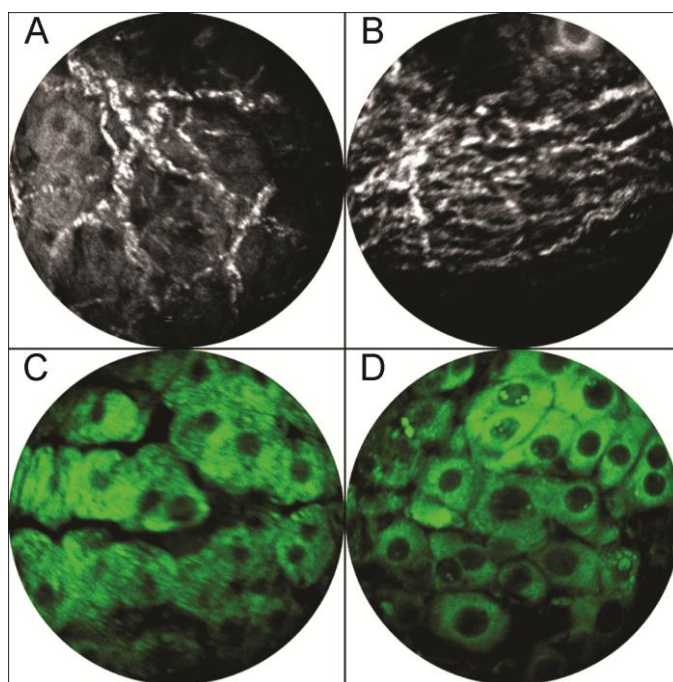
Figure 41: The *ex vivo* SHG/TPEF imaging of liver surface using non-linear endoscopy.

4.5 Conclusions

We proposed and validated a quantification system, capsule index, for liver fibrosis assessment from liver surface reflective SHG imaging. We demonstrated the advantage of imaging the Glisson's capsule using reflective SHG, which can accurately reveal the architecture of liver capsule collagen network. Image analysis methods were developed to extract plenary morphology, structure and texture features from capsule collagen network. We also presented a statistical framework to select the most important measurements from all the extracted features and to combine the selected measurements into one index. Capsule index values were compared with a conventional histopathology scoring system for two different animal models, and good correlations were established in both models. The results indicate that capsule index was able to differentiate different fibrosis stages with good performances for both animal models representing two major types of the human chronic liver diseases [190, 191]. By incorporating our capsule index quantification methodology with SHG endomicroscopy, we have established the feasibility of liver fibrosis staging and diagnosis from scanning the liver surface in a less invasive manner. This would also provide us the potential to image a larger sampling area than from biopsy and extract enough information, over many time-points for a long period of time, for liver fibrosis monitoring without the complication brought forth by the current gold standard of the invasive liver biopsy. Thus, liver surface scanning with SHG endomicroscopy could possibly replace liver biopsy in the clinical practice for the sole purpose of fibrosis assessment critical in making clinical decisions on many chronic liver diseases.

Chapter 5

Conclusion and future directions

5.1 Conclusion

The role of liver biopsy as well as the biopsy-based conventional histopathological assessment as the standard for the liver disease diagnosis is being challenged at this time. However, the alternative non-invasive diagnosis tools are still far from mature and cannot completely replace biopsy and histopathological assessment in the foreseeable future. Hence, this thesis focused on the solutions to improve the current practice of histopathological assessment using biopsy samples.

The non-linear optics microscopy especially the SHG was well known for its advantage of applicability on non-stained samples and, therefore, was selected to solve the staining variation problem. The objective assessment tools such as the automated image analysis systems are also important to assist pathologists in fibrosis scoring which could effectively minimize the inter- and intra-observer variations. By translating the qualitative pathological knowledge into the quantitative computer measurements, we build a powerful system, *q*Fibrosis, which is capable of intelligently learning from the most experienced hepato-pathologists for liver fibrosis scoring. As the pathological-relevant information is incorporated into the feature extraction and machine learning procedure, the *q*Fibrosis method is able to deliver more consistent fibrosis scores especially for early and mid stage diagnosis compared to other existing methods, given those scores from pathologists as the reference. More importantly, *q*Fibrosis not only could serve as a powerful complementary tool to

assist pathologist in fibrosis scoring, but are also suitable in many applications where a fully quantitative and unbiased "gold standard" is required. These applications include evaluation of incremental treatment efficacies for anti-fibrotic drug development and validation of newly-developed fibrosis assessment tools.

Although the *q*Fibrosis method could significantly improve the practice of biopsy-based liver fibrosis assessment, it cannot address the problem that biopsy is an invasive procedure as the *q*Fibrosis analysis is based on extracted tissue samples. Hence, we explore the possibility of using non-linear endoscope as the new image modality to assessment liver fibrosis from liver surface which could be less invasive than biopsy but still present enough tissue information at the cellular level. Due to the fact that the surface scanning using the endoscope can only penetrate around hundreds of microns from the liver surface, this thesis documented the very first study to investigate the performance of liver fibrosis diagnosis based on liver capsule at the surface only. The positive results from two animal fibrosis models supported our assumption that liver surface scanning using a non-linear endoscope could be a promising tool for less invasive liver fibrosis assessment in the future.

5.2 Future directions

The development of CAD tools coupled with non-linear optics microscopy could benefit both basic research and clinical management of liver diseases. The quantitative tools proposed in this thesis, mainly *q*Fibrosis and Capsule Index, are just two examples which require further improvement and validation in different applications with large samples sizes. The explorations of some directions with available preliminary results are elaborated as below.

5.2.1 Application of *q*Fibrosis in other liver diseases

With the burgeoning obesity-related problems across the globe, an increasing populace is suffering from the metabolic syndrome. This systemic condition has a liver component called non-alcoholic fatty liver disease (NAFLD) which is recognized as the leading cause of many liver diseases. Among the spectrum of diseases encompassed in NAFLD, diagnosis of non-alcoholic steatohepatitis (NASH) from simple hepatic steatosis is critical in clinical management, as patients with NASH have much higher risk to progress to cirrhosis which will finally lead to portal hypertension and liver cancer. The semi-quantitative scoring systems for NASH include Brunt's score and NAFLD activity score (NAS) which mainly assess the histological features of NASH from three categories: steatosis, inflammation and fibrosis. As NASH is associated with pericellular/perisinusoidal fibrosis, which is specifically denoted as fibrillar index in *q*Fibrosis, we foresee *q*Fibrosis a useful tool to quantitatively assess fibrosis changes from steatosis to NASH.

5.2.2 Go beyond fibrosis in liver disease assessment

Moreover, we have reported the successful implementation of coherent anti-Stokes Raman scattering (CARS) microscopy for liver steatosis assessment in an animal model [218]. Hence, the monitoring of the progression of NAFLD could be achieved by the integration of SHG/TPEF with CARS microscopy. With *q*Fibrosis and new image analysis tools developed for micro- and macro- vascular steatosis quantification in CARS images and inflammatory cell identification in TPEF images, a fully quantitative standard could be established to differentiate between hepatic steatosis and NASH which would have great impact on diagnosis and treatment planning.

5.2.3 Exploring cellular information beneath the liver surface

One of the advantages of non-linear optics microscopy is its penetration depth up to hundreds of microns into the tissue. To further demonstrate the feasibility of potential application of non-linear endoscopy as virtual biopsy, which is less invasive compared to biopsy and is capable of scanning larger areas as needed to reduce sampling error, the development of image analysis tools to assess cellular information beneath the Glisson's capsule is equally important. These histological features include hepatocellular changes such as cell ballooning and necrosis, as well as portal, peri-portal and lobular inflammation.

As tissue staining is not applicable for in vivo virtual biopsy, the development of virtual staining techniques could be rather useful to identify key biological structures in the tissue such as nuclei and cell and add colors to them which are familiar to the pathologists in routine stained images. Such translation from unstained images to the stained images could assist pathologists for the more comfortable evaluation of liver images using non-linear endoscopy and thus improve the qualitative assessment of virtual liver biopsy. One promising solution for this is to adopt the stimulated Raman Scattering (SRS) microscopy which allows chemical imaging of proteins within a single nucleus [219]. Hence, the conventional histopathology could move towards a new stain-free age where real-time in vivo assessment and diagnosis is feasible.

The quantitative evaluation of cellular information in the tissue from non-linear endoscopy is also important as it could provide reproducible and un-biased measurements compared to the qualitative assessment. The nucleus and cell morphologies are important features that characterize the disease progression, but the extraction of such features relies on the accurate segmentation of nuclei and cells which is difficult in TPEF image. A recent study shows that the combination of

CARS and TPEF microscopy could lead to the successful segmentation of single cell and nucleus [220]. Third harmonic generation (THG) microscopy is also reported to provide good contrast on the cell boundary which is useful for the extraction of cellular information [221]. We have explored the usage of local image features, such as scale-invariant feature transform (SIFT) features [222], as alternatives to the morphological features extracted from TPEF image for the classification of liver fibrosis into different stages in an animal study. Under the bag-of-feature (BOF) classification scheme where a dictionary (visual vocabulary) is built by quantizing and clustering SIFT features extracted from the training images, good sensitivity could be achieved for the differentiation of advanced fibrosis from the TPEF images in the test set. Evaluation of different state-of-art image features other than SIFT, such as speeded up robust features (SURF) [223] and gradient location and orientation histogram features (GLOH), that can be used in association with the BOF strategy for the classification of TPEF images of liver fibrosis could be the next step and essentially engage the better quantitative assessment of liver fibrosis using virtual biopsy from non-linear endoscopy.

References

*1.	Bataller, R. and D.A. Brenner,* **Liver fibrosis.** *Journal of Clinical Investigation, 2005. 115(2): p. 209-218.*

*2.	Friedman, S.L.,* **Molecular regulation of hepatic fibrosis, an integrated cellular response to tissue injury.** *Journal of Biological Chemistry, 2000. 275(4): p. 2247-2250.*

*3.	Benyon, R. and J. Iredale,* **Is liver fibrosis reversible?** *Gut, 2000. 46(4): p. 443-446.*

*4.	Afdhal, N.H. and D. Nunes,* **Evaluation of liver fibrosis: a concise review.** *The American journal of gastroenterology, 2004. 99(6): p. 1160-1174.*

*5.	Castera, L. and M. Pinzani,* **Biopsy and non-invasive methods for the diagnosis of liver fibrosis: does it take two to tango?** *Gut, 2010. 59(7): p. 861-866.*

*6.	Martinez, S.M., et al.,* **Noninvasive assessment of liver fibrosis.** *Hepatology, 2011. 53(1): p. 325-335.*

*7.	Ngo, Y., et al.,* **A prospective analysis of the prognostic value of biomarkers (FibroTest) in patients with chronic hepatitis C.** *Clinical chemistry, 2006. 52(10): p. 1887-1896.*

*8.	Seto, W.-K., et al.,* **A new model using routinely available clinical parameters to predict significant liver fibrosis in chronic hepatitis B.** *PloS one, 2011. 6(8): p. e23077.*

*9.	Vallet-Pichard, A., et al.,* **FIB-4: An inexpensive and accurate marker of fibrosis in HCV infection. comparison with liver biopsy and fibrotest.** *Hepatology, 2007. 46(1): p. 32-36.*

*10.	Snyder, N., et al.,* **APRI: an easy and validated predictor of hepatic fibrosis in chronic hepatitis C.** *Journal of clinical gastroenterology, 2006. 40(6): p. 535-542.*

*11.	Fung, J., et al.,* **Correlation of liver biochemistry with liver stiffness in chronic hepatitis B and development of a predictive model for liver fibrosis.** *Liver International, 2008. 28(10): p. 1408-1416.*

*12.	Manning, D.S. and N.H. Afdhal,* **Diagnosis and quantitation of fibrosis.** *Gastroenterology, 2008. 134(6): p. 1670-1681.*

*13.	Sandrin, L., et al.,* **Transient elastography: a new noninvasive method for assessment of hepatic fibrosis.** *Ultrasound in medicine & biology, 2003. 29(12): p. 1705-1713.*

14.   Huwart, L., et al., **Magnetic resonance elastography for the noninvasive staging of liver fibrosis.** *Gastroenterology, 2008. 135(1): p. 32-40.*

15.   Yin, M., et al., **Assessment of hepatic fibrosis with magnetic resonance elastography.** *Clinical Gastroenterology and Hepatology, 2007. 5(10): p. 1207-1213. e2.*

16.   Bonekamp, S., et al., **Can imaging modalities diagnose and stage hepatic fibrosis and cirrhosis accurately?** *Journal of Hepatology, 2009. 50(1): p. 17-35.*

17.   Castéra, L., et al., **Pitfalls of liver stiffness measurement: A 5-year prospective study of 13,369 examinations.** *Hepatology, 2010. 51(3): p. 828-835.*

18.   Faria, S.C., et al., **MR imaging of liver fibrosis: current state of the art.** *Radiographics, 2009. 29(6): p. 1615-1635.*

19.   Rustogi, R., et al., **Accuracy of MR elastography and anatomic MR imaging features in the diagnosis of severe hepatic fibrosis and cirrhosis.** *Journal of Magnetic Resonance Imaging, 2012. 35(6): p. 1356-1364.*

20.   Bedossa, P., D. Dargere, and V. Paradis, **Sampling variability of liver fibrosis in chronic hepatitis C.** *Hepatology, 2003. 38(6): p. 1449-1457.*

21.   Rockey, D.C., et al., **Liver biopsy.** *Hepatology, 2009. 49(3): p. 1017-1044.*

22.   Crawford, A.R., X.Z. Lin, and J.M. Crawford, **The normal adult human liver biopsy: a quantitative reference standard.** *Hepatology, 1998. 28(2): p. 323-331.*

23.   Standish, R., et al., **An appraisal of the histopathological assessment of liver fibrosis.** *Gut, 2006. 55(4): p. 569-578.*

24.   Knodell, R., et al., **Formulation and application of a numerical scoring system for assessing histological activity in asymptomatic chronic active hepatitis.** *Hepatology, 1981. 1(5): p. 431-5.*

25.   Scheuer, P., **Classification of chronic viral hepatitis: a need for reassessment** *Journal of Hepatology, 1991. 13: p. 372-4.*

26.   Ishak, K., et al., **Histological grading and staging of chronic hepatitis.** *Journal of Hepatology, 1995. 22(6): p. 696-9.*

27.   Bedossa, P. and T. Poynard, **The METAVIR cooperative study group. An algorithm for the grading of activity in chronic hepatitis C.** *Journal of Hepatology, 1996. 24(289-93).*

28.   Piccinino, F., et al., **Complications following percutaneous liver biopsy: a multicentre retrospective study on 68 276 biopsies.** *Journal of Hepatology, 1986. 2(2): p. 165-173.*

29.   *Colloredo, G., et al.,* **Impact of liver biopsy size on histological evaluation of chronic viral hepatitis: the smaller the sample, the milder the disease.** *Journal of Hepatology, 2003. 39(2): p. 239-244.*

30.   *Schiano, T.D., et al.,* **Importance of specimen size in accurate needle liver biopsy evaluation of patients with chronic hepatitis C.** *Clinical Gastroenterology and Hepatology, 2005. 3(9): p. 930-935.*

31.   *Regev, A., et al.,* **Sampling error and intraobserver variation in liver biopsy in patients with chronic HCV infection.** *The American journal of gastroenterology, 2002. 97(10): p. 2614-2618.*

32.   *Bedossa, P., et al.,* **Intraobserver and interobserver variations in liver biopsy interpretation in patients with chronic hepatitis C. The French METAVIR Cooperative Study Group.** *Hepatology, 1994. 20(1): p. 15-20.*

33.   *Gronbaek, K., et al.,* **Interobserver variation in interpretation of serial liver biopsies from patients with chronic hepatitis C.** *Journal of Viral Hepatitis, 2002. 9(6): p. 443-449.*

34.   *Westin, J., et al.,* **Interobserver study of liver histopathology using the Ishak score in patients with chronic hepatitis C virus infection.** *Liver, 1999. 19(3): p. 183-187.*

35.   *Denk, W., J.H. Strickler, and W.W. Webb,* **Two-photon laser scanning fluorescence microscopy.** *Science, 1990. 248(4951): p. 73-76.*

36.   *Campagnola, P.J., et al.,* **Three-dimensional high-resolution second-harmonic generation imaging of endogenous structural proteins in biological tissues.** *Biophysical Journal, 2002. 82(1 Pt 1): p. 493-508.*

37.   *Han, X., et al.,* **Second harmonic properties of tumor collagen: determining the structural relationship between reactive stroma and healthy stroma.** *Optics Express, 2008. 16: p. 1846-1859.*

38.   *Lin, M.G., et al.,* **Evaluation of dermal thermal damage by multiphoton autofluorescence and second-harmonic-generation microscopy.** *Journal of Biomedical Optics, 2006. 11(6): p. 064006.*

39.   *Theodossiou, T.A., et al.,* **Second harmonic generation confocal microscopy of collagen type I from rat tendon cryosections.** *Biophysical Journal, 2006. 91(12): p. 4665-4677.*

40.   *Strupler, M., et al.,* **Second harmonic imaging and scoring of collagen in fibrotic tissues.** *Optics Express, 2007. 15(7): p. 4054-4065.*

41.   Sun, W., et al., **Nonlinear optical microscopy: use of second harmonic generation and two-photon microscopy for automated quantitative liver fibrosis studies.** *Journal of Biomedical Optics, 2008. 13(6): p. 064010-064010-7.*

42.   Cox, G., et al., **3-dimensional imaging of collagen using second harmonic generation.** *Journal of Structural Biology, 2003. 141(1): p. 53-62.*

43.   Lee, H.S., et al., **Optical biopsy of liver fibrosis by use of multiphoton microscopy.** *Optics Letter, 2004. 29(22): p. 2614-6.*

44.   Yeh, A.T., et al., **Reversible dissociation of collagen in tissues.** *Journal of Investigative Dermatology, 2003. 121(6): p. 1332-1335.*

45.   Tai, S.-P., et al., **Optical biopsy of fixed human skin with backward-collected optical harmonics signals.** *Optics Express, 2005. 13(20): p. 8231-8242.*

46.   Lin, S.-J., et al., **Discrimination of basal cell carcinoma from normal dermal stroma by quantitative multiphoton imaging.** *Optics letters, 2006. 31(18): p. 2756-2758.*

47.   Su, P.-J., et al. **Discrimination of collagen in normal and pathological dermis through polarization second harmonic generation.** *in* **Proceedings of SPIE.** *2010.*

48.   Cicchi, R., et al., **Scoring of collagen organization in healthy and diseased human dermis by multiphoton microscopy.** *Journal of biophotonics, 2010. 3(1-2): p. 34-43.*

49.   Medyukhina, A., et al., **Automated classification of healthy and keloidal collagen patterns based on processing of SHG images of human skin.** *Journal of biophotonics, 2011. 4(9): p. 627-636.*

50.   Wu, S., et al., **Quantitative analysis on collagen morphology in aging skin based on multiphoton microscopy.** *Journal of Biomedical Optics, 2011. 16(4): p. 040502-040502-3.*

51.   Puschmann, S., et al., **Approach to quantify human dermal skin aging using multiphoton laser scanning microscopy.** *Journal of Biomedical Optics, 2012. 17(3): p. 0360051-0360056.*

52.   Chen, J., et al., **Multiphoton microscopy study of the morphological and quantity changes of collagen and elastic fiber components in keloid disease.** *Journal of Biomedical Optics, 2011. 16(5): p. 051305-051305-6.*

53.   Yeh, A.T., et al., **Selective corneal imaging using combined second-harmonic generation and two-photon excited fluorescence.** *Optics letters, 2002. 27(23): p. 2082-2084.*

54.   Han, M., G. Giese, and J. Bille, Second harmonic generation imaging of collagen fibrils in cornea and sclera. *Optics Express, 2005. 13(15): p. 5791-5797.*

55.   Tan, H.-Y., et al., Multiphoton fluorescence and second harmonic generation microscopy for imaging infectious keratitis. *Journal of Biomedical Optics, 2007. 12(2): p. 024013-024013-8.*

56.   Matteini, P., et al. Quantitative analysis of thermally-induced alterations of corneal stroma by second-harmonic generation imaging. *in BiOS. 2010. International Society for Optics and Photonics.*

57.   Provenzano, P.P., et al., Collagen density promotes mammary tumor initiation and progression. *BMC medicine, 2008. 6(1): p. 11.*

58.   Provenzano, P.P., et al., Collagen reorganization at the tumor-stromal interface facilitates local invasion. *BMC medicine, 2006. 4(1): p. 1-15.*

59.   Conklin, M.W., et al., Aligned collagen is a prognostic signature for survival in human breast carcinoma. *The American journal of pathology, 2011. 178(3): p. 1221-1232.*

60.   Adur, J., et al., Recognition of serous ovarian tumors in human samples by multimodal nonlinear optical microscopy. *Journal of Biomedical Optics, 2011. 16(9): p. 096017-096017-10.*

61.   Kirkpatrick, N.D., M.A. Brewer, and U. Utzinger, Endogenous optical biomarkers of ovarian cancer evaluated with multiphoton microscopy. *Cancer Epidemiology Biomarkers & Prevention, 2007. 16(10): p. 2048-2057.*

62.   Nadiarnykh, O., et al., Alterations of the extracellular matrix in ovarian cancer studied by second harmonic generation imaging microscopy. *BMC cancer, 2010. 10(1): p. 94.*

63.   Hompland, T., et al., Second-harmonic generation in collagen as a potential cancer diagnostic parameter. *Journal of Biomedical Optics, 2008. 13(5): p. 054050-054050-11.*

64.   Wang, C.-C., et al., Differentiation of normal and cancerous lung tissues by multiphoton imaging. *Journal of Biomedical Optics, 2009. 14(4): p. 044034-044034-4.*

65.   Zhang, K., et al., Bipolar cellular morphology of malignant melanoma in unstained human melanoma skin tissue. *Journal of Biomedical Optics, 2009. 14(2): p. 024042-024042-9.*

66.   Sun, T.-L., et al., Ex vivo imaging and quantification of liver fibrosis using second-harmonic generation microscopy. *Journal of Biomedical Optics, 2010. 15(3): p. 036002-036002-6.*

67.   Guilbert, T., et al., **A robust collagen scoring method for human liver fibrosis by second harmonic microscopy.** *Optics Express, 2010. 18(25): p. 25794-25807.*

68.   Pena, A.M., et al., **Three-dimensional investigation and scoring of extracellular matrix remodeling during lung fibrosis using multiphoton microscopy.** *Microscopy research and technique, 2007. 70(2): p. 162-170.*

69.   Strupler, M., et al., **Second harmonic microscopy to quantify renal interstitial fibrosis and arterial remodeling.** *Journal of Biomedical Optics, 2008. 13(5): p. 054041-054041-10.*

70.   Hu, W., et al., **Characterization of collagen fibers by means of texture analysis of second harmonic generation images using orientation-dependent gray level co-occurrence matrix method.** *Journal of Biomedical Optics, 2012. 17(2): p. 0260071-0260079.*

71.   Frisch, K.E., et al., **Quantification of collagen organization using fractal dimensions and Fourier transforms.** *Acta histochemica, 2012. 114(2): p. 140-144.*

72.   Lilledahl, M.B., et al. **Extracting quantitative biomechanical parameters for cartilage from second harmonic generation images.** *in SPIE BiOS. 2011. International Society for Optics and Photonics.*

73.   Lilledahl, M.B., et al., **Structural analysis of articular cartilage using multiphoton microscopy: input for biomechanical modeling.** *Medical Imaging, IEEE Transactions on, 2011. 30(9): p. 1635-1648.*

74.   Plotnikov, S.V., et al., **Measurement of muscle disease by quantitative second-harmonic generation imaging.** *Journal of Biomedical Optics, 2008. 13(4): p. 044018-044018-11.*

75.   Garbe, C.S., et al., **Automated multiscale morphometry of muscle disease from second harmonic generation microscopy using tensor-based image processing.** *Biomedical Engineering, IEEE Transactions on, 2012. 59(1): p. 39-44.*

76.   Zoumi, A., et al., **Imaging coronary artery microstructure using second-harmonic and two-photon fluorescence microscopy.** *Biophysical Journal, 2004. 87(4): p. 2778-2786.*

77.   Kwon, G.P., et al., **Contribution of macromolecular structure to the retention of low-density lipoprotein at arterial branch points.** *Circulation, 2008. 117(22): p. 2919-2927.*

78.   Wallace, S.J., et al., **Second-harmonic generation and two-photon-excited autofluorescence microscopy of cardiomyocytes: quantification of cell volume and myosin filaments.** *Journal of Biomedical Optics, 2008. 13(6): p. 064018-064018-5.*

79.   Tsai, M.-R., et al., Second-harmonic generation imaging of collagen fibers in myocardium for atrial fibrillation diagnosis. *Journal of Biomedical Optics, 2010. 15(2): p. 026002-026002-6.*

80.   Akins, M.L., K. Luby-Phelps, and M. Mahendroo, Second harmonic generation imaging as a potential tool for staging pregnancy and predicting preterm birth. *Journal of Biomedical Optics, 2010. 15(2): p. 026020-026020-10.*

81.   Yousefi, S., B. Kim, and N. Kehtarnavaz, AUTOMATING POROSITY FEATURES EXTRACTION FROM SECOND HARMONIC GENERATION IMAGES OF CERVICAL TISSUE.

82.   Reiser, K.M., et al., Quantitative analysis of structural disorder in intervertebral disks using second harmonic generation imaging: comparison with morphometric analysis. *Journal of Biomedical Optics, 2007. 12(6): p. 064019-064019-17.*

83.   Kage, M., et al., Long-term evolution of fibrosis from chronic hepatitis to cirrhosis in patients with hepatitis C: morphometric analysis of repeated biopsies. *Hepatology, 1997. 25(4): p. 1028-1031.*

84.   Pilette, C., et al., Histopathological evaluation of liver fibrosis: Quantitative image analysis vs semi-quantitative scores: Comparison with serum markers. *Journal of Hepatology, 1998. 28(3): p. 439-446.*

85.   O'Brien, M.J., et al., An assessment of digital image analysis to measure fibrosis in liver biopsy specimens of patients with chronic hepatitis C. *American journal of clinical pathology, 2000. 114(5): p. 712-718.*

86.   Wright, M., et al., Quantitative versus morphological assessment of liver fibrosis: semi-quantitative scores are more robust than digital image fibrosis area estimation. *Liver International, 2003. 23(1): p. 28-34.*

87.   Arima, M., et al., Regression of liver fibrosis in cases of chronic liver disease type C: quantitative evaluation by using computed image analysis. *Internal medicine, 2004. 43(10): p. 902-910.*

88.   Lazzarini, A.L., et al., Advances in digital quantification technique enhance discrimination between mild and advanced liver fibrosis in chronic hepatitis C. *Liver International, 2005. 25(6): p. 1142-1149.*

89.   Friedenberg, M.A., et al., Simplified method of hepatic fibrosis quantification: design of a new morphometric analysis application. *Liver International, 2005. 25(6): p. 1156-1161.*

90.   Goodman, Z.D., et al., Progression of fibrosis in advanced chronic hepatitis C: evaluation by morphometric image analysis. *Hepatology, 2007. 45(4): p. 886-894.*

91.   Goodman, Z.D., et al., **Fibrosis progression in chronic hepatitis C: Morphometric image analysis in the HALT-C trial.** *Hepatology, 2009. 50(6): p. 1738-1749.*

92.   Gailhouste, L., et al., **Fibrillar collagen scoring by second harmonic microscopy: a new tool in the assessment of liver fibrosis.** *Journal of hepatology, 2010. 52(3): p. 398-406.*

93.   Calvaruso, V., et al., **Computer-assisted image analysis of liver collagen: Relationship to Ishak scoring and hepatic venous pressure gradient.** *Hepatology, 2009. 49(4): p. 1236-1244.*

94.   Manousou, P., et al., **Digital image analysis of liver collagen predicts clinical outcome of recurrent hepatitis C virus 1 year after liver transplantation.** *Liver Transplantation, 2011. 17(2): p. 178-188.*

95.   Nitta, Y., et al., **Liver stiffness measured by transient elastography correlates with fibrosis area in liver biopsy in patients with chronic hepatitis C.** *Hepatology Research, 2009. 39(7): p. 675-684.*

96.   Mori, M., et al., **Close correlation of liver stiffness with collagen deposition and presence of myofibroblasts in non-alcoholic fatty liver disease.** *Hepatology Research, 2011. 41(9): p. 897-903.*

97.   Patel, K., et al., **Correlation of FIBRO< i> Spect</i> II With Histologic and Morphometric Evaluation of Liver Fibrosis in Chronic Hepatitis C.** *Clinical Gastroenterology and Hepatology, 2008. 6(2): p. 242-247.*

98.   Masseroli, M., et al., **Automatic quantification of liver fibrosis: design and validation of a new image analysis method: comparison with semi-quantitative indexes of fibrosis.** *Journal of Hepatology, 2000. 32(3): p. 453-64.*

99.   Caballero, T., et al., **Liver fibrosis assessment with semiquantitative indexes and image analysis quantification in sustained-responder and non-responder interferon-treated patients with chronic hepatitis C.** *Journal of Hepatology, 2001. 34(5): p. 740-747.*

100.   Zaitoun, A., et al., **Quantitative assessment of fibrosis and steatosis in liver biopsies from patients with chronic hepatitis C.** *Journal of clinical pathology, 2001. 54(6): p. 461-465.*

101.   Hui, A.Y., et al., **Quantitative assessment of fibrosis in liver biopsies from patients with chronic hepatitis B.** *Liver International, 2004. 24(6): p. 611-618.*

102.   Wong, G.L.H., et al., **Assessment of fibrosis by transient elastography compared with liver biopsy and morphometry in chronic liver diseases.** *Clinical Gastroenterology and Hepatology, 2008. 6(9): p. 1027-1035.*

103.   Sethasine, S., et al., **Quantitative histological-hemodynamic correlations in cirrhosis.** *Hepatology, 2012. 55(4): p. 1146-1153.*

104.   Kim, S.U., et al., **The Laennec staging system for histological sub-classification of cirrhosis is useful for stratification of prognosis in patients with liver cirrhosis.** *Journal of Hepatology, 2012. 57(3): p. 556-563.*

105.   Matalka, I.I., O.M. Al-Jarrah, and T.M. Manasrah, **Quantitative assessment of liver fibrosis: a novel automated image analysis method.** *Liver International, 2006. 26(9): p. 1054-1064.*

106.   Dioguardi, N., et al., **Liver fibrosis and tissue architectural change measurement using fractal-rectified metrics and Hurst's exponent.** *World Journal of Gastroenterology, 2006. 12(14): p. 2187.*

107.   Buschmann, R.J. and J.W. Ryoo, **Hepatic structural correlates of liver fibrosis: a morphometric analysis.** *Experimental and molecular pathology, 1989. 50(1): p. 114-124.*

108.   Ryoo, J. and R. Buschmann, **Comparison of intralobar non-parenchyma, subcapsular non-parenchyma, and liver capsule thickness.** *Journal of clinical pathology, 1989. 42(7): p. 740-744.*

109.   Chapman, G. and D. Eagles, **Ultrastructural features of Glisson's capsule and the overlying mesothelium in rat, monkey and pike liver.** *Tissue and Cell, 2007. 39(5): p. 343-351.*

110.   He, Y., et al., **Toward surface quantification of liver fibrosis progression.** *Journal of Biomedical Optics, 2010. 15(5): p. 056007-056007-11.*

111.   Lee, J.W., et al., **Hepatic Capsular and Subcapsular Pathologic Conditions: Demonstration with CT and MR Imaging1.** *Radiographics, 2008. 28(5): p. 1307-1323.*

112.   Baradet, T.C., J.C. Haselgrove, and J.W. Weisel, **Three-dimensional reconstruction of fibrin clot networks from stereoscopic intermediate voltage electron microscope images and analysis of branching.** *Biophysical Journal, 1995. 68(4): p. 1551-1560.*

113.   Wu, J., et al., **Automated quantification and reconstruction of collagen matrix from 3D confocal datasets.** *Journal of microscopy, 2003. 210(2): p. 158-165.*

114.   Stein, A.M., et al., **An algorithm for extracting the network geometry of three-dimensional collagen gels.** *Journal of microscopy, 2008. 232(3): p. 463-475.*

115.   Nisslert, R., et al., **Identification of the three-dimensional gel microstructure from transmission electron micrographs.** *Journal of microscopy, 2007. 225(1): p. 10-21.*

116.   Yang, Y.-l., L.M. Leone, and L.J. Kaufman, Elastic moduli of collagen gels can be predicted from two-dimensional confocal microscopy. *Biophysical Journal, 2009. 97(7): p. 2051-2060.*

117.   Lück, S., et al., Three-dimensional analysis of intermediate filament networks using SEM tomography. *Journal of microscopy, 2010. 239(1): p. 1-16.*

118.   Smith, M.B., et al., Segmentation and tracking of cytoskeletal filaments using open active contours. *Cytoskeleton, 2010. 67(11): p. 693-705.*

119.   Dioguardi, N., et al., Metrically measuring liver biopsy: A chronic hepatitis B and C computer-aided morphologic description. *World Journal of Gastroenterology, 2008. 14(48): p. 7335-7344.*

120.   Chen, M.H., et al., Multiphoton autofluorescence and second-harmonic generation imaging of the tooth. *Journal of Biomedical Optics, 2007. 12.*

121.   Gong, B., et al., Nonlinear imaging study of extracellular matrix in chemical-induced, developmental dissecting aortic aneurysm: Evidence for defective collagen type III. *Birth Defects Research Part a-Clinical and Molecular Teratology, 2008. 82: p. 16-24.*

122.   Gualda, E.J., et al., In vivo imaging of cellular structures in Caenorhabditis elegans by combined TPEF, SHG and THG microscopy. *Journal of Microscopy-Oxford, 2008. 229: p. 141-150.*

123.   Lyubovitsky, J.G., et al., In situ multiphoton optical tomography of hair follicles in mice. *Journal of Biomedical Optics, 2007. 12.*

124.   Odin, C., et al., Orientation fields of nonlinear biological fibrils by second harmonic generation microscopy. *Journal of Microscopy-Oxford, 2008. 229: p. 32-38.*

125.   Teisseyre, T.Z., et al., Nonlinear optical potentiometric dyes optimized for imaging with 1064-nm light. *Journal of Biomedical Optics, 2007. 12.*

126.   Yasui, T., Y. Tohno, and T. Araki, Characterization of collagen orientation in human dermis by two-dimensional second-harmonic-generation polarimetry. *Journal of Biomedical Optics, 2004. 9(2): p. 259-264.*

127.   Boigk, G., et al., Silymarin retards collagen accumulation in early and advanced biliary fibrosis secondary to complete bile duct obliteration in rats. *Hepatology, 1997. 26(3): p. 643-649*

128.   Ruwart, M.J., et al., The integrated value of serum procollagen-III peptide over time predicts hepatic hydroxyproline content and staniable collagen in a model of dietart cirrhosis in the rat *Hepatology, 1989. 10(5): p. 801-806.*

129.   Otsu, N., A threshold selection method from gray level histograms. *IEEE Trans. System, Man and Cybernetics, 1979. 9: p. 62-66.*

130.   Serra, J., Image analysis and mathematical morphology*1982, London, New York: Academic Press.*

131.   Venkatesh, S.K., M. Yin, and R.L. Ehman, Magnetic resonance elastography of liver: Technique, analysis, and clinical applications. *Journal of Magnetic Resonance Imaging, 2013. 37(3): p. 544-555.*

132.   Theodossi, A., et al., Observer variation in assessment of liver biopsies including analysis by kappa statistics. *Gastroenterology, 1980. 79(2): p. 232-41.*

133.   Theodossi, A., et al., Observer variation and discriminatory value of biopsy features in inflammatory bowel-disease. *Gut, 1994. 35(7): p. 961-968.*

134.   Poynard, T., et al., A comparison of fibrosis progression in chronic liver diseases. *Journal of Hepatology, 2003. 38(3): p. 257-265.*

135.   Organization, W.H., Hepatitis B. Fact sheet No. 204. 2008. *World Health Organization: Geneva, Switzerland, 2012.*

136.   Marcellin, P., et al., Regression of cirrhosis during treatment with tenofovir disoproxil fumarate for chronic hepatitis B: a 5-year open-label follow-up study. *The Lancet, 2012.*

137.   Rosselli, M., et al., Beyond scoring: a modern interpretation of disease progression in chronic liver disease. *Gut, 2013.*

138.   Grant, A. and J. Neuberger, Guidelines on the use of liver biopsy in clinical practice. *Gut, 1999. 45(suppl 4): p. IV1-IV11.*

139.   Saadeh, S., et al., The role of liver biopsy in chronic hepatitis C. *Hepatology, 2001. 33(1): p. 196-200.*

140.   Bedossa, P. and F. Carrat, Liver biopsy: the best, not the gold standard. *Journal of Hepatology, 2009. 50(1): p. 1-3.*

141.   Pinzani, M., et al., Technology Insight: noninvasive assessment of liver fibrosis by biochemical scores and elastography. *Nature Clinical Practice Gastroenterology & Hepatology, 2008. 5(2): p. 95-106.*

142.   Wanless, I.R., E. Nakashima, and M. Sherman, Regression of human cirrhosis: morphologic features and the genesis of incomplete septal cirrhosis. *Archives of pathology & laboratory medicine, 2000. 124(11): p. 1599-1607.*

143.   Hytiroglou, P., et al., Beyond "Cirrhosis" A Proposal From the International Liver Pathology Study Group. *American journal of clinical pathology, 2012. 137(1): p. 5-9.*

144.   *Müller, A., et al.,* **Thioacetamide-induced cirrhosis-like liver lesions in rats usefulness and reliability of this animal model.** *Experimental pathology, 1988. 34(4): p. 229-236.*

145.   *Akahoshi, T., et al.,* **Role of the spleen in liver fibrosis in rats may be mediated by transforming growth factor β-1.** *Journal of gastroenterology and hepatology, 2002. 17(1): p. 59-65.*

146.   *Dekel, R., et al.,* **Gliotoxin ameliorates development of fibrosis and cirrhosis in a thioacetamide rat model.** *Digestive diseases and sciences, 2003. 48(8): p. 1642-1647.*

147.   *Xu, L. and M.I. Jordan,* **On convergence properties of the EM algorithm for Gaussian mixtures.** *Neural computation, 1996. 8(1): p. 129-151.*

148.   *Gonzalez, R.C., R.E. Woods, and S.L. Eddins,* **Digital image processing using MATLAB.** *Vol. 2. 2009: Gatesmark Publishing Knoxville.*

149.   *Aurenhammer, F.,* **Voronoi diagrams—a survey of a fundamental geometric data structure.** *ACM Computing Surveys (CSUR), 1991. 23(3): p. 345-405.*

150.   *Greene, W.H.,* **Econometric Analysis, 5/e** *2003: Pearson Education India.*

151.   *Guyon, I., et al.,* **Gene selection for cancer classification using support vector machines.** *Machine learning, 2002. 46(1-3): p. 389-422.*

152.   *Abeel, T., et al.,* **Robust biomarker identification for cancer diagnosis with ensemble feature selection methods.** *Bioinformatics, 2010. 26(3): p. 392-398.*

153.   *Abdi, H. and L.J. Williams,* **Principal component analysis.** *Wiley Interdisciplinary Reviews: Computational Statistics, 2010. 2(4): p. 433-459.*

154.   *Williams, R.,* **Generalized ordered logit/partial proportional odds models for ordinal dependent variables.** *Stata Journal, 2006. 6(1): p. 58-82.*

155.   *Degos, F., et al.,* **Diagnostic accuracy of FibroScan and comparison to liver fibrosis biomarkers in chronic viral hepatitis: a multicenter prospective study (the FIBROSTIC study).** *Journal of Hepatology, 2010. 53(6): p. 1013-1021.*

156.   *Jin, W., et al.,* **Diagnostic accuracy of the aspartate aminotransferase-to-platelet ratio index for the prediction of hepatitis B-related fibrosis: a leading meta-analysis.** *BMC gastroenterology, 2012. 12(1): p. 14.*

157.   *Kim, B.K., et al.,* **Validation of FIB-4 and comparison with other simple noninvasive indices for predicting liver fibrosis and cirrhosis in hepatitis B virus-infected patients.** *Liver International, 2010. 30(4): p. 546-553.*

158.   *Zipfel, W.R., R.M. Williams, and W.W. Webb,* Nonlinear magic: multiphoton microscopy in the biosciences. *Nature biotechnology, 2003. 21(11): p. 1369-1377.*

159.   *Tokin Ivan B., T.I.I.a.F.G.F.,* Quantitative morphometric analysis of liver biopsy: problems and perspectives, *in Liver Biopsy, H. Takahashi, Editor 2011, InTech.*

160.   *Tokin Ivan, B.,* Quantitative Morphometric Analysis of Liver Biopsy: Problems and Perspectives. *2011.*

161.   *Guilbert, T., et al.,* A robust collagen scoring method for human liver fibrosis by second harmonic microscopy. *Opt Express, 2010. 18(25): p. 25794-807.*

162.   *Marcellin, P., et al.,* Regression of cirrhosis during treatment with tenofovir disoproxil fumarate for chronic hepatitis B: a 5-year open-label follow-up study. *Lancet, 2013. 381(9865): p. 468-75.*

163.   *Rosselli, M., et al.,* Beyond scoring: a modern interpretation of disease progression in chronic liver disease. *Gut, 2013. 62(9): p. 1234-41.*

164.   *Hytiroglou, P., et al.,* Beyond "cirrhosis": a proposal from the International Liver Pathology Study Group. *Am J Clin Pathol, 2012. 137(1): p. 5-9.*

165.   *Chen, Y.P., et al.,* Larger biopsies evaluation of transient elastography for detecting advanced fibrosis in patients with compensated chronic hepatitis B. *Journal of gastroenterology and hepatology, 2012. 27(7): p. 1219-1226.*

166.   *Friedman, S.L.,* Evolving challenges in hepatic fibrosis. *Nature Reviews Gastroenterology and Hepatology, 2010. 7(8): p. 425-436.*

167.   *Rockey, D.C., et al.,* Liver biopsy. *Hepatology, 2008. 49(3): p. 1017-1044.*

168.   *CarEy, E. and W.D. CAREY,* Noninvasive tests for liver disease, fibrosis, and cirrhosis: Is liver biopsy obsolete? *Cleveland Clinic journal of medicine, 2010. 77(8): p. 519-527.*

169.   *Mart ńez, S.M., et al.,* Noninvasive assessment of liver fibrosis. *Hepatology, 2011. 53(1): p. 325-335.*

170.   *Taouli, B., R.L. Ehman, and S.B. Reeder,* Advanced MRI methods for assessment of chronic liver disease. *American Journal of Roentgenology, 2009. 193(1): p. 14-27.*

171.   *Choong, C., S.K. Venkatesh, and E. Siew,* Accuracy of Routine Clinical Ultrasound for Staging of Liver Fibrosis. *Journal of Clinical Imaging Science, 2012. 2(1): p. 58.*

172.   *Ziol, M., et al.,* **Noninvasive assessment of liver fibrosis by measurement of stiffness in patients with chronic hepatitis C.** *Hepatology, 2004. 41(1): p. 48-54.*

173.   *Friedrich–Rust, M., et al.,* **Performance of transient elastography for the staging of liver fibrosis: a meta-analysis.** *Gastroenterology, 2008. 134(4): p. 960-974. e8.*

174.   *Rouvière, O., et al.,* **MR Elastography of the Liver: Preliminary Results1.** *Radiology, 2006. 240(2): p. 440-448.*

175.   *Huwart, L., et al.,* **Magnetic resonance elastography for the noninvasive staging of liver fibrosis.** *Gastroenterology, 2008. 135(1): p. 32.*

176.   *Shaheen, A.A.M., A.F. Wan, and R.P. Myers,* **FibroTest and FibroScan for the prediction of hepatitis C-related fibrosis: a systematic review of diagnostic test accuracy.** *The American journal of gastroenterology, 2007. 102(11): p. 2589-2600.*

177.   *Lucidarme, D., et al.,* **Factors of accuracy of transient elastography (fibroscan) for the diagnosis of liver fibrosis in chronic hepatitis C.** *Hepatology, 2008. 49(4): p. 1083-1089.*

178.   *Park, S.H., et al.,* **Usefulness of multiple biomarkers for the prediction of significant fibrosis in chronic hepatitis B.** *Journal of clinical gastroenterology, 2011. 45(4): p. 361.*

179.   *Baranova, A., et al.,* **Non-Invasive markers for hepatic fibrosis.** *BMC gastroenterology, 2011. 11(1): p. 91.*

180.   *He, Y., et al.,* **Toward surface quantification of liver fibrosis progression.** *Journal of biomedical optics, 2010. 15(5): p. 056007-056007-11.*

181.   *MacAulay, C., P. Lane, and R. Richards-Kortum,* **In vivo pathology: microendoscopy as a new endoscopic imaging modality.** *Gastrointestinal endoscopy clinics of North America, 2004. 14(3): p. 595-620.*

182.   *HOSOYAMADA, Y., H. KURIHARA, and T. SAKAI,* **Ultrastructural localisation and size distribution of collagen fibrils in Glisson's sheath of rat liver: implications for mechanical environment and possible producing cells.** *Journal of Anatomy, 2002. 196(3): p. 327-340.*

183.   *Bedossa, P. and T. Poynard,* **The METAVIR cooperative study group: An algorithm for the grading of activity in chronic hepatitis C.** *Hepatology, 1996. 24(2).*

184.   *Knodell, R.G., et al.,* **Formulation and application of a numerical scoring system for assessing histological activity in asymptomatic chronic active hepatitis.** *Hepatology, 1981. 1(5): p. 431-435.*

185.   Ishak, K., et al., **Histological grading and staging of chronic hepatitis.** *J hepatol, 1995. 22: p. 696-699.*

186.   Lee, H.S., et al., **Optical biopsy of liver fibrosis by use of multiphoton microscopy.** *Optics letters, 2004. 29(22): p. 2614-2616.*

187.   Sun, W., et al., **Nonlinear optical microscopy: use of second harmonic generation and two-photon microscopy for automated quantitative liver fibrosis studies.** *Journal of biomedical optics, 2008. 13(6): p. 064010-064010-7.*

188.   Tai, D.C.S., et al., **Fibro-C-Index: comprehensive, morphology-based quantification of liver fibrosis using second harmonic generation and two-photon microscopy.** *Journal of biomedical optics, 2009. 14(4): p. 044013-044013-10.*

189.   Regev, A., et al., **Sampling error and intraobserver variation in liver biopsy in patients with chronic HCV infection.** *The American journal of gastroenterology, 2002. 97(10): p. 2614-2618.*

190.   Constandinou, C., N. Henderson, and J.P. Iredale, **Modeling liver fibrosis in rodents.** *Methods in molecular medicine, 2005. 117: p. 237.*

191.   Iredale, J.P., **Models of liver fibrosis: exploring the dynamic nature of inflammation and repair in a solid organ.** *Journal of Clinical Investigation, 2007. 117(3): p. 539.*

192.   Goodman, Z.D., **Grading and staging systems for inflammation and fibrosis in chronic liver diseases.** *Journal of hepatology, 2007. 47(4): p. 598-607.*

193.   Frangi, A.F., et al., **Multiscale vessel enhancement filtering,** *in* Medical Image Computing and Computer-Assisted Intervention—MICCAI'98*1998, Springer. p. 130-137.*

194.   Gedda, M. and P. Vallotton. **Three-dimensional tracing of neurites in fluorescence microscopy images using local path-finding.** *in* Acoustics Speech and Signal Processing (ICASSP), 2010 IEEE International Conference on. *2010. IEEE.*

195.   Telea, A. and J.J. Van Wijk. **An augmented fast marching method for computing skeletons and centerlines.** *in* Proceedings of the symposium on Data Visualisation 2002. *2002. Eurographics Association.*

196.   Qian, X., et al., **A non-parametric vessel detection method for complex vascular structures.** *Medical image analysis, 2009. 13(1): p. 49-61.*

197.   Dijkstra, E.W., **A note on two problems in connexion with graphs.** *Numerische mathematik, 1959. 1(1): p. 269-271.*

198.   Haralick, R.M., K. Shanmugam, and I.H. Dinstein, **Textural features for image classification.** *Systems, Man and Cybernetics, IEEE Transactions on, 1973(6): p. 610-621.*

199.   Shen, J. and G. Strang, **Asymptotics of daubechies filters, scaling functions, and wavelets.** *Applied and Computational Harmonic Analysis, 1998. 5(3): p. 312-331.*

200.   Daugman, J.G., **Complete discrete 2-D Gabor transforms by neural networks for image analysis and compression.** *Acoustics, Speech and Signal Processing, IEEE Transactions on, 1988. 36(7): p. 1169-1179.*

201.   Pinsky, M.A., **Introduction to Fourier analysis and wavelets.** *Vol. 102. 2002: Amer Mathematical Society.*

202.   Guyon, I., et al., **Gene selection for cancer classification using support vector machines.** *Machine learning, 2002. 46(1): p. 389-422.*

203.   Wu, C.F.J., **Jackknife, bootstrap and other resampling methods in regression analysis.** *The Annals of Statistics, 1986. 14(4): p. 1261-1295.*

204.   Hanley, J.A., **Characteristic (ROC) Curvel.** *Radiology, 1982. 743: p. 29-36.*

205.   Wallis, J.W. and T.R. Miller, **Three-dimensional display in nuclear medicine and radiology.** *Journal of nuclear medicine: official publication, Society of Nuclear Medicine, 1991. 32(3): p. 534.*

206.   Greene, W.H. and C. Zhang, **Econometric analysis.** *Vol. 3. 1997: Prentice hall Upper Saddle River, NJ.*

207.   Georges, P.C., et al., **Increased stiffness of the rat liver precedes matrix deposition: implications for fibrosis.** *American Journal of Physiology-Gastrointestinal and Liver Physiology, 2007. 293(6): p. G1147-G1154.*

208.   Wells, R.G., **The role of matrix stiffness in regulating cell behavior.** *Hepatology, 2008. 47(4): p. 1394-1400.*

209.   Geerts, A.M., et al., **Comparison of three research models of portal hypertension in mice: macroscopic, histological and portal pressure evaluation.** *International journal of experimental pathology, 2008. 89(4): p. 251-263.*

210.   Guerra, R.R., et al., **A novel chronic cirrhosis TAA-induced model in rats.** *Brazilian Journal of Veterinary Pathology, 2010. 3(1): p. 9-16.*

211.   Castera, L., **Non-invasive assessment of liver fibrosis in chronic hepatitis C.** *Hepatology international, 2011. 5(2): p. 625-634.*

212.   *Wu, Y., et al.,* **Scanning fiber-optic nonlinear endomicroscopy with miniature aspherical compound lens and multimode fiber collector.** *Optics letters, 2009. 34(7): p. 953-955.*

213.   *Zhang, Y., et al.,* **A compact fiber-optic SHG scanning endomicroscope and its application to visualize cervical remodeling during pregnancy.** *Proceedings of the National Academy of Sciences, 2012. 109(32): p. 12878-12883.*

214.   *Fu, L., et al.,* **Nonlinear optical endoscopy based on a double-clad photonic crystal fiber and a MEMS mirror.** *Optics Express, 2006. 14(3): p. 1027-1032.*

215.   *Bao, H., et al.,* **Second harmonic generation imaging via nonlinear endomicroscopy.** *Optics Express, 2010. 18(2): p. 1255-1260.*

216.   *Brown, C.M., et al.,* **In vivo imaging of unstained tissues using a compact and flexible multiphoton microendoscope.** *Journal of biomedical optics, 2012. 17(4): p. 040505-1-040505-3.*

217.   *Rivera, D.R., et al.,* **Compact and flexible raster scanning multiphoton endoscope capable of imaging unstained tissue.** *Proceedings of the National Academy of Sciences, 2011. 108(43): p. 17598-17603.*

218.   *Lin, J., et al.,* **Assessment of liver steatosis and fibrosis in rats using integrated coherent anti-Stokes Raman scattering and multiphoton imaging technique.** *Journal of Biomedical Optics, 2011. 16(11): p. 116024-1160247.*

219.   *Freudiger, C.W., et al.,* **Multicolored stain-free histopathology with coherent Raman imaging.** *Laboratory investigation, 2012. 92(10): p. 1492-1502.*

220.   *Meyer, T., et al.,* **Interpreting CARS images of tissue within the C–H-stretching region.** *Journal of biophotonics, 2012. 5(10): p. 729-733.*

221.   *Medyukhina, A., et al.,* **Towards automated segmentation of cells and cell nuclei in nonlinear optical microscopy.** *Journal of biophotonics, 2012. 5(11-12): p. 878-888.*

222.   *Lowe, D.G.* **Object recognition from local scale-invariant features.** *in* **Computer vision, 1999. The proceedings of the seventh IEEE international conference on.** *1999. Ieee.*

223.   *Bay, H., et al.,* **Speeded-up robust features (SURF).** *Computer vision and image understanding, 2008. 110(3): p. 346-359.*